

Guidance, Control and Trajectory Tracking of Small Fixed Wing  
Unmanned Aerial Vehicles (UAV's)

A THESIS IN MECHATRONICS

Presented to the faculty of the American University of Sharjah  
College of Engineering  
in partial fulfillment of  
the requirements for the degree of

MASTER OF SCIENCE

by

AMER A. KH. AL-RADAIDEH

B.S. 2006

Sharjah, UAE

April 2009

©2009

AMER A. KH. AL-RADAIDEH

ALL RIGHTS RESERVED

# Guidance, Control and Trajectory Tracking of Small Fixed Wing Unmanned Aerial Vehicles (UAV's)

Amer A.KH.Al-Radaideh, Candidate for Master of Science in Mechatronics Engineering

American University of Sharjah, 2009

## ABSTRACT

Unmanned Aerial Vehicles (UAV's) have gained increasing considerations due to their low cost and increased autonomy. A large number of applications in the military and civilian fields. The present work considers a low level flight control algorithms (auto-pilot) to improve the guidance, path following and trajectory tracking capabilities of the low speed fixed wing AUS-UAV. In addition, this investigation aims the development and building of fully functioning test-bed UAV platform. The test-bed includes an enhanced hardware in the loop simulation "HILS" system to facilitate the development and evaluation of the ability of the flight control systems (FCS) of the AUS-UAV to follow prescribed trajectories.

At the end of this thesis, the AUS-UAV was modelled using ground based numerical modelling for the aerodynamic coefficients in the early phases. Then, the aerodynamic coefficients estimation was enhanced using flight test based identification. The engine and actuator were also identified.

Furthermore, a trajectory tracking algorithm was designed, implemented and evaluated using HILS. The avionics unit was also designed, calibrated and tested. Finally, flight test were conducted using Krestal autopilot to experiment with flight testing and compare the performance with our avionics unit HILS results.

# CONTENTS

<b>Abstract</b>	<b>iii</b>
<b>List of Figures</b>	<b>vi</b>
<b>List of Tables</b>	<b>x</b>
<b>Nomenclature</b>	<b>xii</b>
<b>Acknowledgements</b>	<b>xvi</b>
<b>1 Introduction</b>	<b>1</b>
1.1 Unmanned Aerial Vehicles(UAVs) . . . . .	1
1.1.1 Predator . . . . .	2
1.1.2 Hermes . . . . .	3
1.1.3 Aerosonde . . . . .	3
1.2 UAV History . . . . .	4
1.3 UAV Missions and Applications . . . . .	6
1.4 Guidance and control Background . . . . .	7
1.5 Previous research on UAVs at AUS . . . . .	9
1.6 Thesis objectives and contribution . . . . .	11
1.7 Thesis outline . . . . .	12
<b>2 ARF60 AUS-UAV Nonlinear Model and Dynamics Equations</b>	<b>14</b>
2.1 UAV Coordinate Frames and Axis System Definition . . . . .	14
2.1.1 Inertial Frame . . . . .	14
2.1.2 Body Frame . . . . .	14
2.1.3 Stability Frame . . . . .	15
2.1.4 Wind Frame . . . . .	16
2.2 UAV Aerodynamic Control Surfaces . . . . .	17
2.3 UAV Equations of Motion . . . . .	20
2.3.1 UAV Forces and Moments . . . . .	20
2.3.2 UAV Orientation and Position . . . . .	23
2.4 Aerodynamic coefficients for forces and moments . . . . .	24
2.4.1 Aerodynamic Forces . . . . .	24
2.4.2 Aerodynamic Moments . . . . .	25
2.5 Implementation of the ARF60 AUS-UAV Nonlinear Model in Simulink	25

<b>3</b>	<b>ARF60 AUS-UAV Modeling and System Identifications</b>	<b>27</b>
3.1	Introduction . . . . .	27
3.2	Overview of UAV System ID and literature Review . . . . .	28
3.3	System ID steps . . . . .	30
3.4	Aircraft System ID . . . . .	31
3.4.1	Aerodynamic Numerical modeling . . . . .	31
3.4.2	Flight Tests Based System ID . . . . .	33
3.5	OS 61FX Engine and its Propeller System ID . . . . .	40
3.6	Actuator System ID . . . . .	42
<b>4</b>	<b>ARF60 AUS-UAV Aircraft Natural Motion, Controller Design and Simulation</b>	<b>45</b>
4.1	Aircraft Linear Model . . . . .	45
4.1.1	ARF60 UAV Longitudinal Model . . . . .	45
4.1.2	ARF60 UAV Lateral Model . . . . .	47
4.2	ARF60 UAV Autopilot design using Successive Loop Closure (SLC) .	50
4.2.1	Autopilot Overview . . . . .	50
4.2.2	Longitudinal Autopilot . . . . .	55
4.2.3	Lateral Autopilot . . . . .	62
4.2.4	Trajectory Tracker(Shortest Flight Algorithm in 3D) . . . . .	66
<b>5</b>	<b>Control and Hardware Implementation</b>	<b>71</b>
5.1	Signals, Hardware and Software . . . . .	72
5.1.1	Control Signals . . . . .	72
5.1.2	Control Hardware . . . . .	72
5.2	Avionics . . . . .	74
5.2.1	Flight Controller Computer (MPC555 Microcontroller) . . . . .	74
5.2.2	INS/GPS Unit . . . . .	75
5.2.3	Battery and Power Distribution Board . . . . .	77
5.3	Ground Station Design . . . . .	77
5.3.1	Ground Station GUI . . . . .	78
5.4	Summary . . . . .	82
<b>6</b>	<b>Hardware in the loop Simulation (HILS)</b>	<b>84</b>
6.1	Hardware in the Loop Simulation Development . . . . .	85
6.1.1	ARF60 UAV 6-DOF model simulator . . . . .	85
6.1.2	R/C transmitter . . . . .	86
6.1.3	Data communication and synchronization . . . . .	87
6.1.4	HILS Summary . . . . .	88
6.2	Hardware in the loop Simulation Results . . . . .	89
6.2.1	HILS Autopilot Results . . . . .	89
6.2.2	HILS Trajectory Tracking Results . . . . .	89

<b>7</b>	<b>Flight Tests Results and Autopilot Tuning</b>	<b>95</b>
7.1	Kestrel Autopilot Overview . . . . .	95
7.1.1	Mounting Kestrel Autopilot on the ARF60 UAV . . . . .	96
7.1.2	Flight Testing Using Kestrel Autopilot . . . . .	101
<b>8</b>	<b>Thesis Summary and Future Work</b>	<b>119</b>
8.1	Summary and Contributions . . . . .	119
8.1.1	Avionics Unit Development . . . . .	119
8.1.2	System Identification and Aircraft Nonlinear Modelling . . . . .	119
8.1.3	Developing Hardware in The Loop Simulation . . . . .	119
8.1.4	Implementing SLC Based Autopilot and Trajectory Tracking Using Simulink Embedded Model-based Design . . . . .	119
8.1.5	Developing Common Ground Station for UxV's in AUS . . . . .	120
8.1.6	Flight Testing . . . . .	120
8.2	Future Work . . . . .	120
8.2.1	Ground Station Enhancement . . . . .	120
8.2.2	Nonlinear Autopilot and Trajectory Tracking Enhancement . . . . .	120
8.2.3	Nonlinear System Identification . . . . .	120
<b>A</b>	<b>Geometry, Aerodynamic, and other Aircraft Design information</b>	<b>121</b>
A.1	Aircraft Geometry Definitions . . . . .	121
A.1.1	Wingspan . . . . .	121
A.1.2	Mean Aerodynamic Chord (MAC) . . . . .	121
A.1.3	Aspect ratio (AR) . . . . .	122
<b>B</b>	<b>Hardware and Softwares Used in This Thesis</b>	<b>123</b>
B.1	Hardware . . . . .	123
B.1.1	OS FS120 Engine . . . . .	123
B.1.2	MIDG II INS/GPS . . . . .	123
B.1.3	MPX4115A Absolute Pressure Sensor . . . . .	125
B.1.4	1INCHGBASIC Differential Pressure Sensor . . . . .	126
<b>C</b>	<b>Engine and Actuators System Identification</b>	<b>127</b>
C.1	Engine System ID . . . . .	127
C.1.1	The Engine and its Propeller Modeling . . . . .	127
C.2	Actuator System ID . . . . .	128
	<b>References</b>	<b>134</b>

## LIST OF FIGURES

1.1	Predator-UAV. . . . .	3
1.2	Hermes 450 UAV. . . . .	4
1.3	Aerosonde-UAV. . . . .	5
1.4	RPioneer, first commissioned UAV. . . . .	6
1.5	AUS Avionics Unit constructed in (Hadi, 2005) . . . . .	10
1.6	The HILS Setup designed in (Hassan, 2006) . . . . .	10
1.7	The Ground Station Built in (Hassan, 2006) . . . . .	11
1.8	UAV System Architecture . . . . .	12
2.1	Inertial Axis Definition . . . . .	15
2.2	Body Axis Definition . . . . .	15
2.3	Stability Axis Definition . . . . .	16
2.4	Wind Axis Definition . . . . .	16
2.5	Control Surface Deflection . . . . .	17
2.6	Aileron Control Surface . . . . .	18
2.7	Elevator Control Surface . . . . .	19
2.8	Rudder Control Surface . . . . .	19
2.9	ARF60 UAV Simulink Model general Structure . . . . .	26
3.1	UAV components dynamics and control . . . . .	29
3.2	System Identification Steps . . . . .	31
3.3	CG location Experiment top . . . . .	32
3.4	CG location Experiment . . . . .	32
3.5	Construction of System identification for the ARF60 UAV . . . . .	35
3.6	ARF60 Actuators deflections during the system identification test . . . . .	35
3.7	ARF60 Angular Rates during the system identification test . . . . .	36
3.8	ARF60 Accelerations during the system identification test . . . . .	36
3.9	ARF60 Attitudes during the system identification test . . . . .	37
3.10	ARF60 Velocities during the system identification test . . . . .	37
3.11	ARF60 Position during the system identification test . . . . .	38
3.12	ARF60 Air Data during the system identification test . . . . .	38
3.13	The OS 61FX RPM measured output for the validation data set, together with the output from the ARX, ARMAX, OE and BJ models when simulated with the input sequence from the validation data set . . . . .	42
3.14	The OS 61FX thrust measured output for the validation data set, together with the output from the ARX, ARMAX, OE and BJ models when simulated with the input sequence from the validation data set . . . . .	43

3.15	Thrust measured output together with the output from the BJ model when simulated with the input PRBS . . . . .	43
3.16	Actuator Identification Setup . . . . .	44
4.1	Poles Locations for the Longitudinal Model . . . . .	47
4.2	Impulse Response for the Longitudinal Model . . . . .	48
4.3	Poles Locations for the Lateral Model . . . . .	49
4.4	Aircraft in a Steady Banked Turn . . . . .	53
4.5	SISO Design Task,Root Locus Graphical Tuning Window, Analysis Plots and Compensator Parameters Tuning Editor. . . . .	56
4.6	Pitch Rate Damping Block Diagram . . . . .	57
4.7	Pitch Rate Damping Root Locus . . . . .	58
4.8	Pitch attitude hold using elevator Block Diagram . . . . .	59
4.9	Pitch attitude hold using elevator step response . . . . .	60
4.10	Altitude hold using commanded pitch Block Diagram . . . . .	60
4.11	Altitude hold using commanded pitch loop step response . . . . .	61
4.12	Airspeed hold using throttle Block Diagram . . . . .	62
4.13	Airspeed hold using throttle step response . . . . .	62
4.14	ARF60 Longitudinal Autopilot Block Diagram . . . . .	63
4.15	Roll Rate Damping Block Diagram . . . . .	63
4.16	Roll Attitude Hold Block Diagram . . . . .	64
4.17	Dutch Roll Damper Block Diagram . . . . .	65
4.18	ARF60 Lateral Autopilot Block Diagram . . . . .	65
4.19	Path taken by the UAV When Entering a Curve using Feedback Guidance . . . . .	66
4.20	Extension of the Feedback Guidance Strategy - Bidirectional . . . . .	67
4.21	ARF60 Autopilot and Trajectory Tracker System Block Diagram . . . . .	68
4.22	Four waypoints navigation results . . . . .	69
4.23	Four waypoints navigation Map 2D . . . . .	70
4.24	Four waypoints navigation plot 3D . . . . .	70
5.1	AUS Avionics and Ground station Block Diagram . . . . .	71
5.2	AUS Avionics Unit. . . . .	74
5.3	MIDG II:Inertial Navigation System (INS) with Global Positioning System (GPS) . . . . .	75
5.4	Block Diagram of Avionics Power Distribution . . . . .	77
5.5	Autopilot Panel-Ground Station . . . . .	78
5.6	Desired Commands Panel-Ground Station . . . . .	79
5.7	Actuators Monitoring Panel-Ground Station . . . . .	79
5.8	States Monitoring Panel-Ground Station . . . . .	80
5.9	Ground Station Map . . . . .	81
5.10	Ground Station Map Settings . . . . .	81
5.11	PID Loops Parameters-Ground Station . . . . .	82
5.12	Data Log Panel-Ground Station . . . . .	82



5.13	Communication Settings Panel-Ground Station . . . . .	83
6.1	Hardware-in-the-loop (HIL) simulation Setup . . . . .	85
6.2	Hardware-in-the-loop (HIL) simulation environment . . . . .	87
6.3	HILS Autopilot Test 1 -Attitudes . . . . .	90
6.4	HILS Autopilot Test 2 - States Results . . . . .	90
6.5	2WP Navigation-2D . . . . .	91
6.6	2WP Navigation-3D . . . . .	91
6.7	2WP Navigation-Map . . . . .	92
6.8	2WP Navigation-Attitudes . . . . .	92
6.9	4WP Navigation (Hourglass Shape)-2D . . . . .	93
6.10	4WP Navigation (Hourglass Shape)-3D . . . . .	93
6.11	4WP Navigation (Hourglass Shape)-Map . . . . .	94
6.12	4WP Navigation (Hourglass Shape)-Attitudes . . . . .	94
7.1	Kestrel Autopilot . . . . .	96
7.2	Kestrel Autopilot Diagram . . . . .	96
7.3	Kestrel Autopilot Block Diagram . . . . .	97
7.4	Kestrel Autopilot with spacers . . . . .	97
7.5	Kestrel Autopilot isolation from inside . . . . .	98
7.6	Kestrel Autopilot isolation from outside . . . . .	98
7.7	Kestrel Autopilot inside the Alumunime box . . . . .	99
7.8	GPS Location on the aircraft . . . . .	99
7.9	RF Antenna Location on the Aircraft . . . . .	100
7.10	Pitot Static Tube Location on the Aircraft . . . . .	100
7.11	Pitot Static Tube Location on the Aircraft . . . . .	101
7.12	Crashed test (1) . . . . .	102
7.13	Crashed test (2) . . . . .	102
7.14	Roll Hold Test1 . . . . .	104
7.15	Roll Hold Test1 Error Analysis . . . . .	104
7.16	Roll Hold Test1 Map . . . . .	105
7.17	Roll Hold Test2 . . . . .	105
7.18	Roll Hold Test2 Error Analysis . . . . .	106
7.19	Roll Hold Test2 Map . . . . .	106
7.20	Pitch Hold Test . . . . .	107
7.21	Airspeed Hold Test . . . . .	107
7.22	150m Loiter Test . . . . .	109
7.23	Error Analysis for the Altitude from the 150m Loiter Test . . . . .	110
7.24	Error Analysis for the Pitch from the 150m Loiter Test . . . . .	110
7.25	Error Analysis for the Roll from the 150m Loiter Test . . . . .	111
7.26	150m Loiter Test Map . . . . .	111
7.27	Square Pattern . . . . .	112
7.28	Four Waypoints Square Trajectory Test . . . . .	112

7.29	Four Waypoints Square Trajectory Test Analysis . . . . .	113
7.30	Four Waypoints Square 3D Trajectory . . . . .	113
7.31	Four Laps:Four Waypoints Square 2D Trajectory . . . . .	114
7.32	Four Laps:Four Waypoints Square 3D Trajectory . . . . .	114
7.33	Four Laps:Four Waypoints Square 3D Trajectory Map . . . . .	115
7.34	Hourglass Pattern . . . . .	115
7.35	Four Waypoints Hourglass Trajectory Test . . . . .	116
7.36	Four Waypoints Hourglass Trajectory Test Analysis . . . . .	116
7.37	Four Waypoints Hourglass 3D Trajectory . . . . .	117
7.38	Three Laps:Four Waypoints Hourglass 3D Trajectory . . . . .	117
7.39	Three Laps:Three Waypoints Hourglass 3D Trajectory Map . . . . .	118
B.1	OS FS120 Engine . . . . .	123
B.2	MIDG II:Inertial Navigation System (INS) with Global Positioning System (GPS) . . . . .	124
B.3	MMPX4115A Absolute Pressure Sensor . . . . .	125
C.1	Load Cell Calibration Plot . . . . .	129
C.2	Engine Identification Setup . . . . .	130
C.3	PRBS PWM Signal Generation using dSpace Toolbox Blocks . . . . .	130
C.4	RPM Measurement using dSpace Toolbox Blocks . . . . .	131
C.5	Thrust Measurement using dSpace Toolbox Blocks . . . . .	131
C.6	Actuator Identification Setup . . . . .	131
C.7	Aileron actuator response with the doublets input . . . . .	132
C.8	Aileron Actuator Identification Results for Doublets inputs . . . . .	132
C.9	Aileron actuator response with the PRBS input . . . . .	133
C.10	Aileron Actuator Identification Results for PRBS inputs . . . . .	133

## LIST OF TABLES

3.1	ARF60 measured geometric parameters - input to the MATLAB script	33
3.2	Stability derivatives of the ARF60 UAV (All units per radian) . . . .	34
3.3	Identified Stability derivatives of the ARF60 UAV (All units per radian) using System ID algorithm . . . . .	41
3.4	OS 61FX Engine RPM System ID Results . . . . .	41
3.5	OS 61FX Engine Thrust System ID Results . . . . .	42
4.1	Pole locations, natural frequencies and periods for the longitudinal modes. . . . .	47
4.2	Pole locations, natural frequencies and periods for the lateral modes.	49
4.3	Pitch attitude hold using elevator loop gains . . . . .	59
4.4	Altitude hold using commanded pitch loop gains . . . . .	61
4.5	Airspeed hold using throttle loop gains . . . . .	62
4.6	Dutch Roll Damper loop gains . . . . .	65
5.1	MIDG II Specifications . . . . .	76
5.2	Cost, Mass and Power Consumption . . . . .	83
7.1	Calibration data . . . . .	102
7.2	Stability Augmentation System (SAS) gains . . . . .	103
7.3	Inner Attitude Hold Loops gains . . . . .	108
7.4	Outer Airspeed Hold PID Loops Gains . . . . .	108
7.5	Outer Altitude Hold PID Loops Gains . . . . .	108
B.1	S FS120 Engine Specifications . . . . .	124
C.1	Load cell calibration data . . . . .	129

# NOMENCLATURE

## Axis System (Reference Frames), Angles and Transformations

$i$	Inertial reference frame
$B$	Body reference frame
$F_i(O_i X_i Y_i Z_i)$	Inertial axis system
$F_B(O_B X_B Y_B Z_B)$	Body axis system
$F_S(O_S X_S Y_S Z_S)$	Stability Frame
$F_W(O_W X_W Y_W Z_W)$	Wind Frame
$h$	Altitude
$\varphi$	Latitude
$\lambda$	Longitude
$\phi$	Roll angle
$\theta$	Pitch angle
$\psi$	Yaw angle
$\alpha$	Angle of Attack (AOA)
$\beta$	Angle of Side Slip (AOS)

## Earth Quantities (WGS-84)

$g_n$	Normal gravitational acceleration ( $\varphi = 45^\circ$ )
$a$	Equatorial radius of the Earth (semimajor axis) = 6378137.000 m
$b$	polar radius of the Earth (semiminor axis) = 6356752.3142 m
$\Omega$	Earth turn rate with respect to $i$ frame = $7.292116 \times 10^{-5}$ rad/s
$\mathbf{g}_l$	Local gravity column matrix
$f$	Flattening (ellipticity) = $1/298.257223563$ (0.00335281066474)
$e$	Major eccentricity of Earth = 0.0818191908426
$\mu$	Earth's gravitational constant = $3986005 \times 10^8 m^3/s^2$
$M$	Mass of Earth (including the atmosphere) = $5.9733328 \times 10^{24}$ Kg

## System Identifications

$ARX$	Autoregressive with exogenous inputs model
$ARMAX$	Autoregressive moving average model with exogenous inputs model
$OE$	Output Error
$BJ$	Box-Jenkins

## Stability Derivatives

$C_{L_0}$	Zero alpha lift
$C_{L_\alpha}$	Alpha derivative
$C_{L_{\alpha t}}$	Alpha derivative for the tail

$C_{L\alpha_v}$	Alpha derivative for the vertical tail
$C_{L\delta_e}$	Pitch control (elevator) derivative
$C_{L\dot{\alpha}}$	Alpha-dot derivative
$C_{Lq}$	Pitch rate derivative
$C_{D_0}$	Minimum drag
$C_{D\delta_e}$	Pitch control (elevator) derivative
$C_{D\delta_a}$	Roll control (aileron) derivative
$C_{D\delta_r}$	Yaw control (rudder) derivative
$C_{Y\beta}$	Sideslip derivative
$C_{Y\delta_a}$	Roll control derivative
$C_{Y\delta_r}$	Yaw control derivative
$C_{Yp}$	Roll rate derivative
$C_{Yr}$	Yaw rate derivative
$C_{m_0}$	Zero alpha pitch
$C_{m\alpha}$	Alpha derivative
$C_{m\delta_e}$	Pitch control derivative
$C_{m\dot{\alpha}}$	Alpha dot derivative
$C_{mq}$	Pitch rate derivative
$C_{l\beta}$	Sideslip derivative
$C_{l\delta_a}$	Roll control derivative
$C_{l\delta_r}$	Yaw control derivative
$C_{lp}$	Roll rate derivative
$C_{lr}$	Yaw rate derivative
$C_{n\beta}$	Sideslip derivative
$C_{n\delta_a}$	Roll control derivative
$C_{n\delta_r}$	Yaw control derivative
$C_{np}$	Roll rate derivative
$C_{nr}$	Yaw rate derivative

#### Static Quantities

$AR$	aspect ratio
$b$	wing span (i.e., tip to tip)
$c$	wing chord (varies along span)
$\bar{c}$	mean aerodynamic chord (mac)
$S$	wing area total
$\lambda$	taper ratio (tip chord/root chord)
$\Lambda$	leading-edge sweep angle
$J_x$	Moment of inertia in the x-axis
$J_y$	Moment of inertia in the y-axis
$J_z$	Moment of inertia in the z-axis
$J_{xz}$	Moment of inertia in the xz-plane

#### Dynamic Quantities

$D$	Drag
$L$	Lift

$\ell_w$	Rolling moment
$m_w$	Pitching moment
$n_w$	Yawing moment
$V_n$	Normal gravitational acceleration ( $\varphi = 45^\circ$ )
$\mathbf{V}_e^n$	Kinematic velocity expressed in $n$ frame
$\omega_{nb}^b$	Angular rate of $b$ frame relative to $n$ frame expressed in $b$ frame
$\omega_{en}^n$	Angular rate of $n$ frame relative to $e$ frame expressed in $n$ frame
$\omega_{ib}^b$	Angular rate of $b$ frame relative to $n$ frame expressed in $b$ frame
$\mathbf{f}^e$	Specific force in $b$ frame
$\mathbf{f}^b$	Specific force in $n$ frame
$v_N, v_E, v_D$	The north, east and down components of $\mathbf{V}_e^n$
$f_N, f_E, f_D$	The north, east and down components of $\mathbf{f}_e^n$
$V_{air}$	The true UAV airspeed
$u$	X-axis velocity in the body frame
$v$	Y-axis velocity in the body frame
$w$	Z-axis velocity in the body frame
$p$	Roll rate
$q$	Pitch rate
$r$	Yaw rate
$C_X$	Drag force aerodynamic coefficient
$C_Y$	Side force aerodynamic coefficient
$C_Z$	Lift force aerodynamic coefficient
$C_\ell$	X-axis aerodynamic moment coefficient
$C_m$	Y-axis aerodynamic moment coefficient
$C_n$	Z-axis aerodynamic moment coefficient

#### Subscripts

$j, k, l$	Indexes for high speed computer cycle ( $j$ -cycle), moderate computer speed cycle ( $k$ -cycle) and low computer speed cycle ( $l$ -cycle) respectively
$N, E, D$	North, East and Down components of $n$ frame vector

#### Abbreviations

ARF	Almost Ready to Fly
COTS	Cost-Of-The-Shelf
CR	Confidence Region
DCM	Direction Cosine Matrix
DGPS	Differential Global Positioning System
DOF	Degrees of Freedom
ECEF	Earth-Centered Earth-Fixed
GPS	Global Positioning System
IMU	Inertial Measurement Unit
INS	Inertial Navigation System
KF	Kalman Filter
NED	North-East-Down

UAV  
PRBS

Unmanned Aerial Vehicle  
Pseud Random Binary Sequence

## ACKNOWLEDGEMENTS

This MSc Thesis has only been possible with the help and support of some people I would like to thank very much.

First of all, I would like to sincerely thank my advisor Prof.Dr.Mohammad-Ameen Al Jarrah for his support during this thesis, for the guidance, support and for always believing in me and pushing me for more.

It is difficult to overstate my appreciation to Dr.Ali Jhemi, who gave me a lot of his valuable time and provided me with a lot of support. And I am deeply grateful to my colleagues Elvanto Ikhsan, Tri Hardimasyar and Guntur Supriyadi. I cant forget all the days that we spent in flight testing.

To all the colleagues in the Mechatronics Program, Hossein Sadjadi, Hussein Sahli, Laith Sahawneh, Mohammed Assadi, Amal Khattab, Tariq Abu-Hashim, Yasmeeen Abu-Kheil, Ali Ghazi, Mohammed Saleh, Khaled Al-Suwaidi, Oubada Al-Dabbas, Hazaa Al-Abdouli, Hamad Al-Kotbi, Faisal Al-Kabi, Behrooz Mozafferi, Ihab Abu-Younis, Younes Al-Younes and Mahmoud Ghaith. The best friends ever. Thank You all.

I am also very grateful to all my professors in AUS for teaching me such fascinating topics during those two years. I would not have brought this project very far without such a previous knowledge.

Thanks go to the ILL people at AUS-Library, for your non-ending support.

Finally, I would like to thank all my friends in AUS, and particularly those who helped me enjoying those first two years in UAE.

**To my parents, brothers and sister, whom my words can't describe.**

***To Knowledge.***



## CHAPTER 1

# INTRODUCTION

Unmanned Aerial Vehicles (UAVs) research and development is a growing area as their cost and reliability is improving. However, significant development is needed in order to get a reliable autonomous system capable of performing all types of maneuvers with reasonable performance and stability. Advanced control algorithms are usually non-linear methods of feedback control implemented in the Digital Flight Control System (DFCS) of the UAV, or what is usually called the autopilot. The autopilot consists of several components that are integrated together along with a tailored embedded software to perform a specific task. Autonomous UAV's operation is improving continuously from advances in other technologies like sensor fusion, propulsion systems, navigation aids and single-chip embedded system. Advance control technology, embedded systems, and MEMS technology made autonomous systems feasible and cost effective (Jung, 2001). The availability and ease of use of this kind of technologies made it relatively cost effective and affordable to develop UAVs' advanced control systems. In this chapter a brief introduction to UAVs, what they are, and what they do, as well as their history and previous work done will be presented. Finally, we will state the thesis' objectives and contribution.

### 1.1 UNMANNED AERIAL VEHICLES(UAVS)

UAV is Unmanned Aerial Vehicle that is controlled autonomously by an integrated system called the Autopilot. In the old days, the autopilot was built using analog circuits that form several PID (Proportional Integral Derivative) loops to provide aircraft stability. Nowadays, microcontrollers with embedded software are used in modern control of a UAV. Microcontrollers are the brain of the autopilot, they read the signals from all onboard sensors, like inertial sensors and air data sensors, and then they process the data according to the control algorithm and command the actuator accordingly. The initial design of autopilots served as a Stability Augmentation

System (SAS) that provides proper flight stability of a marginally stable or unstable aircrafts. But in UAVs the autopilot takes full control over the aircraft. With a specific mission programmed in the microcontroller, UAVs can be fully autonomous. But most UAVs nowadays can also be remotely controlled in case of any emergency. UAVs vary in size, cost, mission, and endurance. They can be from a several inches micro size UAV that perform very short missions to over one hundred feet UAV that has high endurance and high range communication capabilities like High Altitude Long Endurance (HALE) ([www.gruntsmilitary.com](http://www.gruntsmilitary.com)). UAVs have several features that make them attractive. It's not only their capability of flying autonomously and performing specific missions, but also because they are relatively inexpensive compared to manned aircrafts. Using UAVs in dangerous missions behind enemy lines will also protect the lives of human pilots. A new breed of UAVs is the UCAVs (Unmanned Combat Aerial Vehicle) (Pike, 2005) which are designed to address a variety of the most dangerous missions due to their high maneuverability and endurance. These vehicles are usually stealthy and used for suppression of enemy air defenses, persistent surveillance, reconnaissance and precision strike ([www.gruntsmilitary.com](http://www.gruntsmilitary.com)). An example of these UCAVs is the Boeing X-45A UCAV (Pike, 2005). Below are several examples of UAVs and some details about each one of them.

### 1.1.1 Predator

The Predator was the first tactical UAV with significant participation in the U.S. Air Force ([www.gruntsmilitary.com](http://www.gruntsmilitary.com)). With a range of up to 500 miles, and endurance capabilities exceeding 20 hours, the Predator was designed with the capability to provide near real time imagery intelligence to the theater through use of infrared sensors along with payloads capable of penetrating adverse weather. The Predator is flown by Air Force pilots from a remote facility with the air vehicle controlled by line-of-sight satellite relay data links. During 1995 and 1996, the Predator was flown in Albania in support of relief operations as well as follow-on operations in Bosnia supporting Operation Deny Flight. Predator UAV is shown in Figure 1.1.



Figure 1.1: Predator-UAV.

### 1.1.2 Hermes

The Hermes 450 is a single engine UAV with advanced composite structure and optimized aerodynamics ([www.israeli-weapons.com](http://www.israeli-weapons.com)). The advanced avionics unit installed inside it enables the Hermes 450 to perform autonomous flight and precise GPS navigation. Reliability is significantly increased by having a fully redundant system. Target detection and recognition are performed by gimballed, electro-optical payloads. The UAV is equipped with advanced communication system transferring video in real time to ground control stations. The Hermes 450 is the latest generation and most advanced UAV deployed with the Israel Defense Forces (IDF). Already operational for some time, the 450s have successfully completed acceptance tests and established the highest standards of reliability, availability and maintainability in their class. Hermes 450 UAV is shown in Figure 1.2.

### 1.1.3 Aerosonde

The Aerosonde is a small robotic aircraft for long-range environmental monitoring and surveillance (Holland, 1998). It has been developed especially for meteorological and environmental reconnaissance over oceanic and remote areas and in harsh conditions, for which its economy and flexibility will allow routine operations on a much wider scale than has been possible in the past. On August, 21 1998 Aerosonde "Laima" became the first unmanned aircraft to cross the north Atlantic. The crossing was



Figure 1.2: Hermes 450 UAV.

completed within 15 minutes of schedule after a flight of 3270 km in a time of 26 h 45 min. Altitude was specified at 1680m, dropping to around 150m on approach to Benbecula, all that on a gallon and a half of fuel.

## 1.2 UAV HISTORY

The origin of UAVs goes back to the development of RPVs (Remotely Piloted Vehicles), which served afterwards as the basic chassis for the future UAVs. It all started with the development of the RPV RP-1 (Naughton, 2003) by former movie star and modeler, Reginald Denny. The first Remote Piloted Vehicle was designed and tested by him in 1935.

In the mid-1930s, radio-controlled model airplanes became the basis for the Army Air Corps' development of the aerial targets for antiaircraft gunnery training. Starting in 1935, the Radioplane Company in California developed several variations of the RP-1 (Naughton, 2003). Then UAVs were used in World War II when unmanned remotely controlled aircraft served as primitive, cruise missiles and gunnery targets such as the famous German V-1 (R. Connor, 2001). In the near past, Israel invested heavily in remotely piloted aircraft technology during the late 1960s after the Egyptians surprised Israeli aircrews during the short Six-Day War in early June 1967



Figure 1.3: Aerosonde-UAV.

(R. Connor, 2001). When Israel invaded Lebanon in 1982, Israel Aircraft Industries, Ltd., (IAI) was manufacturing the Scout UAV (R. Connor, 2001). Successes flying the Scout during the invasion and subsequent flight demonstrations of this UAV's capabilities convinced leaders in the U.S. Navy Mediterranean Fleet to acquire their own Scouts. In 1984, IAI and Tadiran, Ltd., formed a joint subsidiary company called Mazlat Ltd., to develop an improved version of the Scout known as the Pioneer. The following year, Mazlat flew the Pioneer in a UAV competition sponsored by the U.S. Navy, which it won a contract to build this UAV in January 1986. Within the following two years, orders were placed for nine complete systems (UAVs + ground equipment) with a total of about 50 air vehicles. The U.S. Navy's Pioneer was the first tactical battlefield UAV in service with the U.S. armed forces ([www.puav.com](http://www.puav.com)).

A Pioneer airframe consists of a twin-tail boom fuselage with two vertical stabilizers on the tail and a conventional wing and stub fuselage mounting a pusher engine. The airframe consists of carbon-fiber composites, fiberglass, Kevlar, aluminum, and balsa wood. These lightweight materials enable the Pioneer to loft its payload of surveillance equipment with a 26 horsepower, two-cycle engine. The non-metallic



Figure 1.4: RPioneer, first commissioned UAV.

composites also reduce the UAV's radar cross-section. A fuel capacity of 12 gallons of 100-octane aviation gasoline can keep the Pioneer airborne for 5.5 hours. Between 1985 and 1994, Pioneer units logged over 10,000 flight hours. The Pioneer UAVs were first used operationally in Operation Desert Storm in early 1991 ([www.puav.com](http://www.puav.com)). They were quite successful and their deployment significantly contributed to the increasing recognition of UAVs as valid combat elements. After the Pioneer a lot of UAVs have been deployed. The most famous one nowadays is the Predator shown in the previous section.

### 1.3 UAV MISSIONS AND APPLICATIONS

UAVs are used in both military and civil operations. In military operations UAVs are used for tactical intelligence, surveillance, and reconnaissance purposes. UAVs can keep manned aircrafts out of hostile areas while providing real time information needed for battle decisions. They can also detect ground vehicles and transmit their images as well as their coordinates. UAVs maybe used to attack specific ground targets, like the Predator which carries the hellfire missiles ([www.gruntsmilitary.com](http://www.gruntsmilitary.com)). The newUCAVs are specially designed for combat operations to accomplish the most dangerous missions (Pike, 2005). For civil applications, UAVs can be used as a de-

livery vehicle for critical medical supplies needed anywhere (Holland, 1998). The coast guard and border patrol can deploy UAVs to watch coastal waters, patrol the nation's borders, and protect major oil and gas pipelines. UAVs can also be part of traffic monitoring and control. Another potential application is law enforcement surveillance, where UAV can be used to track suspicious vehicles to its hideout. UAVs can also be used in research applications and the development of artificial intelligent vehicles. UAVs are used in aerospace systems research and development (Jung, 2001). They serve as an ideal test bed for conducting air vehicle configuration studies, aerodynamic research, maneuver analysis, and flight control design. In weather research UAV can navigate through thunderstorms or nearby hurricanes to get some data on these hazardous phenomena (Holland, 1998). These kinds of applications can endanger the life of human pilots because we still do not fully understand how these natural phenomena work. Therefore UAVs maybe used to predict their behaviors. An example of a civil oriented UAV is the Aerosonde (Holland, 1998). The Aerosonde is being deployed to fill chronic gaps in the global upper-air sounding network, to conduct systematic surveillance of tropical cyclones and other severe weather, to undertake offshore surveillance and agricultural/biological surveys, and to obtain specialist observations, such as volcanic plumes.

#### 1.4 GUIDANCE AND CONTROL BACKGROUND

Recently several papers discussed new numerous guidance and control algorithms. Such techniques have been proposed for nonlinear systems. Vector Field approach is one of the most recent methods for UAV path following (Beard, 2006). In this paper, vector fields approach is used to represent desired ground track headings to direct the vehicle to the desired path. The key feature of this approach is that ground track heading error and lateral following error reach zero asymptotically even in the presence of constant wind. Another guidance strategy is to steer the UAV from a given initial position and heading to a specified destination way-point in an obstacle free environment which is called the feedback guidance strategy presented in (Bhatt S. P., 2005). The feedback guidance strategy achieves perfect guidance at constant altitude and speed under continuous and perfect position and heading updates. In this thesis, the performance of this guidance strategy under discrete position and

heading updates from the GPS was studied through simulation.

Providing an accurate path following is considered to be one of the main key engineering challenges to obtain full autonomy for an aerial vehicle (Rolf, 2003). Therefore, many path following techniques were proposed. Among them, Lyapunov vector fields (Beard, 2006), and Helmsman behavior (Wise, 2006). Lyapunov vector field calculates a vector field around the path to be tracked. Such vectors are directed toward the path to be followed and in the desired direction of flight. Then, the vectors in the field serve as heading commands to the UAV. The method is currently applicable to paths composed of straight lines and arcs. However, using vector field can cause an extreme and unpredictable viewing pattern when the UAV encounters sharp direction changes or when the UAV becomes slower than the target (Wise, 2006). Another technique for path following is the use of Helmsman behavior guidance law. In such technique, the path geometry to be followed is determined based on the current position, heading and a standoff distance. Any deviations from this path produce errors on course angle and cross track distance. To converge back to the desired path, Helmsman behavior provides smoothly transitions from current path to the desired path by simultaneously bringing cross track distance and course angle errors to zero (Wise, 2006).

Many researches have been done on path following and trajectory tracking of UAVs. For example, (Kaminer & Silvestre, 1998) proposed a combined approach for developing guidance and control algorithms for autonomous vehicle trajectory tracking. The proposed approach was based on gain scheduling and was tested through simulations of a small UAV. Another study was conducted by (S. Park & How, 2004) who presented a way for tight tracking of curved trajectories. In their approach, they estimated PD control for straight-line paths while for curved paths, they implemented an additional control element to enhance the tracking capability. The implemented approach was validated with flight tests experiments. Moreover, (Beard, 2006) proposed a new method for Miniature Air Vehicle (MAV) path following based on the concept of vector fields. Their objectives were to reach the path while flying at a predefined airspeed. In their approach, they combined course measurements in the path following control with the vector field strategy. They proved, using Lyapunov stability criteria, that the vector field provides asymptotic following for straight-line and circular paths in the presence of constant wind disturbances. To demonstrate the



effectiveness of path-following abilities enabled by the vector field algorithm, MAVs were commanded to fly a variety of paths composed of straight lines, orbits, and combinations of straight lines and circular arcs. Results showed that following errors average was less than one wingspan in both steady straight-line and orbit paths. In the case of paths involving frequent transitions between straight-line and arc segments, following errors average was less than three wingspans.

## 1.5 PREVIOUS RESEARCH ON UAVS AT AUS

Significant research work has been done in the area of UAV at AUS. The first research was completed by a graduate student (Hadi, 2005). He designed, built and tested a low cost Avionics Unit consisting of an embedded system integrated with sensors and actuators. Figure 1.5 shows the implemented Avionics Unit. The embedded system consists of a PID controlled Dynamic Flight Controller System (DFCS) or Stability Augmentation System (SAS), a Longitudinal Autopilot created using Discrete State Space Controller implementing Linear Quadratic Regulator (LQR), and a Lateral Autopilot created using PID controller. The SAS was able to maintain stability of the aircraft during various disturbances and also extricate itself from rough transitions or turns. The Longitudinal Autopilot maintains a reference speed and altitude within tolerable limits. The Lateral Autopilot is used to turn the aircraft to a given direction. The embedded system implementing the autopilots also initiates a wireless link with a Ground Station to send sensor data at regular interval for future flight performance analysis. The Embedded Controller also implements a text based configuration menu to set reference gains and offset trims, to adapt the aircraft to different flight environments.

Another graduate research (thesis) has been completed by AUS Master student (Hassan, 2006). He demonstrated using Hardware in the Loop Simulation (HILS), Figure 1.6, that the existing UAV test-bed can be utilized to perform waypoint navigation in three dimensions. Waypoint navigation consists of getting the aircraft to fly to within 50 meters over subsequent waypoints or position coordinates. The waypoints selected by the Ground User by clicking on the map in the Ground Station, Figure 1.7, and then sent to the UAV via the wireless link thus allowing "flexible mission" capability. The path taken by the UAV to navigate between waypoints had

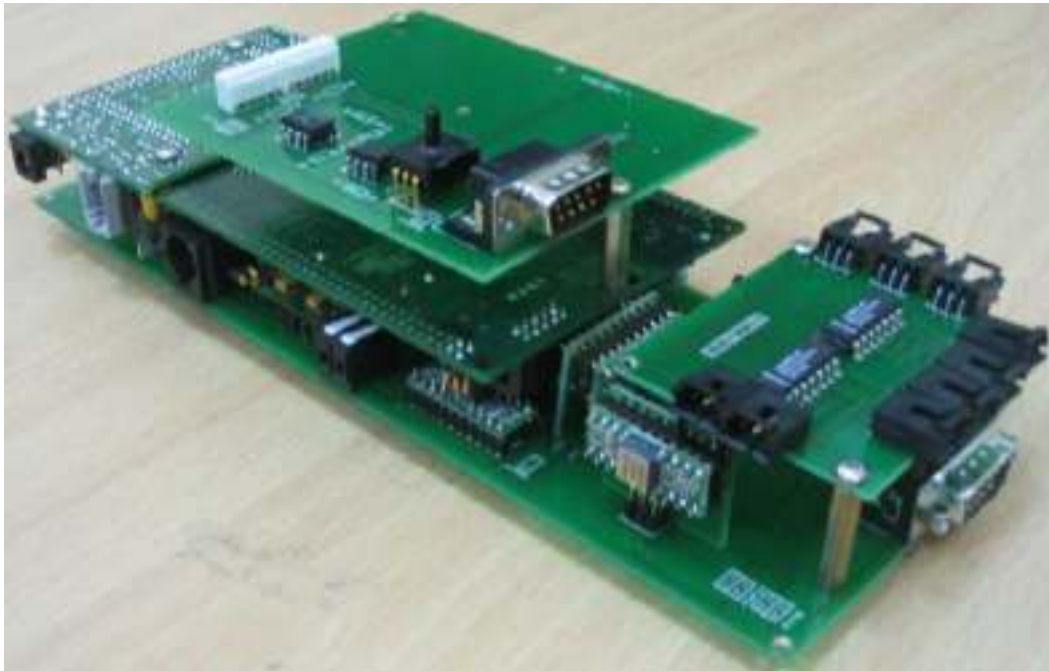


Figure 1.5: AUS Avionics Unit constructed in (Hadi, 2005)

to be smooth and fast and doesn't violate the flight constraints of the UAV.



Figure 1.6: The HILS Setup designed in (Hassan, 2006)

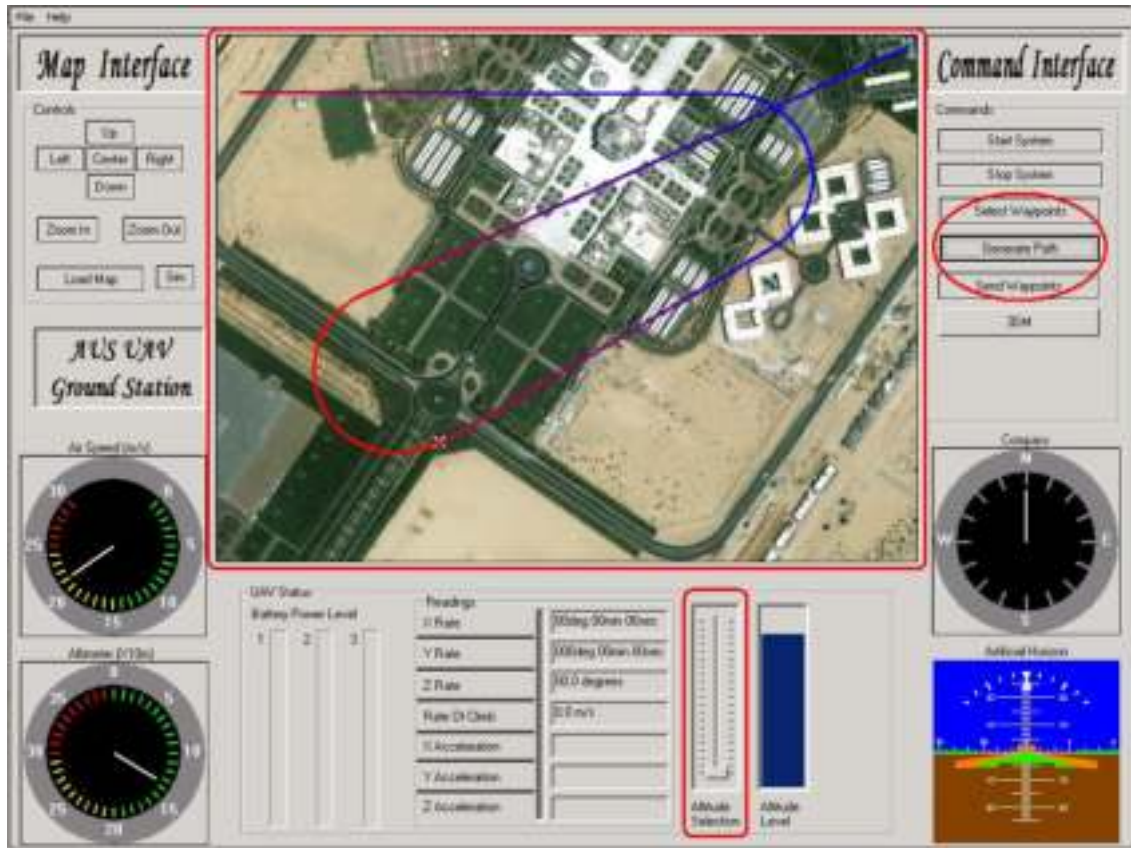


Figure 1.7: The Ground Station Built in (Hassan, 2006)

## 1.6 THESIS OBJECTIVES AND CONTRIBUTION

As shown in Figure 1.8, the UAV system architecture considered in this thesis consists of five layers: the Waypoint Path Planner (WPP), the Dynamic Trajectory Smoother (DTS), the Trajectory Tracker (TT), the Longitudinal and Lateral Autopilots, and the UAV. The description and the role of each is listed below:

**Waypoint Path Planner (WPP)** The WPP generates waypoint paths (straight-line segments) that change in accordance with the dynamic environment consisting of the location of the UAV, the targets, and the dynamically changing threats.

**Dynamic Trajectory Smoother (DTS)** The DTS smoothes through these waypoints and produces a feasible time parameterized desired trajectory, that is, the desired position, heading, and altitude.

**Trajectory Tracker (TT)** The TT outputs the desired velocity command, heading command, and altitude command to the autopilots based on the desired

trajectory.

**Longitudinal and Lateral Autopilots** The autopilots then use these commands to control the elevator, aileron, rudder deflections and the throttle setting of the UAV.

**UAV** The UAV model which will be identified to get the mathematical model. This mathematical model will be used to develop and integrate the above layers together in the designed HILS.

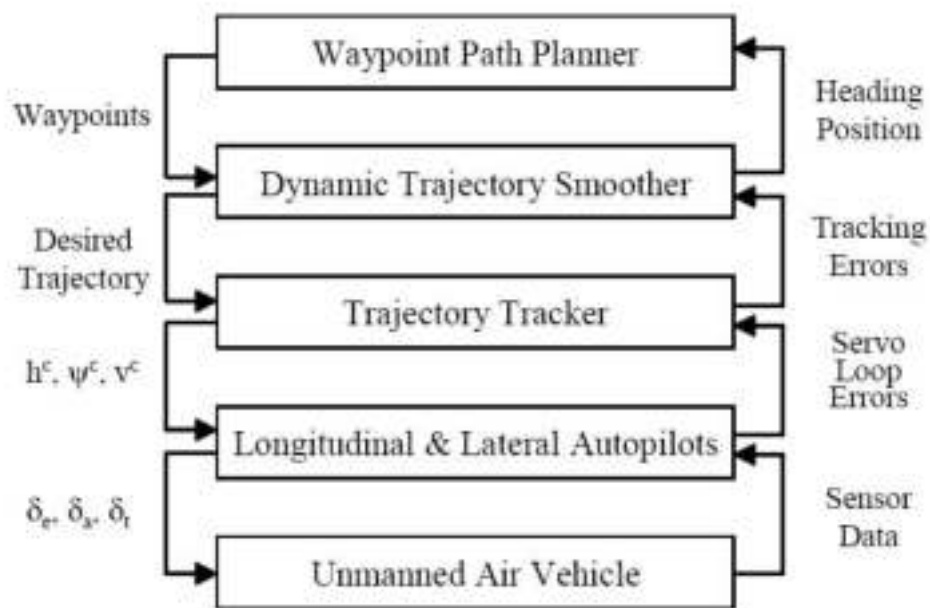


Figure 1.8: UAV System Architecture

Where the objectives of this thesis is building a model of the ARF60 UAV, designing the longitudinal and lateral autopilots and implementing the trajectory tracker. The integration of the above layers was validated using the hardware in the loop simulation which was developed as well.

## 1.7 THESIS OUTLINE

This thesis is organized as follows. Chapter 2 explains the nonlinear mathematical model and dynamics equations. The ARF60 AUS-UAV modeling and system identifications is addressed in Chapter 3. The controller design, and simulation of the ARF60 AUS-UAV are in Chapter 4. Chapters 5-6 cover the move from simulation to

---

a hardware platform through the hardware in the loop simulation (HILS). Hardware results of real-time trajectory tracking are presented in Chapter 7. Conclusions and recommendations for future work are addressed in Chapter 8.

## CHAPTER 2

# ARF60 AUS-UAV NONLINEAR MODEL AND DYNAMICS EQUATIONS

### 2.1 UAV COORDINATE FRAMES AND AXIS SYSTEM DEFINITION

Before developing the nonlinear dynamic model of the aircraft, several coordinate frames and axes must be defined.

In this section, the inertial frame, the body frame, the stability frame and the wind frame will be described first.

#### 2.1.1 Inertial Frame

With reference to Figure 2.1, the inertial axis system,  $F_i(O_iX_iY_iZ_i)$  is an earth fixed coordinate system. Its origin  $O_i$  is located at some point on the earth surface. With the positive  $Z_i$  directed toward the center of the earth. the positive  $X_i$  directed to the north and perpendicular to  $Z_i$  while the positive  $Y_i$  directed to the east and perpendicular to the  $X_iZ_i$  (Peddle, 2005). In this thesis, the earth is assumed to be flat and not rotating since our UAV flight ranges aren't significantly large (1-3Km).

#### 2.1.2 Body Frame

$F_B(O_BX_BY_BZ_B)$  is the body frame with its origin is the CG (Center of Gravity) of the UAV. The positive  $X_B$  axis directing out of the nose of the UAV, the positive  $Y_B$  perpendicular to  $X_B$  and directing out of the right wing while the positive  $Z_B$  axis is out of the UAV frame pointing downward and perpendicular to the  $X_BY_B$  plane.

The UAV is said to *Roll* about the  $X_B$ -axis, *Pitch* about the  $Y_B$ , *Yaw* about the  $Z_B$ . The axes definition of the stability frame is shown in Figure 2.2.



Figure 2.1: Inertial Axis Definition

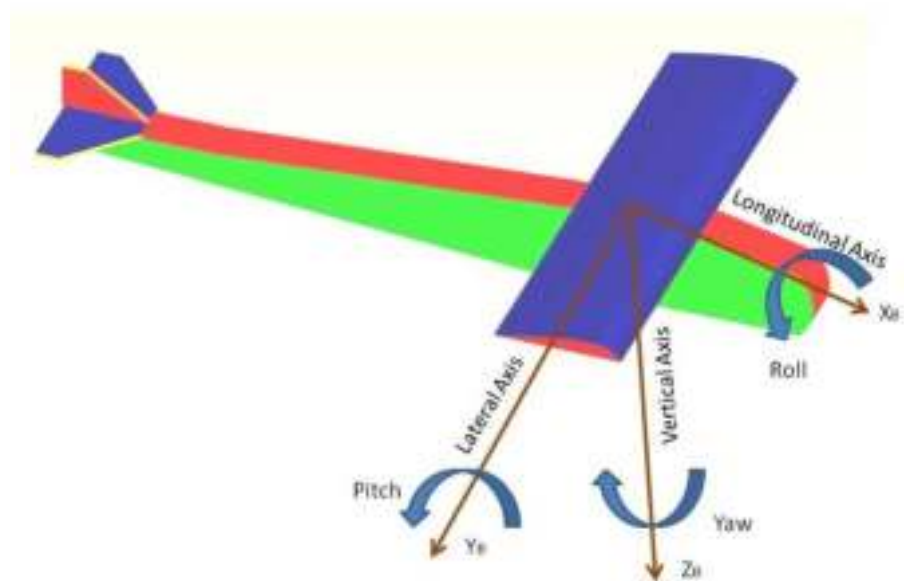


Figure 2.2: Body Axis Definition

### 2.1.3 Stability Frame

When the  $X_B$  axis of the body frame pitch with  $\alpha$  angle of attack ( $AOA$ ) then the body axis frame is referred to as *Stability Frame*  $F_S(O_S X_S Y_S Z_S)$  as shown in Figure 2.3.

Stability frame generates the aerodynamic forces, and thus reducing the aerodynamic model to its simplest form.

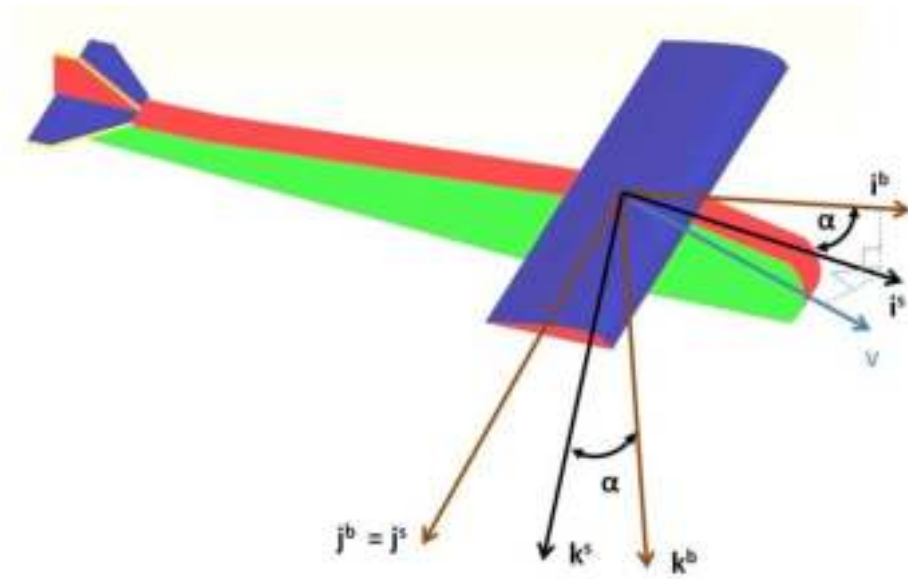


Figure 2.3: Stability Axis Definition

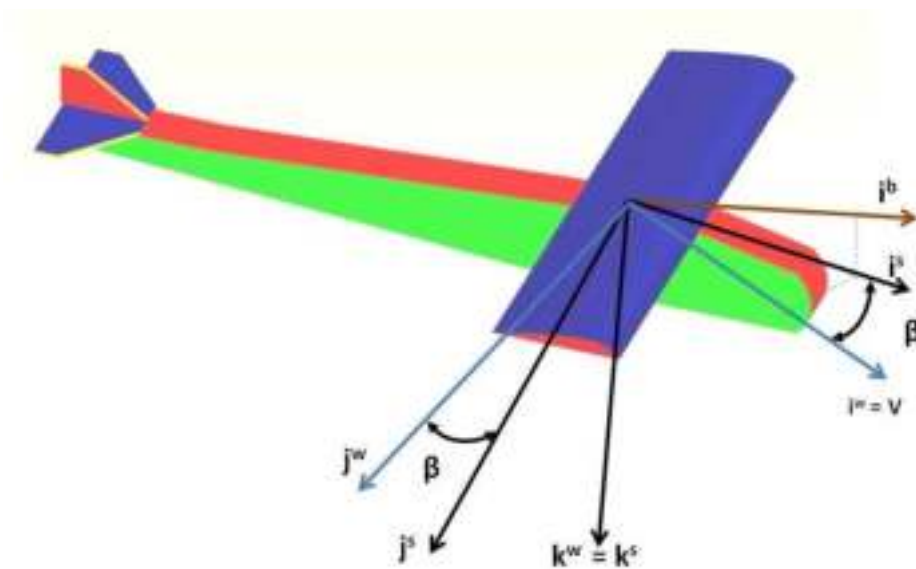


Figure 2.4: Wind Axis Definition

#### 2.1.4 Wind Frame

Whenever the *Body Frame* faces a wind, it is going to yaw into the wind with  $\beta$  Angle of Sideslip. Then the body axis frame is referred to as *Wind Frame*  $F_W(O_W X_W Y_W Z_W)$ . The wind frame axes definition is illustrated in Figure 2.4.

The following relations are useful and good to be introduced at this point:

$$V_{air} = \sqrt{U^2 + V^2 + W^2} \quad (2.1)$$



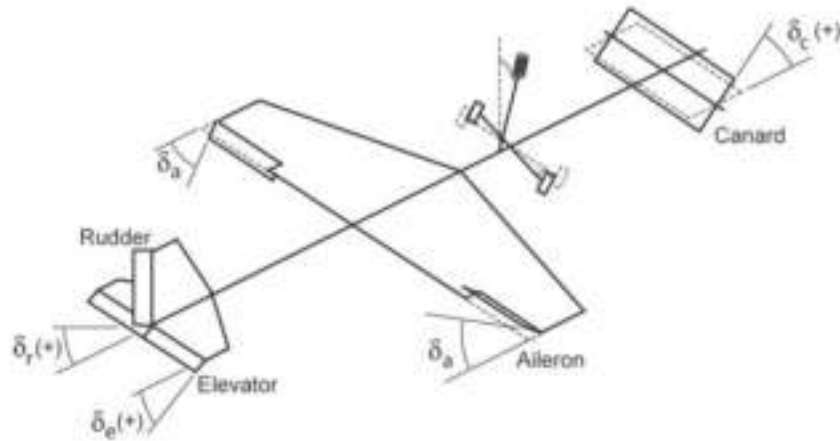


Figure 2.5: Control Surface Deflection

$$\alpha = \arctan\left(\frac{W}{U}\right) \quad (2.2)$$

$$\beta = \arcsin\left(\frac{V}{V_{air}}\right) \quad (2.3)$$

## 2.2 UAV AERODYNAMIC CONTROL SURFACES

The conventional aerodynamic control surface deflection variables will be defined also with reference to Figure 2.5.

- $\delta_a$ -Aileron Control Surface Deflection Angle.

Positive deflection causes a negative rolling moment. Ailerons can be used to generate a rolling motion for the UAV.

Ailerons are used to bank the UAV; to cause one wing tip to move up and the other wing tip to move down. The banking creates an unbalanced side force component of the large wing lift force which causes the UAV's flight path to curve.

With greater downward deflection, the lift will increase in the upward direction. Figure 2.6 shows the aileron on the left wing deflected down while the aileron

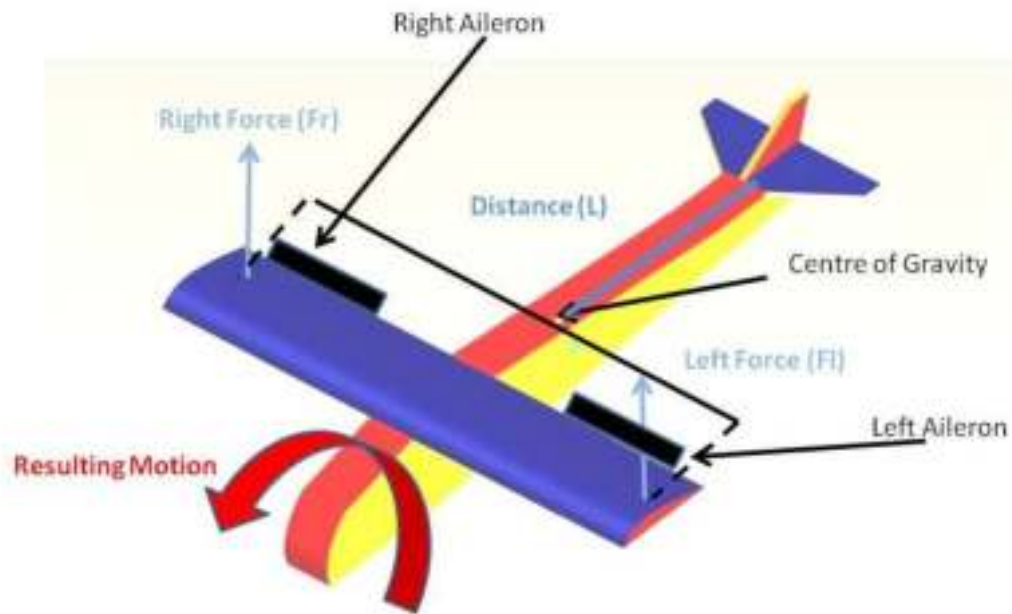


Figure 2.6: Aileron Control Surface

on the right wing is deflected up to produce positive rolling moment.

- $\delta_e$ -Elevator Control Surface Deflection Angle.

Normal convention in aeronautics is that positive elevator deflection causes a negative pitching moment (nose down moment) see Figure 2.7. The elevator is used to control the position of the nose attitude of the UAV and the angle of attack of the wing.

- $\delta_r$ -Rudder Control Surface Deflection Angle.

The convention in aeronautical engineering literature is that positive rudder deflection causes a negative yawing moment. The vertical tail prevents side-to-side, or yawing, motion of the UAV nose. The movements of the rudder, varies the amount of force generated by the tail surface and is used to generate and control the yawing motion of the aircraft see figure 2.8. The rudder also is used to control the position of the nose of the UAV.

- $\delta_t$ -Throttle Control Lever Movement.

It is also prudent to include a throttle actuation variable, denoted by  $\delta_t$ , that is

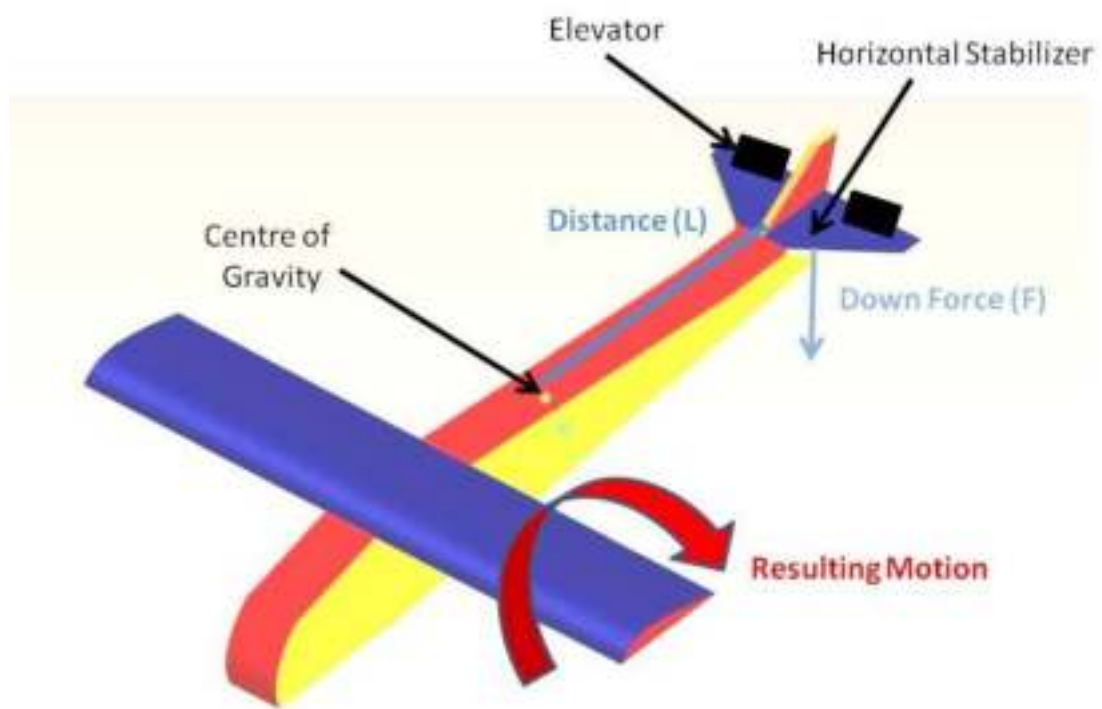


Figure 2.7: Elevator Control Surface

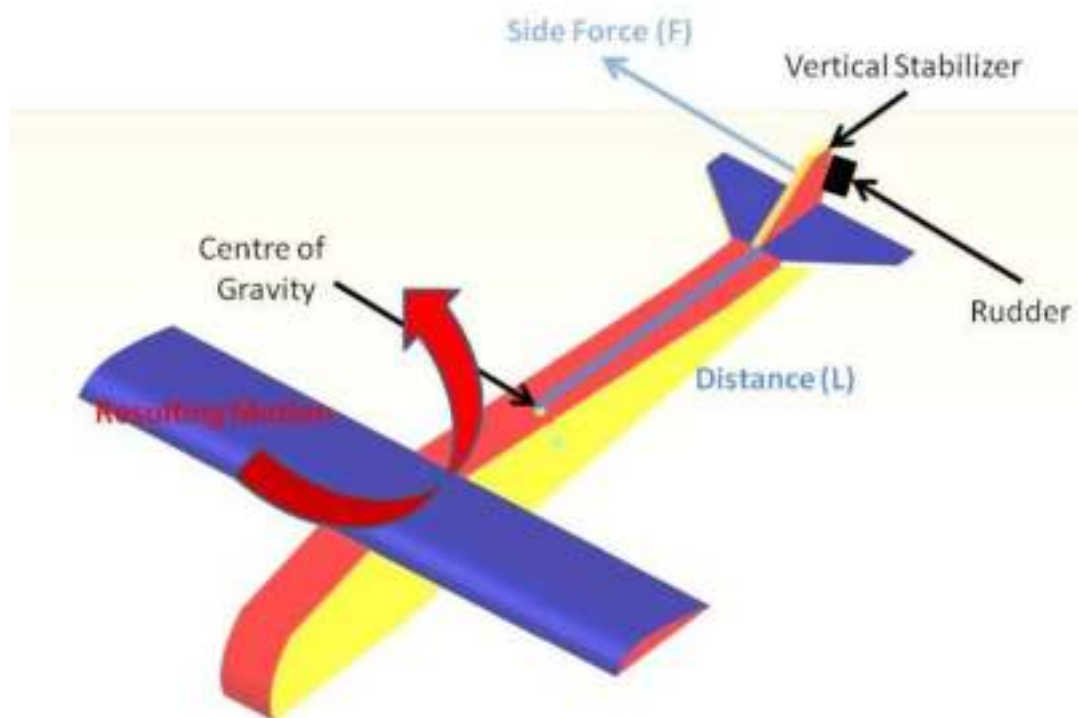


Figure 2.8: Rudder Control Surface

related to the output of the magnitude of the UAV thrust vector.

The movement of the throttle lever range is between (0-1), where the two limits correspond to engine cutoff and full throttle respectively.

### 2.3 UAV EQUATIONS OF MOTION

The basis for analysis, computation, and simulation of the motions of the UAV as well as autopilot design is the mathematical model of the UAV and its subsystems. Actual UAV systems are highly complicated nonlinear systems. It consists of an aggregate of elastic bodies so connected that both rigid and elastic relative motions can occur. For example, the propeller rotates, control surfaces move about their hinges, and bending and twisting of the various aerodynamic surfaces occur. The external forces that act on the UAV are also complex functions of shape and motion. Realistic analysis of engineering precision are not likely to be accomplished with a very simple mathematical model. The model that is developed in the following section is a classical model. It has been found by aeronautical engineers and researchers to be very useful in practise. The vehicle is treated as a single rigid body with six degree of freedom. This body is free to move in the atmosphere under the actions of gravity and aerodynamic forces.

As indicated earlier in section 2.1, the Earth is treated as flat and stationary in inertial space. These assumptions simplify the model enormously, and are quite acceptable for analyzing most problems of UAV flight (Peddle, 2005).

#### 2.3.1 UAV Forces and Moments

Newton's second law of motion is used to determine the effect of the net force and moment on a body. It states that the summation of all external forces acting on a body is equal to the time rate of change of the linear momentum of the body, and the summation of the external moments acting on the body is equal to the time rate of change of the angular momentum.

The summary of the equations consists of three forces and moments equations are expressed in matrix form in Equations 2.4 and 2.5 respectively.

The gravitational force acting on the airplane acts through the center of gravity of the airplane. Because the body axis system is fixed to the center of gravity, the gravitational force will not produce any moments. It will contribute to the external force acting on the airplane, however, and have components along the respective body axis. The gravitational force components along the x,y, and z axes are expressed in Equation 2.4c.

The aerodynamic forces and moments (Equations 2.4d and 2.5l) are obtained from the dimensionless aerodynamic coefficients at a trimmed flight condition which will be discussed thoroughly in section 2.4.

The thrust force due to propulsion can have components that act along each of the body axis. In addition, the propulsive forces can create moments if the thrust does not act through the CG. The propulsive forces and moments acting along the body axis system are denoted in Equation 2.4e and Equation 2.5k respectively (Randal W. Beard, 2007).

- Force equations:

$$\begin{pmatrix} \dot{u} \\ \dot{v} \\ \dot{w} \end{pmatrix} = \begin{pmatrix} rv - qw \\ pw - ru \\ qu - pv \end{pmatrix} + 1/m \begin{pmatrix} f_x \\ f_y \\ f_z \end{pmatrix} \quad (2.4a)$$

$$\begin{pmatrix} f_x \\ f_y \\ f_z \end{pmatrix} = \begin{pmatrix} f_{gx} \\ f_{gy} \\ f_{gz} \end{pmatrix} + \begin{pmatrix} f_{ax} \\ f_{ay} \\ f_{az} \end{pmatrix} + \begin{pmatrix} f_{px} \\ f_{py} \\ f_{pz} \end{pmatrix} \quad (2.4b)$$

$$\begin{pmatrix} f_{gx} \\ f_{gy} \\ f_{gz} \end{pmatrix} = \begin{pmatrix} -mg \sin \theta \\ mg \cos \theta \sin \phi \\ mg \cos \theta \cos \phi \end{pmatrix} \quad (2.4c)$$

$$\begin{pmatrix} f_{ax} \\ f_{ay} \\ f_{az} \end{pmatrix} = \begin{pmatrix} \frac{1}{2} \rho V_{air}^2 SC_x \\ \frac{1}{2} \rho V_{air}^2 SC_y \\ \frac{1}{2} \rho V_{air}^2 SC_z \end{pmatrix} \quad (2.4d)$$

$$\begin{pmatrix} f_{px} \\ f_{py} \\ f_{pz} \end{pmatrix} = \begin{pmatrix} X_T \\ Y_T \\ Z_T \end{pmatrix} \quad (2.4e)$$

where:

$f_g$ =gravitational forces.

$f_a$ =aerodynamic forces.

$f_p$ =forces due to thrust.

- Moment Equations:

$$\begin{pmatrix} \dot{p} \\ \dot{q} \\ \dot{r} \end{pmatrix} = \begin{pmatrix} \Gamma_1 pq - \Gamma_2 qr \\ \Gamma_5 pr - \Gamma_4(p^2 - r^2) \\ \Gamma_6 pq - \Gamma_1 qr \end{pmatrix} + \begin{pmatrix} \Gamma_3 l + \Gamma_4 n \\ \frac{1}{J_y} m \\ \Gamma_4 l + \Gamma_7 n \end{pmatrix} \quad (2.5a)$$

where:

$$\Gamma \triangleq J_x J_z - J_{xz}^2 \quad (2.5b)$$

$$\Gamma_1 = \frac{J_{xz}(J_x - J_y + J_z)}{\Gamma} \quad (2.5c)$$

$$\Gamma_2 = \frac{J_z(J_z - J_y) + J_{xz}^2}{\Gamma} \quad (2.5d)$$

$$\Gamma_3 = \frac{J_z}{\Gamma} \quad (2.5e)$$

$$\Gamma_4 = \frac{J_{xz}}{\Gamma} \quad (2.5f)$$

$$\Gamma_5 = \frac{J_z - J_x}{J_y} \quad (2.5g)$$

$$\Gamma_6 = \frac{1}{J_y} \quad (2.5h)$$

$$\Gamma_7 = \frac{J_x(J_x - J_y) + J_{xz}^2}{\Gamma} \quad (2.5i)$$

$$\Gamma_8 = \frac{J_x}{\Gamma} \quad (2.5j)$$

$$\begin{pmatrix} L_p \\ M_p \\ N_p \end{pmatrix} = \begin{pmatrix} L_T \\ M_T \\ N_T \end{pmatrix} \quad (2.5k)$$

$$\begin{pmatrix} l \\ m \\ n \end{pmatrix} = \begin{pmatrix} \frac{1}{2}\rho V_{air}^2 S b C_l \\ \frac{1}{2}\rho V_{air}^2 S \bar{c} C_m \\ \frac{1}{2}\rho V_{air}^2 S b C_n \end{pmatrix} \quad (2.5l)$$

### 2.3.2 UAV Orientation and Position

- **Kinematic Equations:** The orientation of the airplane can be described by three consecutive rotations whose order is important. The angular rotations are called the Euler angles.

The relationship between the angular velocities in the body frame ( $p$ ,  $q$  and  $r$ ) and the Euler rates ( $\dot{\psi}$ ,  $\dot{\theta}$ , and  $\dot{\phi}$ ) is shown in Equation 2.6.

$$\begin{pmatrix} p \\ q \\ r \end{pmatrix} = \begin{pmatrix} 1 & 0 & -\sin \theta \\ 0 & \cos \phi & \cos \theta \sin \phi \\ 0 & -\sin \phi & \cos \theta \cos \phi \end{pmatrix} \begin{pmatrix} \dot{\phi} \\ \dot{\theta} \\ \dot{\psi} \end{pmatrix} \quad (2.6)$$

Equation 2.6 can be solved for the Euler rates in terms of the body angular velocities:

$$\begin{pmatrix} \dot{\phi} \\ \dot{\theta} \\ \dot{\psi} \end{pmatrix} = \begin{pmatrix} 1 & \sin \phi \tan \theta & \cos \phi \tan \theta \\ 0 & \cos \phi & -\sin \phi \\ 0 & \sin \phi \sec \theta & \cos \phi \sec \theta \end{pmatrix} \begin{pmatrix} p \\ q \\ r \end{pmatrix} \quad (2.7)$$

By integrating these equations, one can determine the Euler angles  $\psi$ ,  $\theta$ , and  $\phi$ .

- **Navigation Equations:** The state variables  $p_n$ ,  $p_e$ , and  $p_d$  are inertial frame position quantities, whereas the velocities  $u$ ,  $v$ , and  $w$  are body frame quantities. Therefore the relationship between the position and velocities if we account for the wind ( $w_n$ ,  $w_e$ , and  $w_d$ ) represented in the inertial frame is given by

Equation 2.8.

$$\begin{pmatrix} \dot{p}_n \\ \dot{p}_e \\ \dot{p}_d \end{pmatrix} = \begin{pmatrix} \cos \theta \cos \psi & \sin \phi \sin \theta \cos \psi - \sin \psi \cos \phi & \cos \phi \sin \theta \cos \psi + \sin \psi \sin \phi \\ \cos \theta \sin \psi & \cos \phi \sin \theta \cos \psi + \sin \psi \cos \phi & \cos \phi \sin \theta \sin \psi - \cos \psi \sin \phi \\ -\sin \theta & \sin \phi \cos \theta & \cos \phi \cos \theta \end{pmatrix} \begin{pmatrix} u \\ v \\ w \end{pmatrix} + \begin{pmatrix} w_n \\ w_e \\ w_d \end{pmatrix} \quad (2.8)$$

## 2.4 AERODYNAMIC COEFFICIENTS FOR FORCES AND MOMENTS

### 2.4.1 Aerodynamic Forces

The resultant aerodynamic force is the integrated effect of the pressure and skin friction caused by the flow of air over the surface of the UAV. The lift and the drag are the components of the resultant aerodynamic force perpendicular and parallel to the velocity vector. Both the lift and the drag forces satisfy equations 2.9 and 2.10 respectively :

$$L = \frac{1}{2} \rho V_{air}^2 S C_L \quad (2.9)$$

$$D = \frac{1}{2} \rho V_{air}^2 S C_D \quad (2.10)$$

Where:

$C_L$ : is the *Lift coefficient*.

$C_D$ : is the *Drag coefficient*.

$\rho$ : is the *atmosphere density* at the altitude of the UAV.

$V_{air}$ : is the *UAV Velocity* relative to the atmosphere.

$S$ : is the *Wing Surface Area*.

If the equations governing the motion of air and the boundary conditions are nondimensionalized, the integration of the pressure and skin friction coefficients over the surface of the UAV leads to the following functional relations for the lift coefficient,



the drag coefficient and the side force coefficient for a constant geometry UAV:

$$C_L = C_{L_o} + C_{L_\alpha} \alpha + C_{L_{\delta_e}} \delta_e + \frac{\bar{c}}{2V_{air}} (C_{L_{\dot{\alpha}}} \dot{\alpha} + C_{L_q} q) \quad (2.11)$$

$$C_D = C_{D_o} + \frac{(C_L - C_{L_o})^2}{\pi e AR} + C_{D_{\delta_a}} \delta_a + C_{D_{\delta_e}} \delta_e + C_{D_{\delta_r}} \delta_r \quad (2.12)$$

$$C_Y = C_{Y_\beta} \beta + C_{Y_{\delta_a}} \delta_a + C_{Y_{\delta_r}} \delta_r + \frac{b}{2V_{air}} (C_{Y_p} p + C_{Y_r} r) \quad (2.13)$$

#### 2.4.2 Aerodynamic Moments

The aerodynamic moments are build from the following moment coefficients:

$$C_l = C_{l_\beta} \beta + C_{l_{\delta_a}} \delta_a + C_{l_{\delta_r}} \delta_r + \frac{b}{2V_{air}} (C_{l_p} p + C_{l_r} r) \quad (2.14)$$

$$C_m = C_{m_o} + C_{m_\alpha} \alpha + C_{m_{\delta_e}} \delta_e + \frac{\bar{c}}{2V_{air}} (C_{m_{\dot{\alpha}}} \dot{\alpha} + C_{m_q} q) \quad (2.15)$$

$$C_n = C_{n_\beta} \beta + C_{n_{\delta_a}} \delta_a + C_{n_{\delta_r}} \delta_r + \frac{b}{2V_{air}} (C_{n_p} p + C_{n_r} r) \quad (2.16)$$

## 2.5 IMPLEMENTATION OF THE ARF60 AUS-UAV NONLINEAR MODEL IN SIMULINK

The forces and moments described in Section 2.3 can now be implemented in Simulink environment. Simulink block-diagrams, are flexible, and more user-friendly than other models proposed in the literature (Rauw, 1992). With the presence of the Aerosim and Aerospace Simulink based Blocksets, adding new output equations, deleting unwanted relations, or changing sub models to implement other aircraft is now straightforward. Figure 2.9, shows the general structure of the ARF60 AUS-UAV Simulink nonlinear model.

Most of the subsystems were designed using the AeroSim and Aerospace blocks. The propulsion and actuators models were modelled experimentally as it will be described in the System identification chapter 3. The aerodynamics, propulsion, and inertia models compute the airframe loads (forces and moments) as functions of

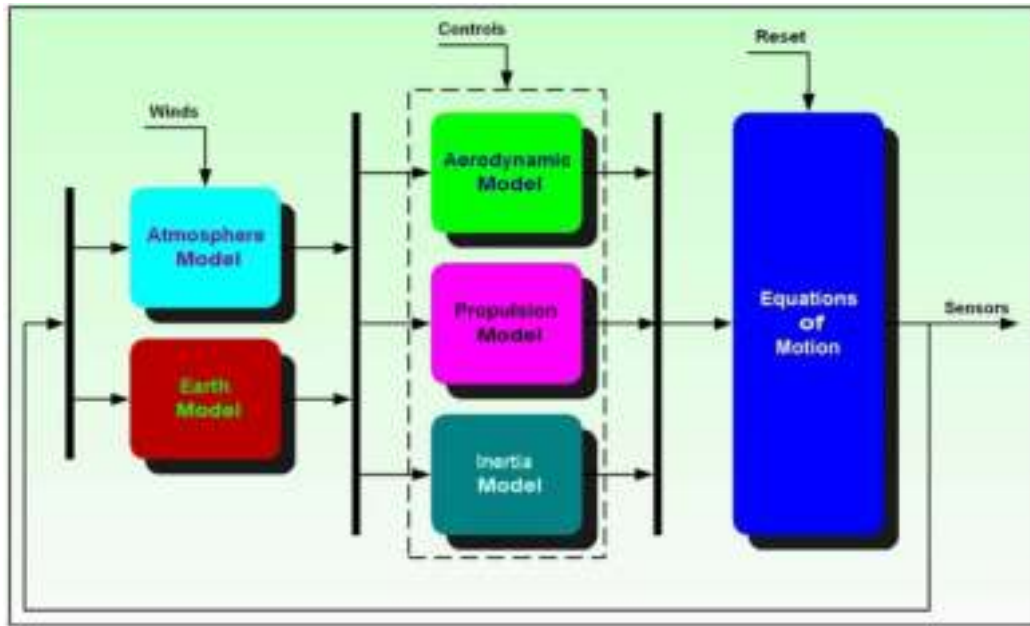


Figure 2.9: ARF60 UAV Simulink Model general Structure

control inputs and environment (atmosphere and Earth) effects. The resulting accelerations are then integrated by the Equations of Motion to obtain the aircraft states (position, velocity, attitude, angular velocities). The aircraft states will affect the output of the environment blocks at the next iteration (for example altitude changes result in atmospheric pressure changes, latitude and longitude variations result in gravity variations). Also, the aircraft states are used in the computation of sensor outputs (GPS, inertial measurements, etc.).

## CHAPTER 3

# ARF60 AUS-UAV MODELING AND SYSTEM IDENTIFICATIONS

After introducing the dynamics of a conventional aircraft in Chapter 2, this chapter provides the identified model that reflects our ARF60 AUS-UAV. This identification includes, aerodynamic parameters, mass moment of inertia, propulsion model and the actuators models.

### 3.1 INTRODUCTION

One of the oldest and most fundamental of all human scientific pursuits is developing mathematical models for physical systems based on imperfect observations or measurements. This activity is known as system identification. A good practical definition is that of (Zadeh, 2007):

*System identification is the determination, on the basis of observation of input and output, of a system within a specified class of systems to which the system under test is equivalent.*

Implicit in the preceding definition is the practical fact that the mathematical model of a physical system is not unique. In general, the guiding principle for model selection is the parsimony principle, which states that of all models in specified class that exhibit the desired characteristics, the simplest one should be preferred. There are both theoretical and practical reasons for the parsimony principle, and these were discussed further throughout (Vladislav Klein & Eugene A. Morell, 2006). The preceding definition also mentions that system identification is based on observations of input and output for the system under test. In practise, these observations are corrupted by measurement noise.

The most important requirement for a mathematical model is that it be useful in some way. This means that the model can be used to predict some aspects of the behavior of a physical system, while at other times it can just predict the values of desired parameters. In any case, the synthesized model must be simple enough to be useful and at the same time complex enough to capture important dependencies and features embodied in the observations or measurements.

### 3.2 OVERVIEW OF UAV SYSTEM ID AND LITERATURE REVIEW

In aircraft dynamics and control, system identification techniques are used to obtain refined aerodynamic model, propulsion system model, and control actuators models as shown in Figure 3.1.

In the present investigation, the identification model will be used in the following objectives:

1. Find the system mathematical model  $S$ , given the input  $u$  and the output  $y$ .
2. Find the input  $u$  to get the output  $y$ , given the system mathematical model  $S$  (for the autopilot system design)
3. Find the output  $y$  for the input  $u$ , given the system mathematical model  $S$  (for the hardware in the loop simulation).

As indicated earlier in Chapter 2 an aircraft can be modeled as a rigid body, whose motion is governed by Newton laws. System identification techniques need to be used to characterize applied forces and moments acting on the aircraft that arise from aerodynamics and propulsion. Typically, thrust forces and moments are obtained from ground tests, so aircraft system identification is applied to model the functional dependence of aerodynamic forces and moments on aircraft motion and control variables. Modern computational methods and wind-tunnel can provide, in many instances, comprehensive data about the aerodynamic characteristics of an aircraft. However, there are still several motivations for identifying aircraft models from flight-test data, including

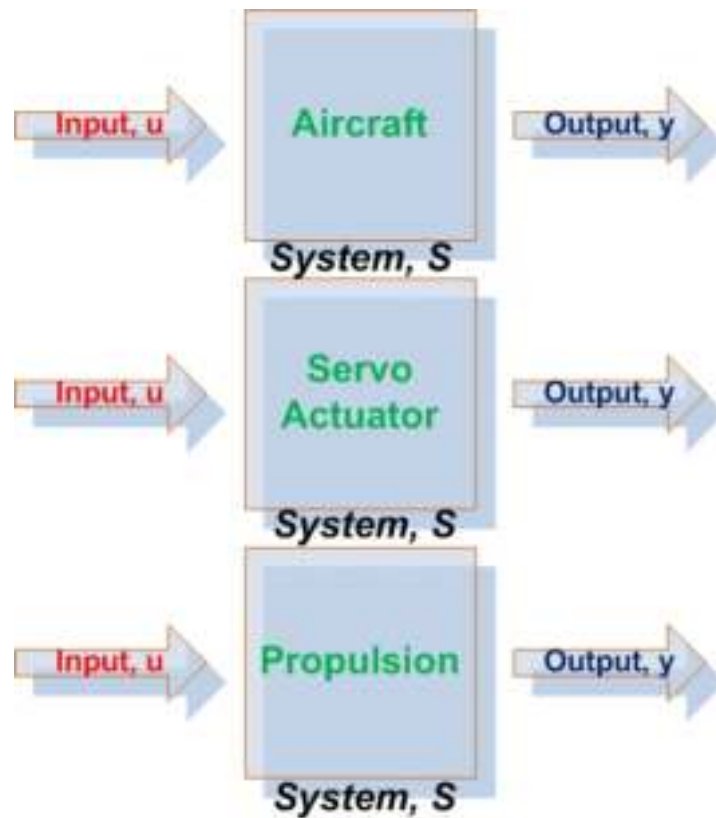


Figure 3.1: UAV components dynamics and control

1. Verifying and interpreting theoretical predictions and wind-tunnel test results (flight-test results can also be used to help improve ground based predictive methods);
2. Obtaining more accurate and comprehensive mathematical models of aircraft dynamics, for use in designing stability augmentation system and flight control systems;
3. Developing flight simulators, which require accurate representation of the aircraft in all flight modes and regimes (many aircraft motions and flight conditions simply cannot be duplicated in the wind tunnel nor computed analytically with sufficient accuracy or computational efficiency);
4. Verifying aircraft specification compliance.

Recently, several papers discussed new system identification algorithms. Those techniques have been proposed for the modelling of nonlinear systems. Fuzzy identification (Li-Xin Wang, 1995), state space identification (Shaaban, A., 2006), frequency domain analysis (R. Pintelon & J. Schoukens., 2001), artificial neural networks are

some of the prominent ones. On the other hand, in (Chunhua Hu & Zhu, 2004) they used an easy to implement system identification process. System identification for a small UAVs take-off process based on operator's control was carried out. The auto-regressive exogenous *ARX*, auto-regressive moving average exogenous *ARMAX* and Box-Jenkins *BJ* models were used to describe the dynamics of BlueEagles speeding up before take-off where they have better input-output fits. Using input and output data of actual flying test, system identification results were shown through numerical analysis. Validated by input and output data of other actual flying test, the resulting model was acceptable.

### 3.3 SYSTEM ID STEPS

The System Identification problem is to estimate a model of a system based on observed input-output data. Several ways to describe a system and to estimate such descriptions exist. This section gives a brief account of the most important approaches. The procedure to determine a model of a dynamical system from observed input-output data involves three basic ingredients. Which are input-output measurement data, set of candidate structure models and identification method selection.

The identification process amounts to repeatedly selecting a model structure, computing the best model in the structure, and evaluating this models properties to see if they are satisfactory. The cycle can be itemized as follows:

1. Experimental Design: Its purpose is to obtain good experimental data, and it includes the choice of the measured variables and of the character of the input signals.
2. Data Examination: Polish the measured data so as to remove trends and outliers, select useful portions of the original data, and apply filtering to enhance important frequency ranges.
3. Model Structure Selection: A suitable model structure is chosen using prior knowledge and trial and error.
4. Choosing the Criterion to Fit : A suitable cost function is chosen, which reflects how well the model fits the experimental data.

5. Parameter estimation: An optimization problem is solved to obtain the numerical values of the model parameters.
6. Model validation: The model is tested in order to reveal its validity.

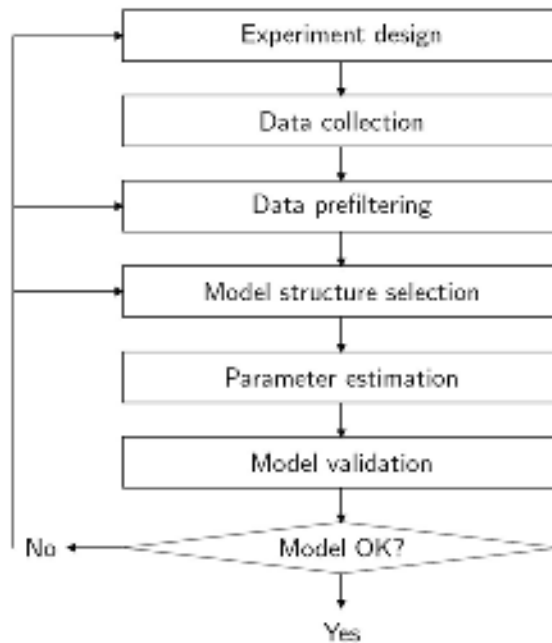


Figure 3.2: System Identification Steps

A flow chart describing the previous steps is shown in Figure 3.2. If the model is good enough, then the work is completed; otherwise we go back to Step 3 and try another model. Possibly, we can try other estimation methods (Step 4) or work further on the input-output data (Steps 1 and 2).

### 3.4 AIRCRAFT SYSTEM ID

#### 3.4.1 Aerodynamic Numerical modeling

Aircraft aerodynamics can be modeled using linear coefficients estimated based on aircraft geometry. Aircraft mass and CG location are too important quantities that need to be identified. The center of gravity location was carefully determined in the body axes, it was taken at the point where the aircraft has a static balance. As shown in Figures 3.3 two lines were drawn on the two planes ( $x-y$  &  $x-z$ ). Another line was drawn on the ( $x-y$ ) to get the intersection with the depth of the ( $x-z$ ) mark; Figure 3.4. The gross and empty weight of the UAV and the landing wheels were



Figure 3.3: CG location Experiment top

measured using a precise scale. The added masses ie.IMU, Autopilot, batteries, etc. were weighed later. All of this data listed in Table 3.1 was entered to MATLAB script to estimate the stability derivatives. The stability derivatives resulted from the MATLAB script based on the linearized model of the aerodynamic forces and moments are summarized in Table 3.2



Figure 3.4: CG location Experiment



Table 3.1: ARF60 measured geometric parameters - input to the MATLAB script

Property	Symbol	Value	Unit(SI)
Empty Aircraft Mass (without fuel)	$m_E$	3.416	$Kg$
Gross Aircraft Mass (with fuel)	$m_G$	3.5105	$Kg$
Center of Gravity Location ( $x, y, z$ )	$CG$	[0.00 0.00 0.00]	$m$
Roll Inertia	$I_{xx}$	0.19969	$kg.m^2$
Pitch Inertia	$I_{yy}$	0.24086	$kg.m^2$
Yaw Inertia	$I_{zz}$	0.396	$kg.m^2$
Wing			
Length of Mean Aerodynamic Cord	$\bar{C}$	0.324	$m$
Wing Span	$b$	1.87	$m$
Wing Dihedral Angle	$\Gamma$	6	$deg$
Wing Taper Ratio	$\lambda$	1	—
Wing Surface Area	$S$	0.6059	$m^2$
Ailerons Surface Area	$S_a$	0.0581	$m^2$
Ailerons Around Area	$A_a$	0.4277	$m^2$
Horizontal Tail			
Horizontal Tail Span	$b_t$	0.6700	$m$
Horizontal Tail Mean Aerodynamic Cord	$\bar{C}_t$	0.1950	$m$
Horizontal Tail Area	$S_t$	0.1307	$m^2$
Elevator Surface Area	$S_e$	0.0232	$m^2$
Distance from CG to H.Tail Quarter Cord	$l_t$	0.8200	$m$
Horizontal Tail Volume Ratio	$V_H$	0.5457	—
Vertical Tail			
Vertical Tail Span	$b_v$	0.2350	$m$
Vertical Tail Mean Aerodynamic Cord	$\bar{C}_v$	0.2150	$m$
Vertical Tail Area	$S_v$	0.0505	$m^2$
Rudder Surface Area	$S_r$	0.1307	$m^2$
Distance from CG to V.Tail Aerodynamic Center	$l_t$	0.8400	$m$
Vertical Tail Volume Ratio	$V_v$	0.2162	—

### 3.4.2 Flight Tests Based System ID

#### Experimental Design

Several flight tests for system identification were conducted. The block diagram for system identification is shown in Figure 3.5, where  $\delta_a, \delta_e, \delta_r, \delta_t$  are input signals for identification and the euler angles:  $\phi, \theta, \psi$ , accelerations:  $a_x, a_y, a_z$ , angular rates:  $p, q, r$ , position:  $Lat, Lon, Alt$ , speed:  $V_x, V_y, V_z$ , Static and differential pressure for altitude and true airspeed are the output signals for identification. Extensive flying tests were conducted, from which, one data set was selected for system identification. The input data acquired from this experiment is shown in Figure 3.6. This data shows the actual deflections of the actuators according to the servo inputs commanded by

Table 3.2: Stability derivatives of the ARF60 UAV (All units per radian)

Symbol	Derivative	Value
Lift coefficient		
$C_{L_0}$	Zero alpha lift	0.4100
$C_{L_\alpha}$	Alpha derivative	4.3842
$C_{L_{\alpha_t}}$	Alpha derivative for the tail	3.6369
$C_{L_{\alpha_v}}$	Alpha derivative for the vertical tail	0.9114
$C_{L_{\delta_e}}$	Pitch control (elevator) derivative	0.3059
$C_{L_{\dot{\alpha}}}$	Alpha-dot derivative	0
$C_{L_q}$	Pitch rate derivative	0.6431
Drag coefficient		
$C_{D_0}$	Minimum drag	0.0500
$C_{D_{\delta_e}}$	Pitch control (elevator) derivative	0
$C_{D_{\delta_a}}$	Roll control (aileron) derivative	0
$C_{D_{\delta_r}}$	Yaw control (rudder) derivative	0
Side force coefficient		
$C_{Y_\beta}$	Sideslip derivative	-0.1795
$C_{Y_{\delta_a}}$	Roll control derivative	0
$C_{Y_{\delta_r}}$	Yaw control derivative	0.1132
$C_{Y_p}$	Roll rate derivative	0
$C_{Y_r}$	Yaw rate derivative	0
Pitch moment coefficient		
$C_{m_0}$	Zero alpha pitch	0
$C_{m_\alpha}$	Alpha derivative	0
$C_{m_{\delta_e}}$	Pitch control derivative	-0.7741
$C_{m_{\dot{\alpha}}}$	Alpha dot derivative	-6.0730
$C_{m_q}$	Pitch rate derivative	-10.0467
Roll moment coefficient		
$C_{l_\beta}$	Sideslip derivative	-0.0013
$C_{l_{\delta_a}}$	Roll control derivative	0.8275
$C_{l_{\delta_r}}$	Yaw control derivative	0.0036
$C_{l_p}$	Roll rate derivative	-1.8267
$C_{l_r}$	Yaw rate derivative	0.0052
Yaw moment coefficient		
$C_{n_\beta}$	Sideslip derivative	0.4653
$C_{n_{\delta_a}}$	Roll control derivative	-0.1357
$C_{n_{\delta_r}}$	Yaw control derivative	-0.2934
$C_{n_p}$	Roll rate derivative	-1.8267
$C_{n_r}$	Yaw rate derivative	-0.2934

the pilot. we tried to excite the aircraft dynamics by introducing series of doublets on the aileron, elevator, rudder and throttle actuators. The output data according to this input signals are shown in Figures 3.7-3.12.

The aerodynamic coefficients are identified from real flight tests using measurements from accelerometers and rate gyros. The aerodynamic force coefficients are

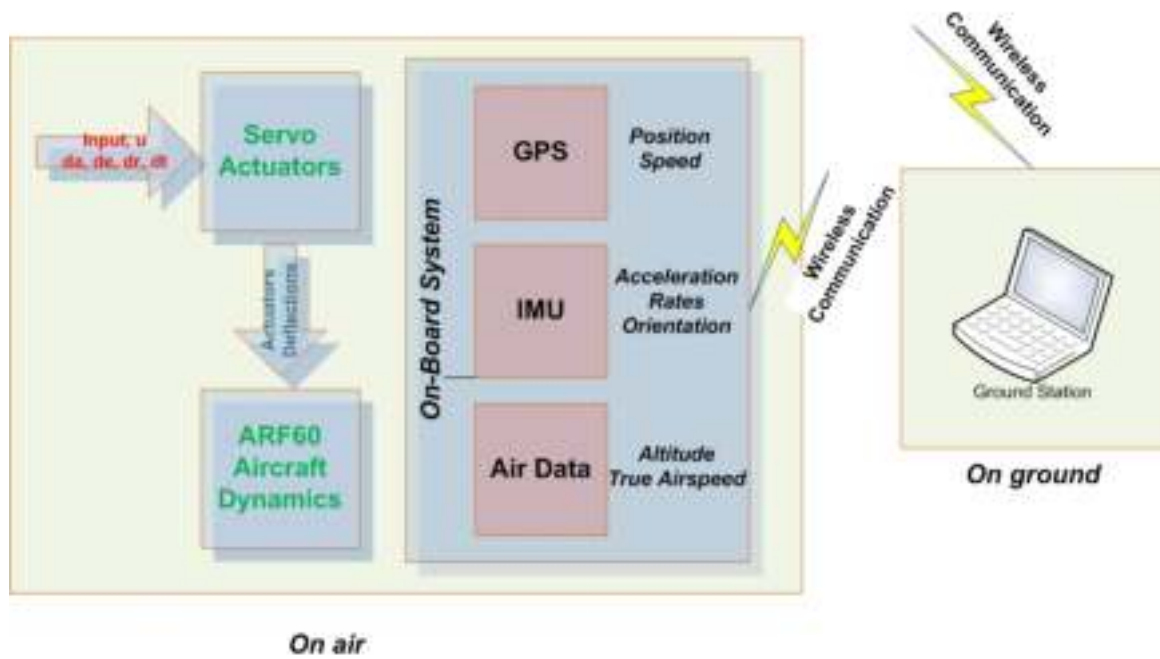


Figure 3.5: Construction of System identification for the ARF60 UAV

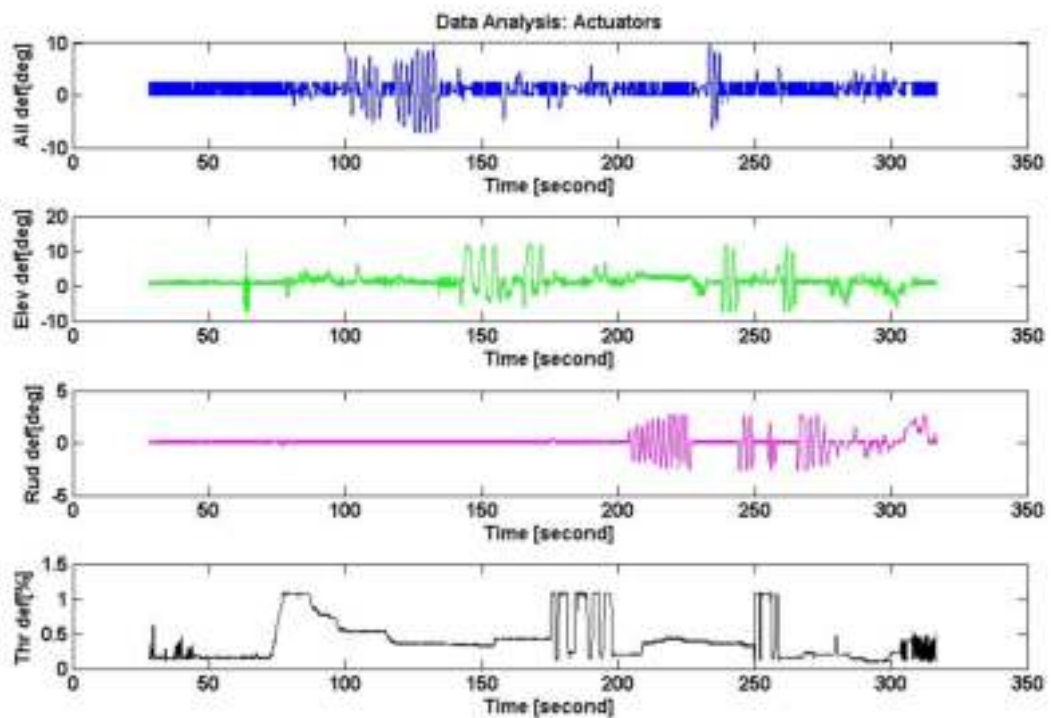


Figure 3.6: ARF60 Actuators deflections during the system identification test

calculated in the body frame using Equations 3.1 by assuming that the thrust force

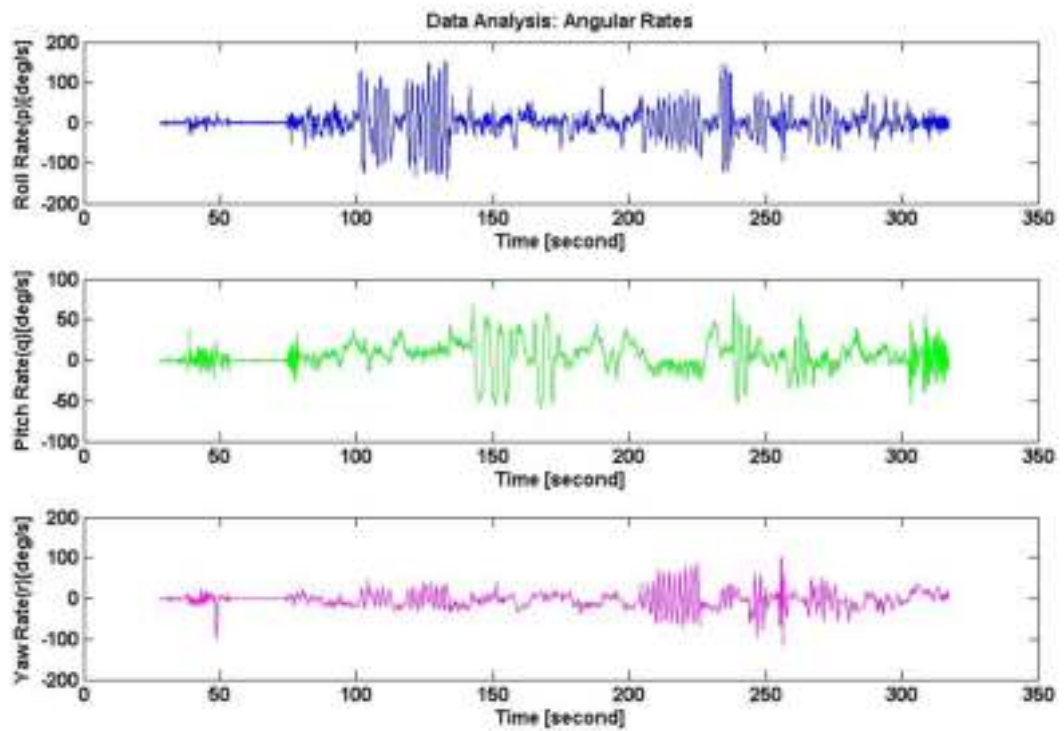


Figure 3.7: ARF60 Angular Rates during the system identification test

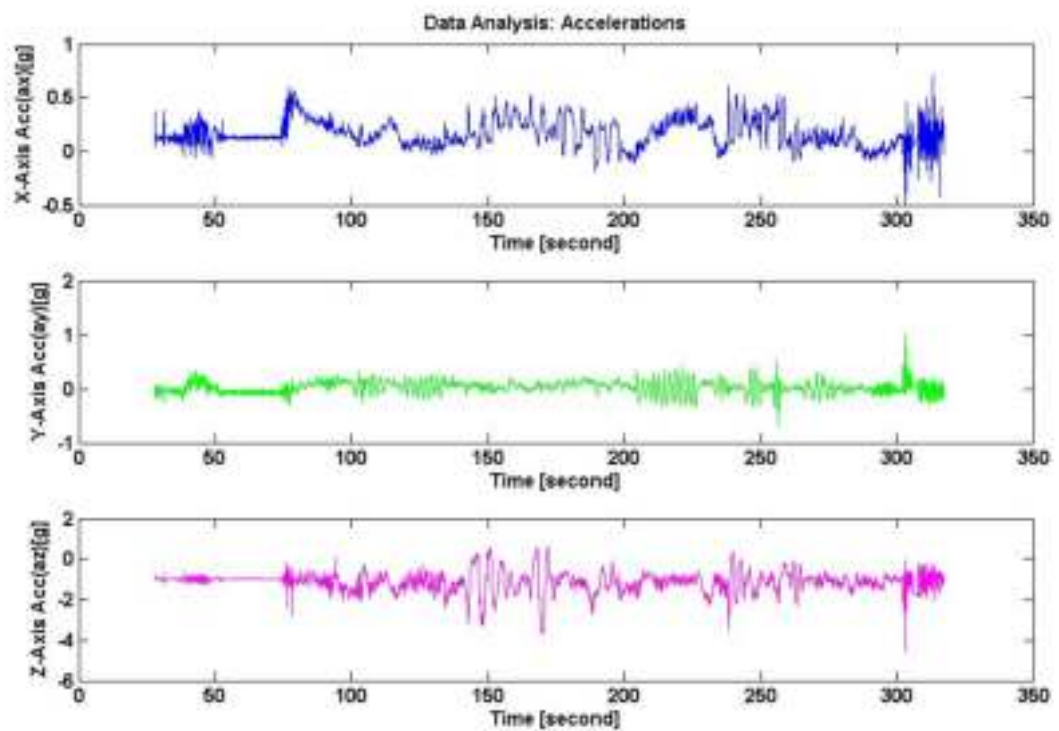


Figure 3.8: ARF60 Accelerations during the system identification test

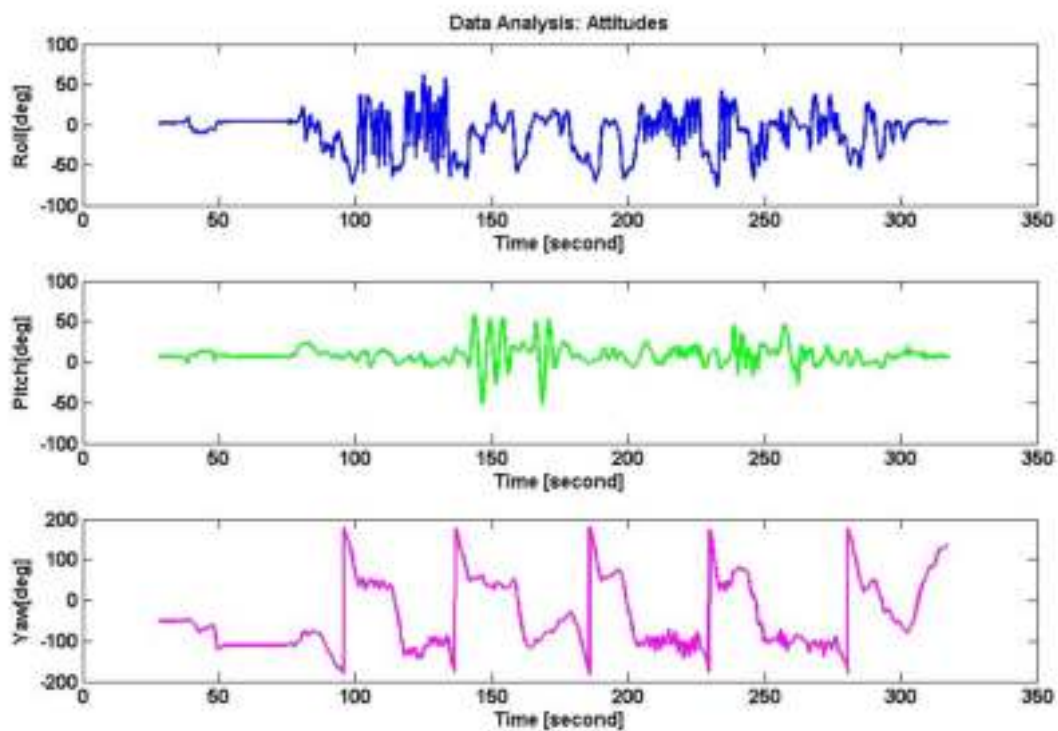


Figure 3.9: ARF60 Attitudes during the system identification test

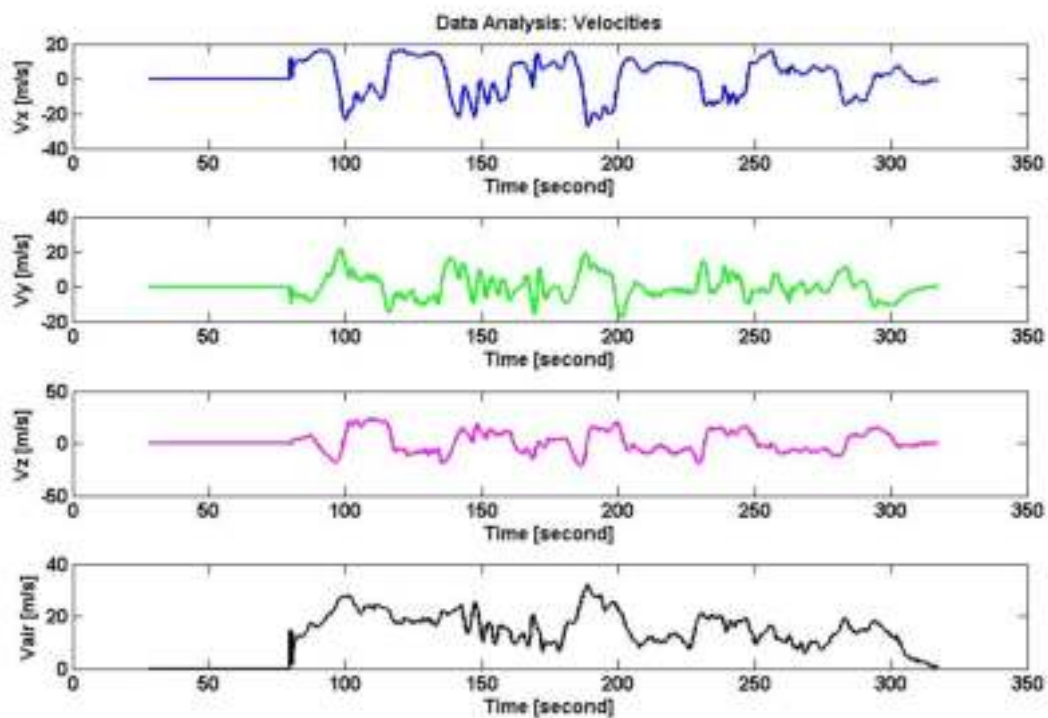


Figure 3.10: ARF60 Velocities during the system identification test

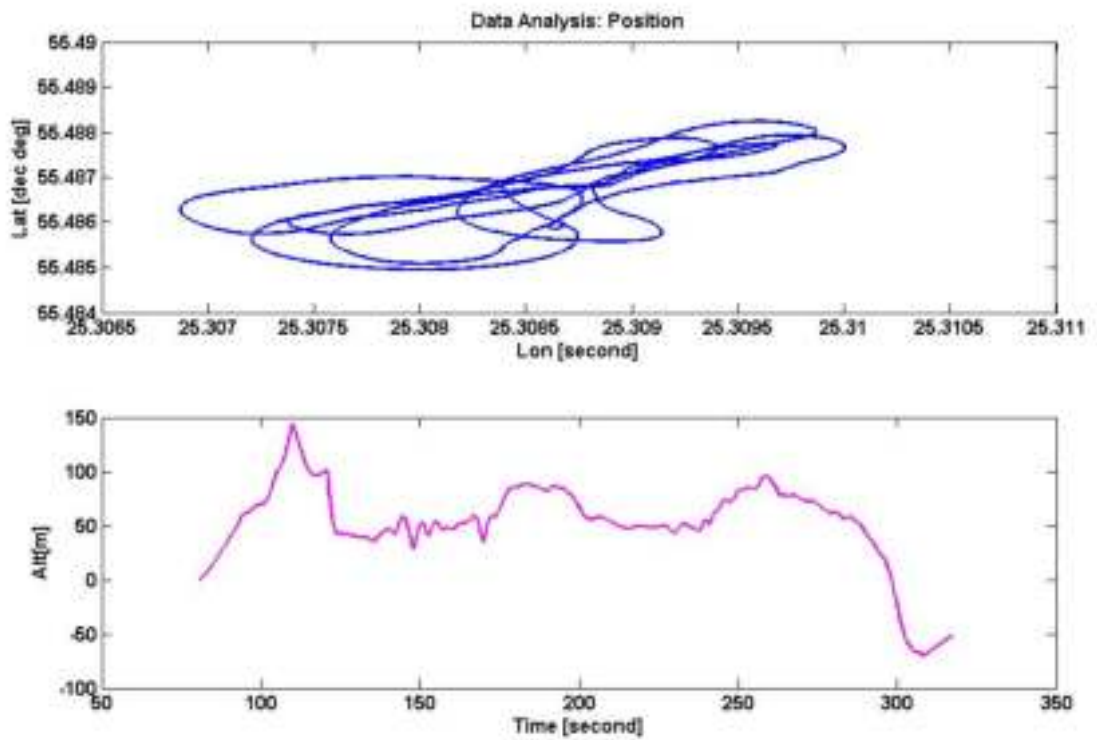


Figure 3.11: ARF60 Position during the system identification test

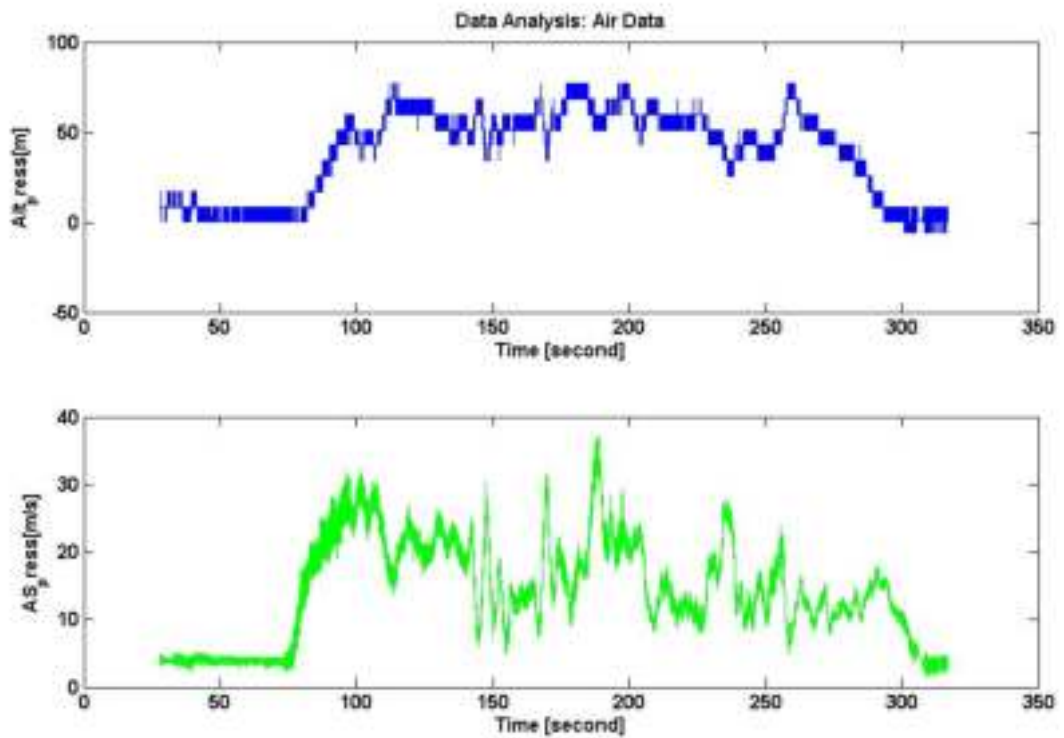


Figure 3.12: ARF60 Air Data during the system identification test

is applied only along the body x-axis.

$$C_X = \frac{m}{\bar{q}S} a_x - \frac{T}{\bar{q}S} \quad (3.1a)$$

$$C_Y = \frac{m}{\bar{q}S} a_y \quad (3.1b)$$

$$C_Z = \frac{m}{\bar{q}S} a_z \quad (3.1c)$$

The aerodynamic moment coefficients are also calculated in the body frame using Equations 3.2 where  $L, M$  and  $N$  are calculated using Equation 2.5.

$$C_\ell = \frac{L}{\bar{q}Sb} \quad (3.2a)$$

$$C_m = \frac{M}{\bar{q}S\bar{c}} \quad (3.2b)$$

$$C_n = \frac{N}{\bar{q}Sb} \quad (3.2c)$$

After identifying the aerodynamic Force/Moment coefficients, a linear regression model was derived based on the decoupled longitudinal and lateral dynamics of the aircraft (Dongwon Jung & Panagiotis Tsiotras, 2007). The formed regressions model is expressed in Equations 3.3

$$C_X = C_{x_o} + C_{x_\alpha} \alpha + C_{x_q} \frac{\bar{c}}{2V_T} q + C_{x_{\delta e}} \delta e \quad (3.3a)$$

$$C_Y = C_{y_o} + C_{y_\beta} \beta + C_{y_p} \frac{b}{2V_T} p + C_{y_r} \frac{b}{2V_T} r + C_{y_{\delta a}} \delta a + C_{y_{\delta r}} \delta r \quad (3.3b)$$

$$C_Z = C_{z_o} + C_{z_\alpha} \alpha + C_{z_q} \frac{\bar{c}}{2V_T} q + C_{z_{\delta e}} \delta e \quad (3.3c)$$

$$C_\ell = C_{L_o} + C_{\ell_\beta} \beta + C_{\ell_p} \frac{b}{2V_T} p + C_{\ell_r} \frac{b}{2V_T} r + C_{\ell_{\delta a}} \delta a + C_{\ell_{\delta r}} \delta r \quad (3.3d)$$

$$C_m = C_{m_o} + C_{m_\alpha} \alpha + C_{m_q} \frac{\bar{c}}{2V_T} q + C_{m_{\delta e}} \delta e \quad (3.3e)$$

$$C_n = C_{n_o} + C_{n_\beta} \beta + C_{n_p} \frac{b}{2V_T} p + C_{n_r} \frac{b}{2V_T} r + C_{n_{\delta a}} \delta a + C_{n_{\delta r}} \delta r \quad (3.3f)$$

From Equations 3.3, it is clear that each aerodynamic coefficient is a function of decoupled longitudinal and lateral derivatives, where the stability and control

derivatives are unknown parameters to be estimated using linear regression analysis. Therefore, each aerodynamic coefficient can be expressed in the following form:

$$z = \theta^T x \quad (3.4)$$

Where:

$z$  is the aerodynamic coefficients calculated from Equations 3.1.

$\theta$  is the stability and control derivatives associated with the aerodynamic coefficient

$x$  is the sensor measurements along with the right-hand-side of Equations 3.3.

The stability and control derivatives are then estimated using Equation 3.5 that finds the best fit using least-square optimization problem  $\min \|z - X\theta\|^2$ .

$$\hat{\theta} = (X^T X)^{-1} X z \quad (3.5)$$

#### *Identification Algorithm Validation*

The identification algorithm proposed earlier (Dongwon Jung & Panagiotis Tsiotras, 2007) was implemented using Matlab script. To assure the correctness of the algorithm and its validity, the data was collected using the nonlinear model of the ARF60-UAV implemented earlier using Simulink. The results show that the algorithm is reliable as the coefficients were almost identical with a range of (95-100%) as expected from a simulated data. The stability derivatives resulted from the algorithm along with the numerical identification are summarized in Table 3.3.

### 3.5 OS 61FX ENGINE AND ITS PROPELLER SYSTEM ID

Identifying the OS 61FX Engine and its Propeller was conducted using various model structures including ARMAX, ARX, OE and BJ. The identification results from each model are summarized in Table 3.4.

From Table 3.4, the best model that describes the engine RPM dynamics is the BJ while the worst model is the ARMAX. Figure 3.13 shows graphical fitting percentage for each model structure.

On the other hand, Table 3.5, shows that the best model that describes the engine thrust dynamics is the BJ while the worst model is the ARX. Figure 3.14



Table 3.3: Identified Stability derivatives of the ARF60 UAV (All units per radian) using System ID algorithm

Symbol	ID Algorithm Value	Numerical ID Value
Lift coefficient		
$C_{L_o}$	0.41	0.4100
$C_{L_\alpha}$	4.38416	4.3842
$C_{L_{\delta_e}}$	0.30585	0.3059
$C_{L_q}$	1.096	0.6431
Drag coefficient		
$C_{D_o}$	0.0510	0.0500
$C_{D_{\delta_e}}$	-0.0106	0
$C_{D_{\delta_a}}$	2.55e-04	0
$C_{D_{\delta_r}}$	2.188e-04	0
Side force coefficient		
$C_{Y_\beta}$	-0.17947	-0.1795
$C_{Y_{\delta_a}}$	-2.30e-14	0
$C_{Y_{\delta_r}}$	0.1131	0.1132
$C_{Y_p}$	1.87e-12	0
$C_{Y_r}$	3.02e-15	0
Pitch moment coefficient		
$C_{m_o}$	0.0022	0
$C_{m_\alpha}$	-1.09172	0
$C_{m_{\delta_e}}$	-0.7064	-0.7741
$C_{m_q}$	-16.5758	-10.0467
Roll moment coefficient		
$C_{l_\beta}$	0.00126	-0.0013
$C_{l_{\delta_a}}$	2.06861e-05	0.8275
$C_{l_{\delta_r}}$	0.00363	0.0036
$C_{l_p}$	-0.7306	-1.8267
$C_{l_r}$	0.00517	0.0052
Yaw moment coefficient		
$C_{n_\beta}$	0.46531	0.4653
$C_{n_{\delta_a}}$	-3.392e-06	-0.1357
$C_{n_{\delta_r}}$	-0.2934	-0.2934
$C_{n_p}$	0.5480	-1.8267
$C_{n_r}$	-0.3712	-0.2934

Table 3.4: OS 61FX Engine RPM System ID Results

Model	Model Structure	Fitting %
ARX	arx525	85.38%
ARMAX	amx5111	84.4 %
OE	oe2210	84.91%
BJ	bj11232	85.31%

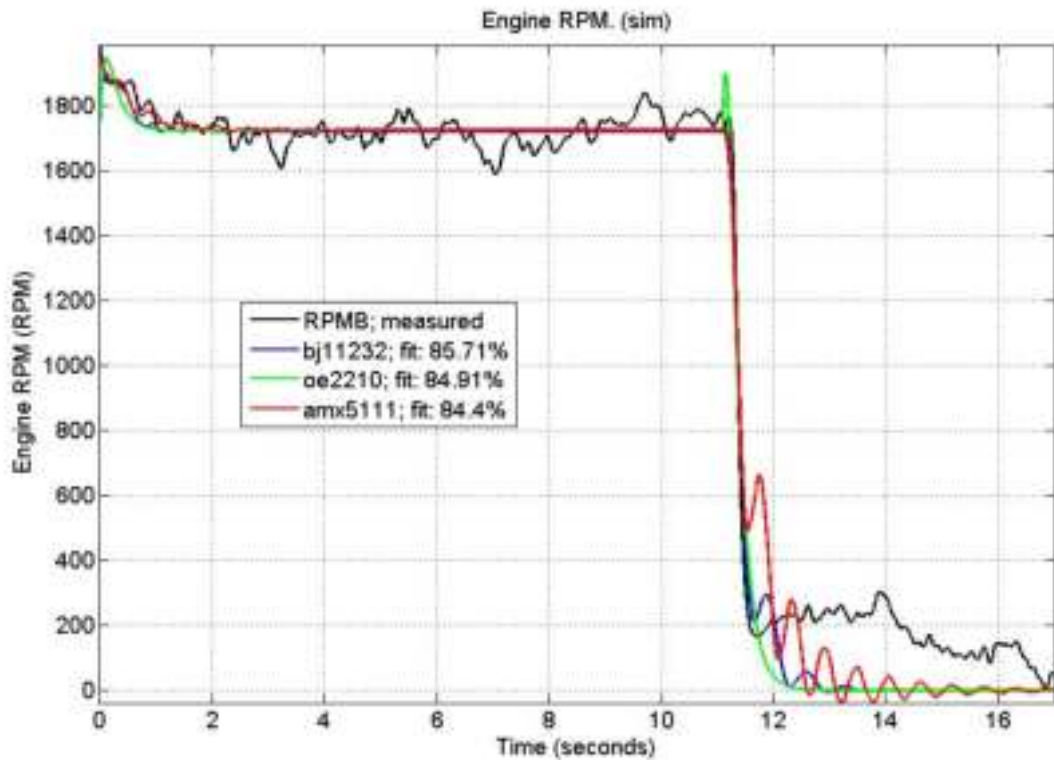


Figure 3.13: The OS 61FX RPM measured output for the validation data set, together with the output from the ARX, ARMAX, OE and BJ models when simulated with the input sequence from the validation data set

Table 3.5: OS 61FX Engine Thrust System ID Results

Model	Model Structure	Fitting %
ARX	arx111	73.56%
ARMAX	amx1131	74.64%
OE	oe617	80.53%
BJ	bj51110	80.58%

shows graphical fitting percentage for each model structure. While Figure 3.15 shows the full raw data measured compared with the model output.

### 3.6 ACTUATOR SYSTEM ID

The control surfaces of the UAV are actuated by four identical R/C servo motors. Each servo arm is coupled to the corresponding control surface via mechanical links. The data collected from the experimental setup (see Figure 3.16) are the servo positions and the control commands. The deflection angles of the control surfaces are measured using potentiometers calibrated using a digital encoder. It appears that

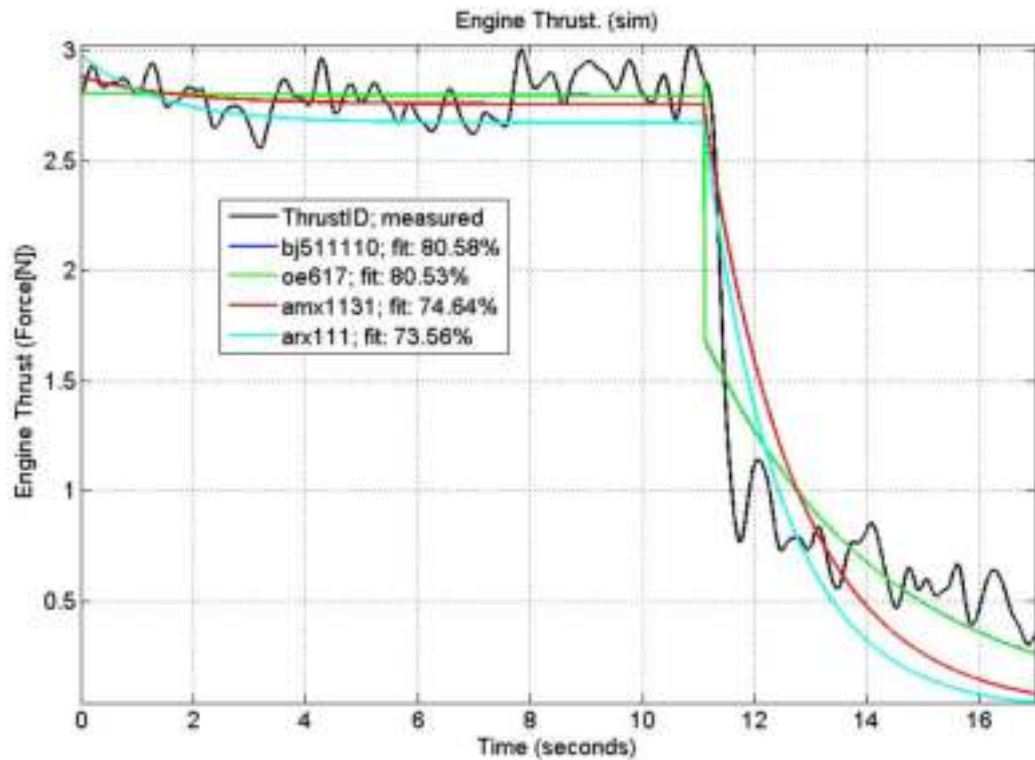


Figure 3.14: The OS 61FX thrust measured output for the validation data set, together with the output from the ARX, ARMAX, OE and BJ models when simulated with the input sequence from the validation data set

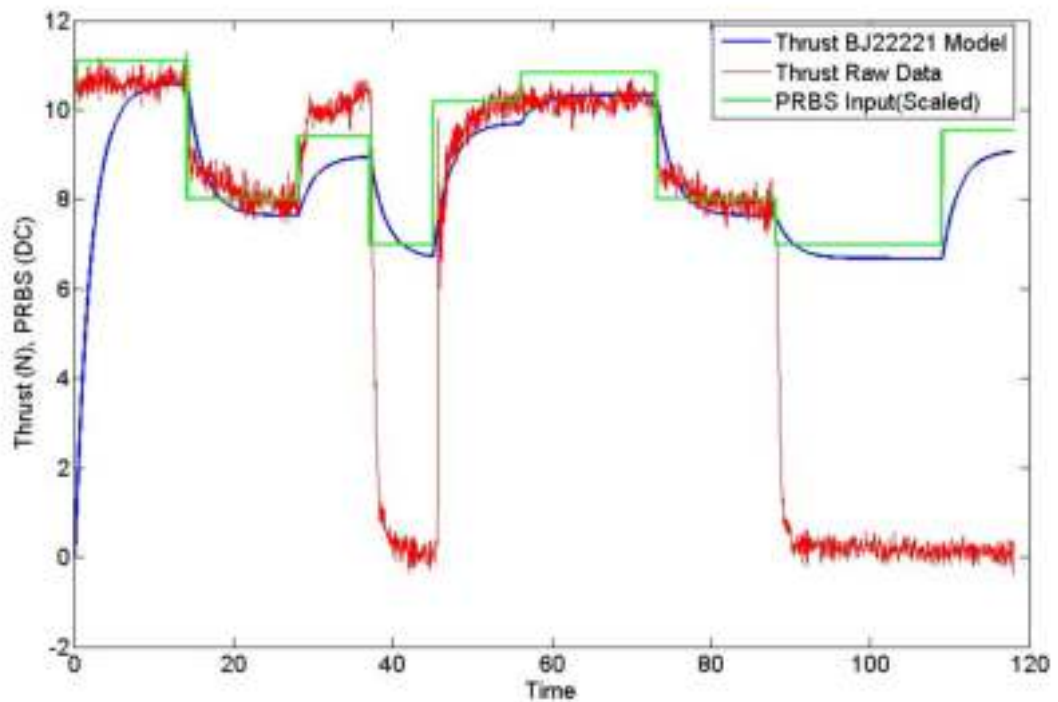


Figure 3.15: Thrust measured output together with the output from the BJ model when simulated with the input PRBS



Figure 3.16: Actuator Identification Setup

an R/C servo motor nearly performs a dead beat control action. Thus, a first-order low pass filter and control saturation results in a good actuator model. Results of all control surfaces models are summarized in Appendix C.1.1.

## CHAPTER 4

# ARF60 AUS-UAV AIRCRAFT NATURAL MOTION, CONTROLLER DESIGN AND SIMULATION

In this chapter we study the stick fixed motion, that is, the motion of the aircraft when all control surfaces are locked in position. Moreover, the aircraft response to actuation of primary controls elevator, aileron, rudder, and throttle also will be studied. The analysis of both the longitudinal and lateral models will be presented in detail in Section 4.1. Next, the autopilot design is considered with linear simulation results in Section 4.2.

### 4.1 AIRCRAFT LINEAR MODEL

The state space linear model of the aircraft was derived using the already available stability derivatives found in Section 3.4.1. The linearized state space model is needed to develop the guidance and control laws. It is used to develop airspeed hold, altitude hold as well as for ground and navigation control. The nonlinear aircraft model is linearized about the trim condition. The derived linear model is then decoupled into a longitudinal and lateral models. The following longitudinal and lateral models were linearized around a typical flight condition ( $V_a = 20m/s$ ,  $h = 100m$ , and  $\phi = 0$ ).

#### 4.1.1 ARF60 UAV Longitudinal Model

The following state space model is the linear longitudinal model for the ARF60 UAV:

$$\begin{aligned}
\begin{pmatrix} \dot{u} \\ \dot{w} \\ \dot{q} \\ \dot{\theta} \\ \dot{h} \end{pmatrix} &= \begin{pmatrix} -0.2289 & 0.3712 & 0 & -9.81 & 0 \\ -1.8772 & -10.1512 & 20 & 0 & 0 \\ 0.9219 & -7.0403 & -26.072 & 0 & 0 \\ 0 & 0 & 1 & 0 & 0 \\ 0 & -1 & 0 & 20 & 0 \end{pmatrix} \begin{pmatrix} u \\ w \\ q \\ \theta \\ h \end{pmatrix} \\
&+ \begin{pmatrix} 0 & 51.5 \\ -14.0042 & 0 \\ -147.6913 & 0 \\ 0 & 0 \\ 0 & 0 \end{pmatrix} \begin{pmatrix} \delta_e \\ \delta_t \end{pmatrix} \quad (4.1)
\end{aligned}$$

Where the state variables  $(u \ w \ q \ \theta \ h)$  refer to the longitudinal velocities,  $u$  and  $w$ , the pitch rate,  $q$  and the angle of inclination,  $\theta$ . In addition to the above states, the altitude  $h$  was augmented to get the full longitudinal dynamics model. The control input  $(\delta_e \ \delta_t)$  is the elevator deflection angle  $\delta_e$ , and the engine throttle lever  $\delta_t$ . The previous longitudinal dynamics are typically resolved into two distinct phugoid and short period modes, which represent the dynamics of the aircraft on different timescales. The short period is characterized by high frequency pitch rate oscillations and can have high or low damping, depending on the stability of the aircraft. In contrast, the phugoid mode is characterized by lightly damped, low frequency oscillations in altitude and airspeed with pitch angle rates,  $q$ , remaining small. The eigenvalues of the full longitudinal state equation can be determined by solving Equation 4.2 The characteristic equation is next calculated as shown in Equation 4.3. Five eigenvalues were found, each corresponding to a state variable, yielding five poles. The altitude's pole is real, as it is an unstable pole and is not considered. The 4 poles yielded two complex conjugate pairs, one for short period (heavily damped) and one for phugoid (long) period (lightly damped). The eigenvalues of the system matrix  $A$  are listed in Table 4.1 and illustrated in Figure 4.1. Figure 4.2 shows the impulse response of the pitch angle to both of the longitudinal inputs (elevator and throttle).

$$|\lambda I - A| = 0 \quad (4.2)$$

Table 4.1: Pole locations, natural frequencies and periods for the longitudinal modes.

	Eigenvalue (Pole)	$\omega_n$ (rad/s)	Period(s)
Mode 1(phugoid mode)	$\lambda_{1,2}=-0.1152 \pm 0.7299i$	7.39e-001 (1.176 Hz)	8.5023
Mode 2(short-period mode)	$\lambda_{3,4}=-18.1110 \pm 8.8071i$	2.01e+001 (3.2 Hz)	0.3126
	$\lambda_5=0$	-	-

$$\lambda^4 + 36.4523\lambda^3 + 414.4618\lambda^2 + 113.1955\lambda + 221.4674 = 0 \quad (4.3)$$

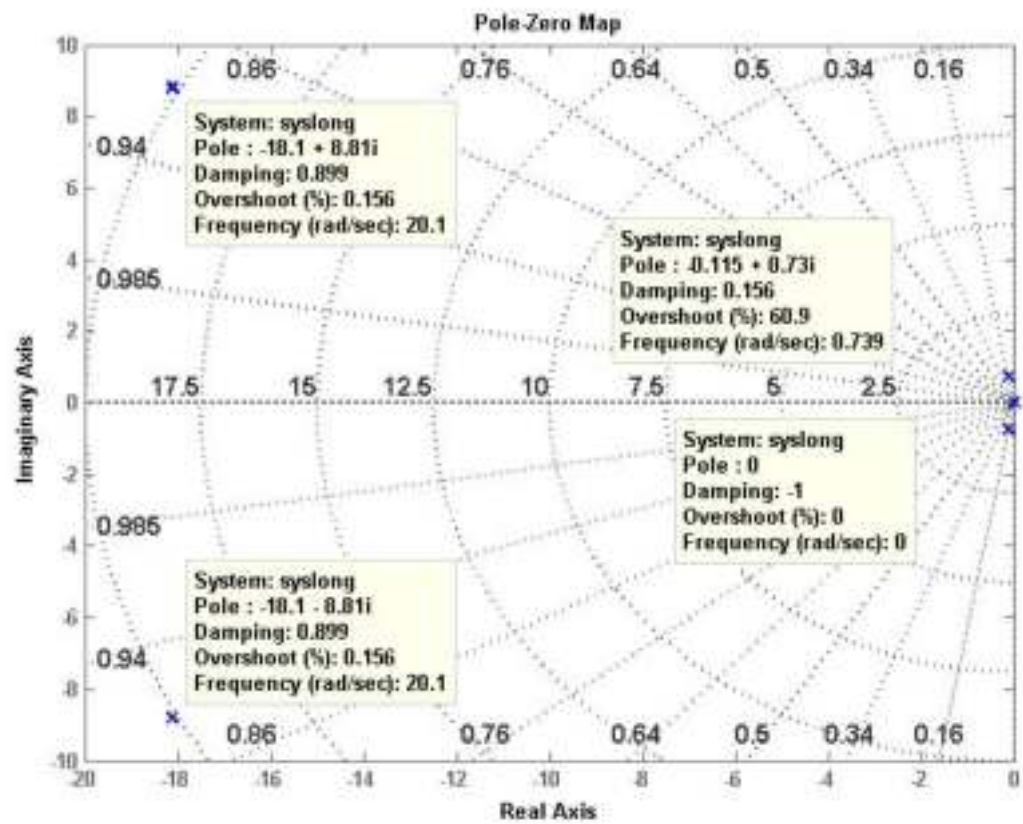


Figure 4.1: Poles Locations for the Longitudinal Model

#### 4.1.2 ARF60 UAV Lateral Model

Similar to the longitudinal model, the dynamics describing lateral perturbations about an equilibrium trim conditions previously mentioned is written below in concise state space form. The eigenvalues of the system matrix  $A$  are listed in Table 4.2 and illustrated in Figure 4.3.

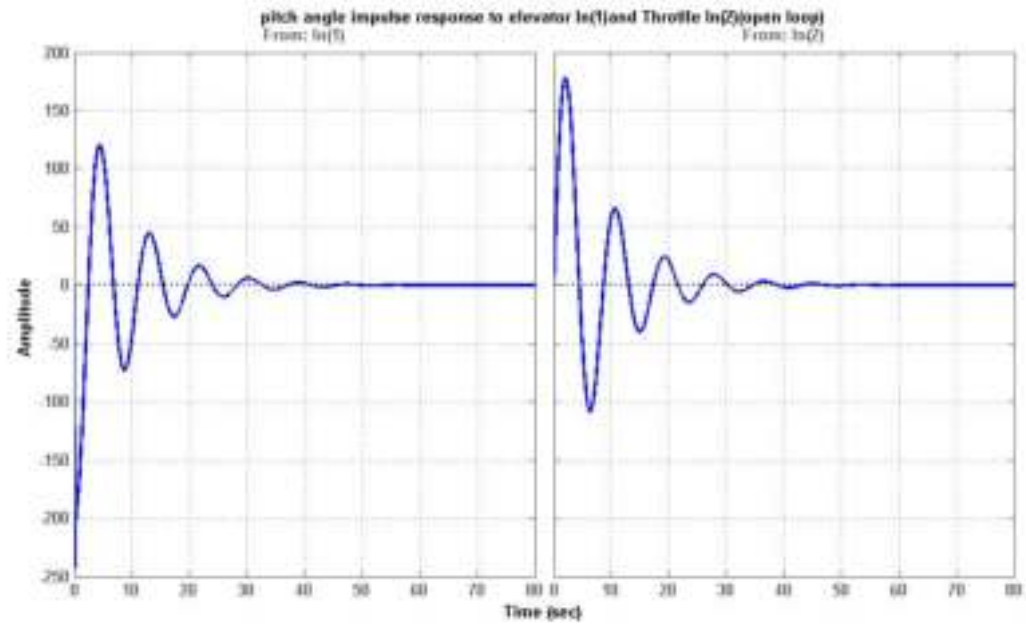


Figure 4.2: Impulse Response for the Longitudinal Model

$$\begin{aligned}
 \begin{pmatrix} \dot{\beta} \\ \dot{p} \\ \dot{r} \\ \dot{\phi} \end{pmatrix} &= \begin{pmatrix} -0.7684 & 0 & -1.0000 & 0.4905 \\ -1.7563 & -47.4848 & 0.3362 & 0 \\ 326.1682 & -17.9588 & -12.1661 & 0 \\ 0 & 1 & 0 & 0 \end{pmatrix} \begin{pmatrix} \beta \\ p \\ r \\ \phi \end{pmatrix} \\
 &+ \begin{pmatrix} 0 & 0.2591 \\ 1150.2319 & 5.0475 \\ -95.1241 & -205.6651 \\ 0 & 0 \end{pmatrix} \begin{pmatrix} \delta_a \\ \delta_r \end{pmatrix} \quad (4.4)
 \end{aligned}$$

Where  $v$  is the sideslip velocity,  $p$  and  $r$  represent the roll and yaw rates and  $\phi$  is the roll angle. The aileron control input is denoted by  $\delta_a$ , and the rudder control input  $\delta_r$ . The Lateral characteristic equation is:

$$\lambda^4 + 60.4193\lambda^3 + 955.7446\lambda^2 + 15968.969\lambda - 43.3071 = 0 \quad (4.5)$$

The roll mode pole is at ( $\lambda_2=-47.3587$ ), this corresponds to a very fast, first order exponential response with a time constant of 0.0211s. While the spiral mode which is extremely slow its pole is at ( $\lambda_1=0.0027$ ). It is a first order exponential re-



Table 4.2: Pole locations, natural frequencies and periods for the lateral modes.

	Eigenvalue (Pole)	$\omega_n$ (rad/s)	Period(s)
Mode 1(Spiral/slow mode)	$\lambda_1=0.0027$	0.0027	2327.1
Mode 2(Roll/fast mode)	$\lambda_2=-47.3587$	47.3587	0.1327
Mode 3(Dutch Roll/oscillatory mode)	$\lambda_3=-6.5317 \pm 17.1635i$	18.3643	0.3421

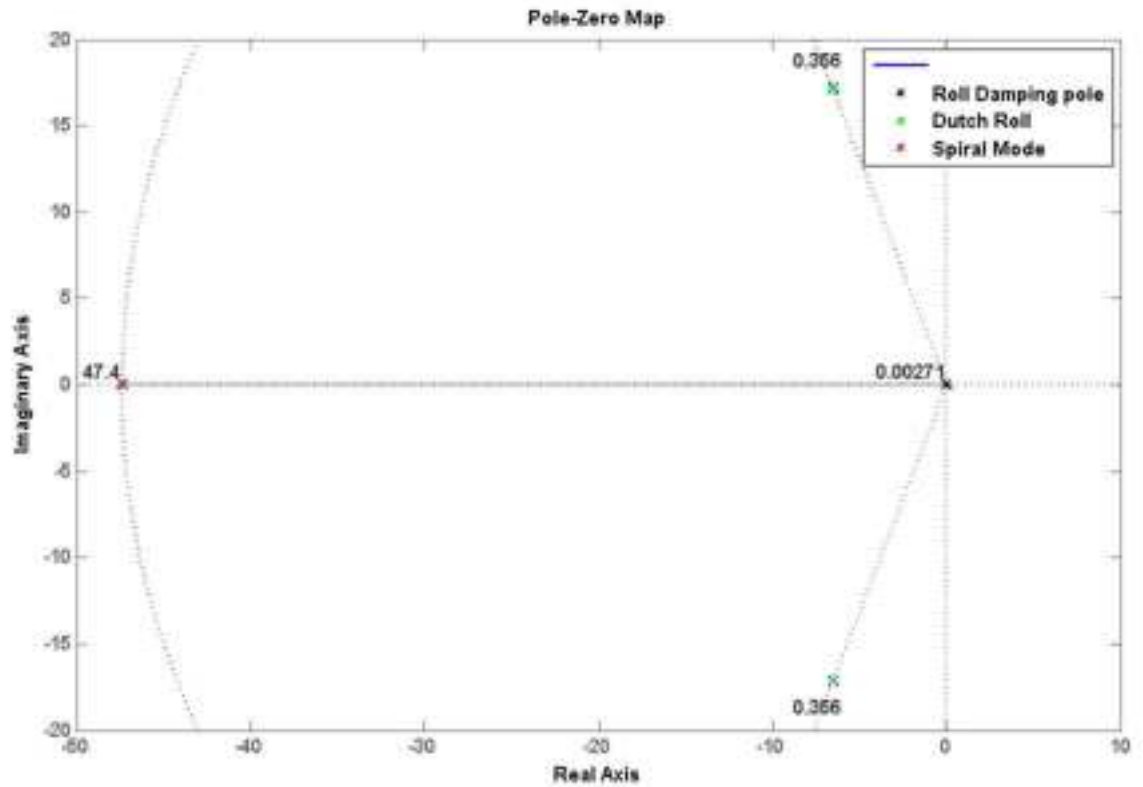


Figure 4.3: Poles Locations for the Lateral Model

sponse with a time constant of 2327.1s. The dutch roll mode poles are at  $\lambda_3=-6.5317 \pm 17.1635i$  with  $\zeta = 0.356$ . These poles for a stable, lightly damped oscillatory mode. The period of oscillation is 0.3421.

In this section, the longitudinal and lateral UAV modes specific for the ARF60 aircraft used in this project were presented. The modes of motion were analyzed. The gained information in this section is used in the next section for the autopilot design. Finally, the dynamics of motion analyzed in this section are consistent with those of conventional aircraft, which instills confidence that there are no dramatic errors in the aircraft models.

## 4.2 ARF60 UAV AUTOPILOT DESIGN USING SUCCESSIVE LOOP CLOSURE (SLC)

In this section, autopilot design steps are outlined. Furthermore, an overview of the controller is given in Section 4.2.1. Finally, a detailed description of longitudinal and lateral autopilots is explained in sections 4.2.2 and 4.2.3.

### 4.2.1 Autopilot Overview

The controller is designed so that the Aircraft is stable and performing the given specification. One simple approach to achieve this is to use open loop control. In such control, the aircraft poles are merely cancelled by compensator zeros and the compensator poles are used to define the desired aircraft dynamics. The problem with this approach is that if the aircrafts dynamic model changes or the aircraft experiences disturbances, the control system performance will deteriorate rapidly. Therefore, feedback control is used to overcome open loop control problems. Feedback control not only reduces the system sensitivity to modelling uncertainties, but also eliminates disturbance and noise effects. Some Examples of disturbance types that affect aircraft motion include wind disturbance, fuel level changes, changes in aircraft model due to flight conditions and aeroelastic effects. The controller robustness is determined by its ability to reduce system sensitivity to modelling errors.

The main task in controlling an aircraft is the control of the attitude since it provides control over aircraft accelerations. For example, the bank angle of an aircraft determines its centripetal acceleration. Direct control over the aircrafts acceleration is desired because the stabilization effects integrate down into the velocity and position states over time and thus leave only the reference velocity and position commands to be regulated by outer control loops.

The aircraft controller involves three main controllers which are the stability augmentation system (SAS) controller, the attitude stabilization (Autopilot) controller and the trajectory tracking controller (Bernard Etkin, 1996).

The stability augmentation system provides artificial damping in order to suppress any high frequency aircraft dynamic. Furthermore, the attitude stabilizer regulates aircraft pitch and roll angles to control aircraft acceleration. Finally, the trajectory tracker controls heading and altitude as an outer loop.

These control loops provide commands to the attitude controller and thus deal with the kinematics of the aircraft. The advantage of this successive loop closure design methodology is that once the attitude controllers have been implemented, the trajectory controllers can be implemented in cascade because the outer control algorithms are essentially independent of the inner ones.

Each of the three controller types is now discussed in more detail.

#### Stability Augmentation System (SAS) Controller

As stated previously, stability augmentation controller is responsible for suppressing any high frequency aircraft dynamic by providing artificial damping.

An aircraft experiences high frequency during the short period mode, the dutch roll mode and during the roll mode. The natural damping of such modes can be caused by induced angles of incidence during angular rate disturbance which implies that the damping is dependent on aircraft velocity and location of center of gravity. To alter natural damping effect, an artificial damping is imposed by sensing aircraft angular rates with gyroscopes. Then, the signals from gyroscopes are fed to their designated actuators to augment aircraft natural damping.

In this thesis, both short period and dutch roll dampers are designed and implemented. However, the artificial roll damper isn't implemented since roll mode is deeply damped with high frequency. The outer attitude control loops will reject the wind gust disturbance.

#### Attitude Stabilization (Autopilot) Controller

Attitude stabilization controller regulates the aircraft pitch and roll angles and in turn controls aircraft acceleration. One approach of implementing such a controller is to use a Linear Quadratic Regulator (LQR) (Peddle, 2005). However, using such approach isn't practical since neither the aircraft model nor low cost sensors provide high accurate data estimation and measurements. Typical examples of low cost sensors include rate gyroscopes, infrared sensors and vision based systems. Although rate gyroscopes work well in all environmental conditions, they have biases on the order of a few tenths of a degree per second. Due to these poor biases, rate gyroscopes cannot be used alone to provide aircraft attitude measurements. Therefore,

rate gyroscopes are combined with a low cost set of accelerometers. In this case, accelerometers provide acceptable attitude information on stationary platforms with low frequency while rate gyroscopes provide good angular rate measurements at high frequency. In other words, rate gyroscopes and accelerometers are used in a complementary filter where the rate gyroscopes give attitude information at high frequency while accelerometers provide attitude information at low frequency. Although combining rate gyros with accelerometers provide reasonable attitude information, it has some drawbacks. During steady manoeuvres, it experiences adverse properties such as constant turns or loops.

The solution to this problem is to use an estimator that takes measurements from low cost rate gyroscopes, accelerometers and a variety of other sensors such as a GPS receiver and a magnetometer. In such estimators, all aircraft states are accurately estimated. however, it is computationally expensive and it is affected by instruments failure. From the above discussion, it is obvious that determining aircraft attitude based on sensors alone isn't an easy task. However, if we can find the states that are directly related to the aircraft attitude under common flight conditions and then measure them using low cost sensors, the aircraft attitude can be indirectly controlled. The designed controller is simple, requires low cost sensors and a small computational power. Both the pitch and roll angle controllers are discussed below.

- Pitch Attitude Hold Consider the primary longitudinal state space model and the climb rate equations described in Equation 4.6 and Equation 4.7, respectively:

$$\dot{x} = Ax + Bu \quad (4.6)$$

$$\dot{h} = C_h x \quad (4.7)$$

Both equations represent a set of five first order, linear differential equations with 7 variables:  $u$ ,  $w$ ,  $q$ ,  $\theta$ ,  $h$ ,  $\delta_e$  and  $\delta_t$ . To have a unique solution of the system, two more linearly independent equation are required. These equations will be the control law equations that determine how the control variables are calculated from different states. The change in airspeed is measured using a differential pressure sensor while the climb rate is measured using an absolute

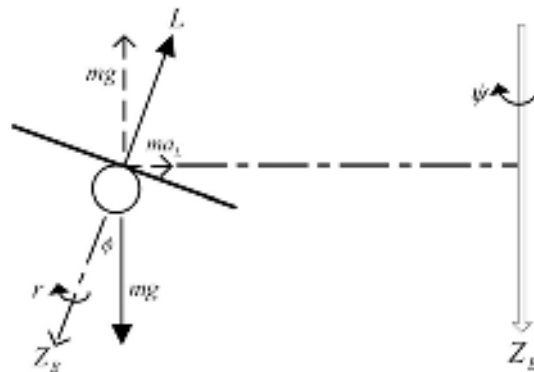


Figure 4.4: Aircraft in a Steady Banked Turn

pressure sensor. Once the two states are measured, they can be used to generate the control signals and thus stabilizing the pitch angle without the need for a direct measurement.

- Roll Attitude Hold Based on the diagram, illustrated in Figure 4.4, the demonstrated aircraft has a steady, constant altitude, banked turn.

The lift vector counters the weight of the aircraft and provides the necessary centripetal acceleration for the turn. Therefore, the lateral acceleration can be written as:

$$a_L = U_o \dot{\psi} = g \tan \phi \quad (4.8)$$

If the roll and pitch angles are limited to small angles; equation 4.8 turns to:

$$\phi \approx \frac{U_o}{g} r \quad (4.9)$$

Equation indicates that for small pitch and roll angles, the aircrafts yaw rate is proportional to the roll angle. As a result, the roll angle can be controlled by controlling the aircraft yaw rate. Controlling the yaw rate not only avoids integrating the signal from rate gyroscopes, but also avoids roll angle drift. However, with a yaw rate controller, the bias will merely cause the aircraft to enter into a slow turn that opposes its magnitude. This turn can easily be corrected by an outer trajectory control loop.

### Trajectory Tracking Controller

The trajectory tracking controllers are responsible for regulating the states of altitude  $h$ , heading  $\psi$  and cross track error  $y$ .

These controllers are chosen because, together with the airspeed, climb rate and yaw rate regulation capabilities of the attitude controllers, they make it possible for the autopilot to perform all conventional flight tasks. The altitude is easily controlled by taking height measurement and feeding them to the climb rate controller. The feedback is used to stabilize the extra integrator pole that the height state adds to the system. The altitude measurement are obtained using an absolute pressure sensor. Then, the heading and cross track error (guidance) controllers are implemented by successive loop closure. A heading measurement can be fed to the yaw rate controller to stabilize the extra integrator added to the system by the heading state. The guidance controller can then be implemented by feeding a cross track error measurement to the heading controller, to stabilize the single integrator added to the system by the cross track error state. This successive loop closure technique minimizes the amount of dynamic compensation required in implementing the two lateral trajectory controllers. The heading and cross track error states can both be measured using a low cost GPS receiver.

### Summary of the Controllers

The stability augmentation systems, attitude stabilization and trajectory tracker controllers discussed in the previous three sections, are divided into a longitudinal and lateral set and summarized below.

- Longitudinal
  1. Pitch Rate Damping.
  2. Pitch attitude hold using elevator.
  3. Airspeed hold using throttle.
  4. Altitude hold using commanded pitch.
- Lateral
  1. Roll Rate Damping.

2. Roll Attitude Hold.
3. Yaw Rate Damping.

The entire control system can be implemented using the following low cost sensors,

- MIDG II Sensor: an Inertial Navigation System (INS) with Global Positioning System (GPS) B.1.2.
- Differential Pressure Sensor B.1.4.
- Absolute Pressure Sensor B.1.3.

The following two sections provide the detailed design of the longitudinal and lateral controllers as applied to the aircraft used in this project. All of the controllers are designed in the continuous time domain. Then the controllers are converted to the discrete domain using Tustin digitization method at a sample rate of 100Hz. This rate was chosen as a convenient rate for implementation, well above the frequencies of the aircrafts natural modes of motion. The discretization of these controllers is not shown in this chapter. Successive loop closure was used for the autopilot design. The basic idea that one loop is closed at a time. At each stage of the design, there is only one gain to tune. Therefore, root locus techniques were used to design our autopilot using successive loop closure (Randal W. Beard, 2007). Designing an autopilot using these techniques requires linear models of the UAV dynamics for a number of trimmed flight conditions. MATLAB was used to determine the trim conditions and derive linear state-space models directly from the nonlinear UAV Simulink model. This saved time and helped to validate the model. The functions provided by Simulink Control Design allowed to visualize the behavior of the AUS ARF60 UAV in terms of open-loop frequency and time responses. Figure 4.5 shows how the Lateral Autopilot inner loops gains were tuned and validated using those tools.

#### 4.2.2 Longitudinal Autopilot

The design and simulation of the aircrafts longitudinal controllers is considered in this section. Each controller design begins with a discussion of the design approach before the details of the controller are considered and the results verified by linear and nonlinear simulation.

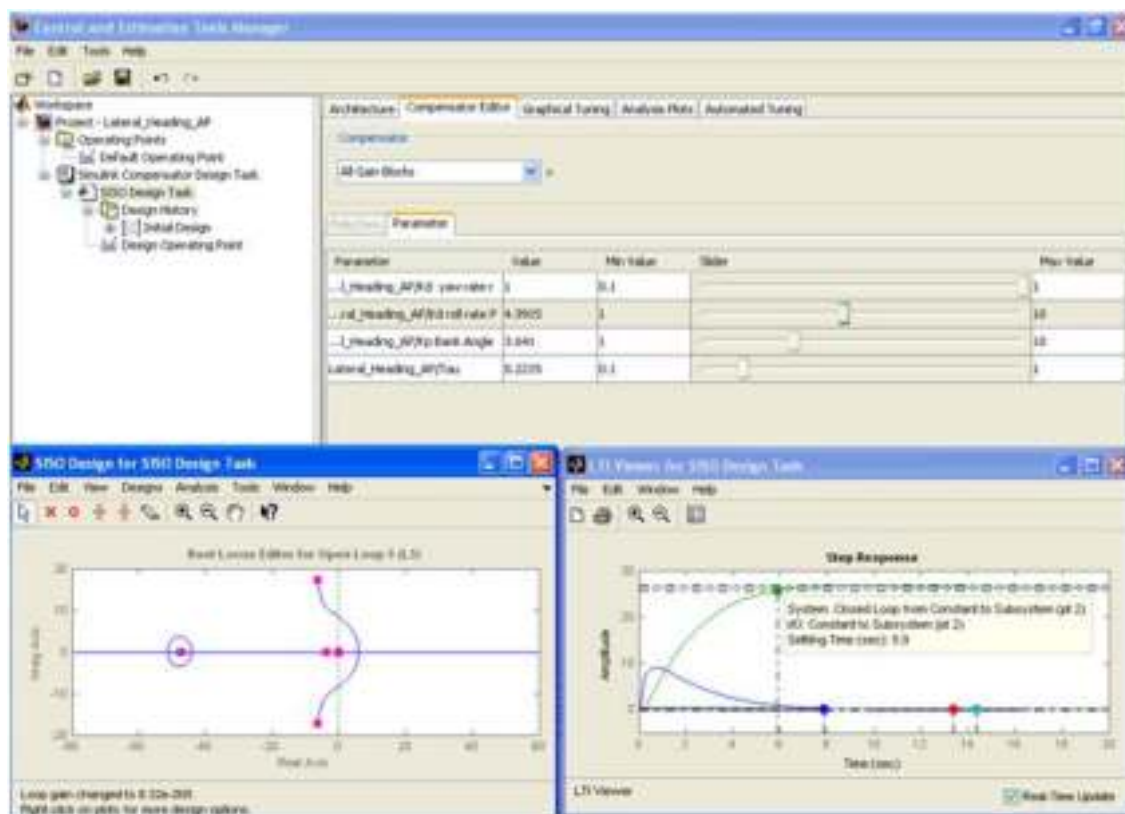


Figure 4.5: SISO Design Task, Root Locus Graphical Tuning Window, Analysis Plots and Compensator Parameters Tuning Editor.

### Pitch Rate Damping

The natural damping of the short period mode predominantly arises from pitch rate induced angles of incidence on the tailplane during pitch rate perturbations. Thus, the damping is a function of the airspeed and the tailplane moment arm length (IT). The aircraft's airspeed changes regularly during flight and the tailplane moment arm length is a function of the center of gravity location, which varies with fuel consumption. Artificial pitch rate damping is thus desired to desensitize the overall aircraft pitch rate damping to variations in these flight parameters, as well as to provide damping with respect to inertial space for wind gust disturbance rejection. Modal analysis was done before and showed that the short period mode is orders of magnitude better controlled by the elevator than by the throttle. This suggests that simple feedback of the aircraft's pitch rate to the elevator will create an effective pitch rate damper. This feedback will essentially provide the aircraft with a larger tailplane during pitch rate perturbations. The control system is summarized in the block diagram of Figure 4.6 where the dynamic equations are obtained from Equation



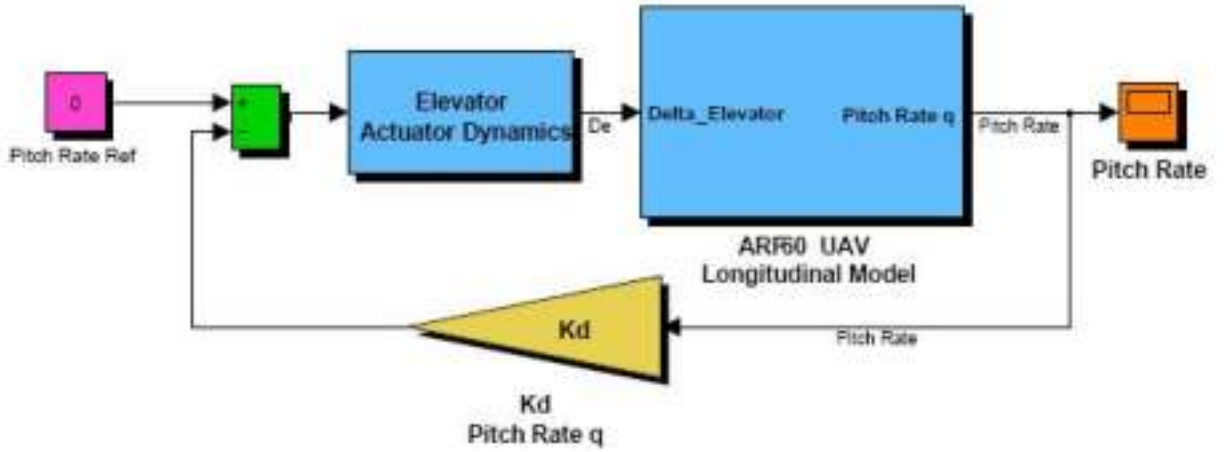


Figure 4.6: Pitch Rate Damping Block Diagram

4.1. The transfer function that relates the elevator deflection in rad  $\delta_e$  to the pitch rate state in radians per second (rad/s) $q$  is written in Equation 4.10 which will be augmented with the elevator actuator dynamics that was identified in 3.6 and written in transfer function form in Equation 4.12.

$$\frac{\delta_e}{q} = \frac{-147.6913s(s + 9.404)(s + 0.3084)}{(s^2 + 0.2303s + 0.5461)(s^2 + 36.22s + 405.6)} \quad (4.10)$$

$$\frac{\delta_{e_a}}{\delta_{e_c}} = \frac{1}{(0.10505s + 1)} \quad (4.11)$$

The root locus plot for variation of the feedback gain from pitch rate to elevator command (Actuator dynamics is augmented) is shown in Figure 4.7. The two poles with large movement are the short period mode poles while the phugoid mode poles are barely visible near the origin.

A feedback gain of,

$$k_q = -0.11642 \quad (4.12)$$

increases the short period mode damping, which is deemed sufficient to adequately desensitise the pitch damping loop without exciting unmodeled dynamics. Of course, this feedback gain can easily be fine tuned during practical flight tests as desired.

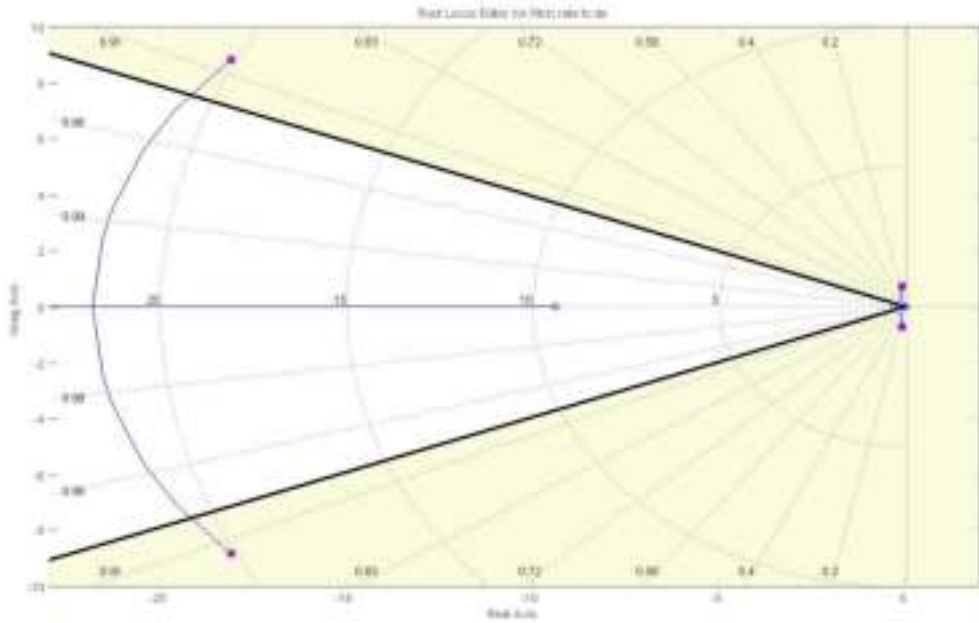


Figure 4.7: Pitch Rate Damping Root Locus

#### Pitch attitude hold using elevator

The aircraft's pitch attitude is regulated by the control of altitude using the elevator actuator. Since the Phugoid oscillation cannot occur if the pitch angle  $\theta$  is not allowed to change (except when commanded), a pitch-attitude-hold feature in the autopilot would be expected to suppress the Phugoid. To proceed further we therefore use the exact transfer function derived from the full system of linearized longitudinal equations of motion (see Equation 4.13). The control system is summarized in the block diagram of Figure 4.8, it includes an inner loop for SAS and an outer loop for the pitch attitude. PI controller was used in the outer loop to stabilize the UAV attitude. The set of the gains are summarized in Table 4.3 and the corresponding step response for those set of gains is shown in Figure 4.9. The specifications for pitch  $1deg$  step response are,

- Rise time of under  $2s$
- Overshoot of less than  $8\%$
- Zero steady state error

$$\frac{\delta_e}{\theta} = \frac{-147.6913(s + 9.404)(s + 0.3084)}{(s^2 + 0.2303s + 0.5461)(s^2 + 36.22s + 405.6)} \quad (4.13)$$

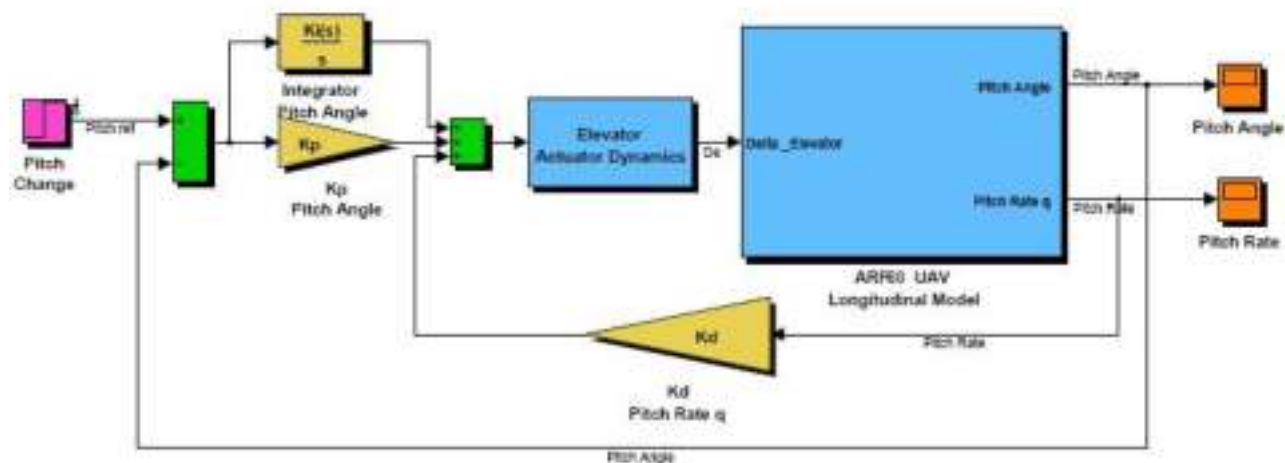


Figure 4.8: Pitch attitude hold using elevator Block Diagram

Table 4.3: Pitch attitude hold using elevator loop gains

Tuned Parameter	gain value
Pitch attitude PID loop ( $K_p$ )	-1.1197
Pitch attitude PID loop ( $K_i$ )	-0.57

Altitude hold using commanded pitch

The altitude controller is the only longitudinal trajectory controller. An outer loop which is the Altitude hold controller was added to the Pitch attitude hold using elevator to maintain level flight. Before the height error signal is fed to the Pitch attitude hold controller, it must be sent through a saturation block to ensure that it does not command climb rate signals in excess of  $\pm 2m/s$ . This block automatically ensures that the aircraft enters a constant climb rate mode when large altitude step commands are issued. The transfer function of the system is shown in Equation 4.14. The controller block diagram is shown in Figure 4.10 and its set of gains are shown in Table 4.4 and the step response of the designed system is shown in Figure 4.11. The specifications for altitude  $1m$  step response are,

- Rise time of under  $9s$
- Overshoot of less than  $16\%$

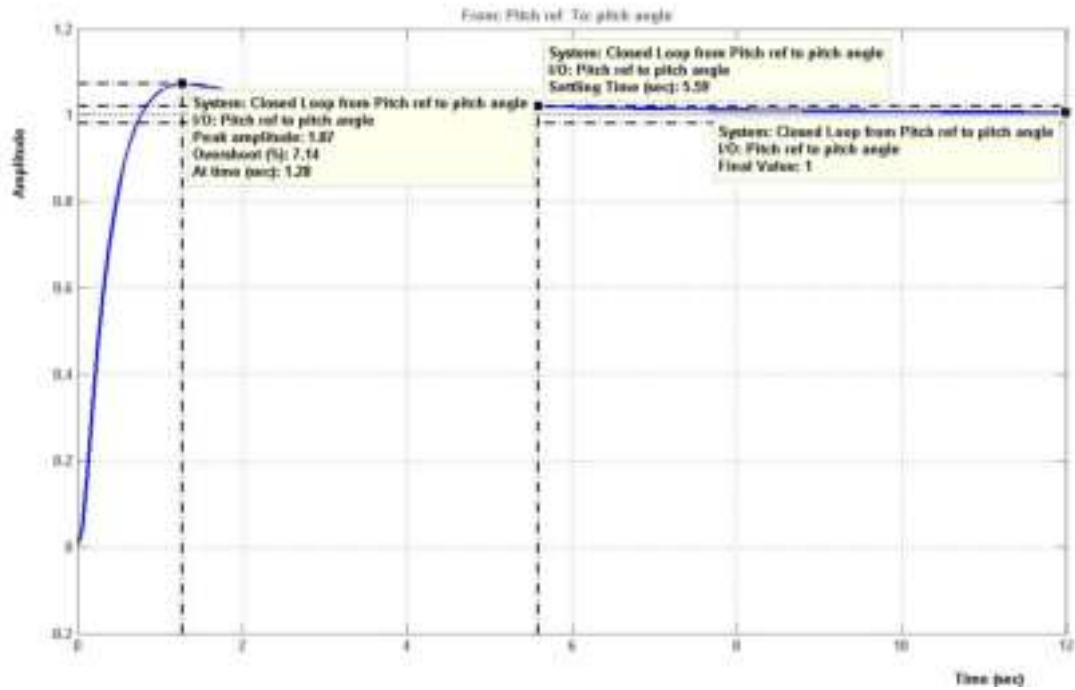


Figure 4.9: Pitch attitude hold using elevator step response

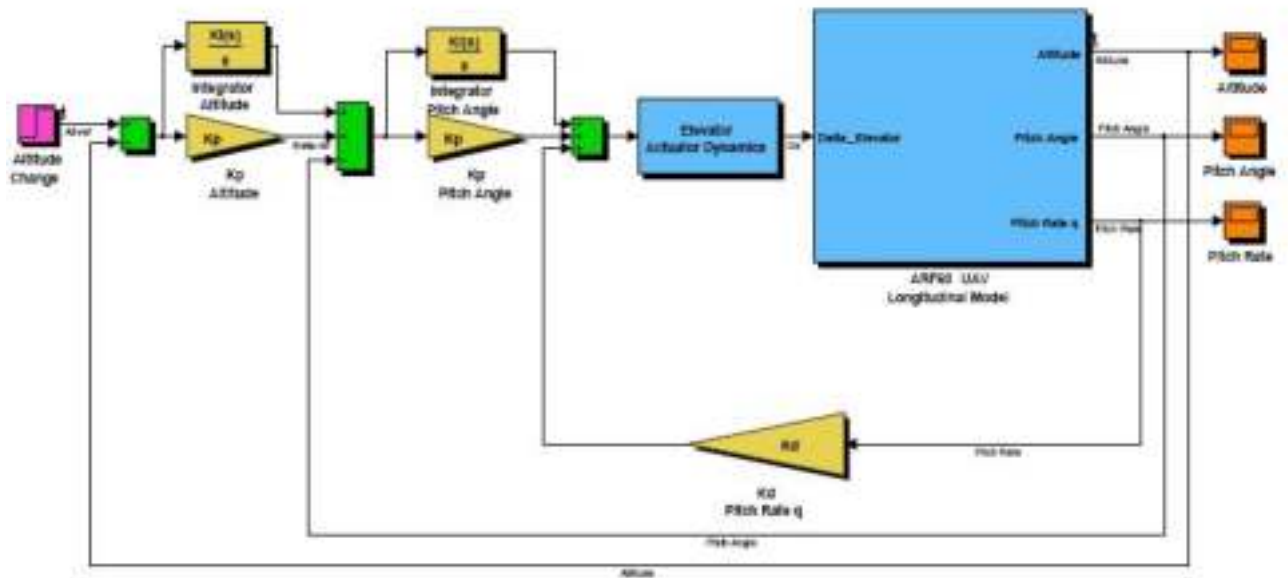


Figure 4.10: Altitude hold using commanded pitch Block Diagram

- Zero steady state error

$$\frac{\delta_e}{h} = \frac{14.0043(s + 59.63)(s - 33.53)(s + 0.2043)}{s(s^2 + 0.2303s + 0.5461)(s^2 + 36.22s + 405.6)} \quad (4.14)$$

Table 4.4: Altitude hold using commanded pitch loop gains

Tuned Parameter	gain value
Altitude hold PID loop ( $K_p$ )	0.4744
Altitude hold PID loop ( $K_i$ )	0.02224

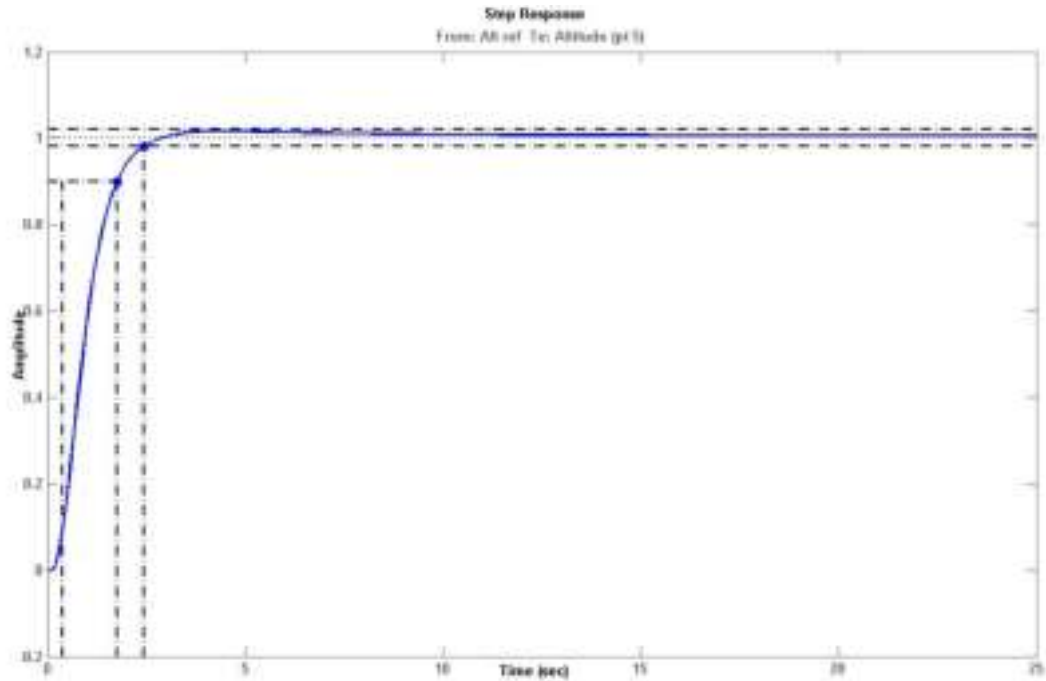


Figure 4.11: Altitude hold using commanded pitch loop step response

#### Airspeed hold using throttle

Figure 4.12 is the block diagram of the control loop for the forward airspeed ( $u$ ) to maintain a constant speed along the flight path. the difference in flight speed is used to produce proportional displacement of the engine throttle so that the speed difference is reduced. The PI controller gains are listed in table 4.5. The step response is shown in Figure 4.13. The specifications for airspeed  $1m/s$  step response are,

- Rise time of under  $2s$
- Overshoot of less than 1%
- Zero steady state error

$$\frac{\delta_t}{u} = \frac{51.5s(s^2 + 36.22s + 405.5)}{(s^2 + 0.2303s + 0.5461)(s^2 + 36.22s + 405.6)} \quad (4.15)$$

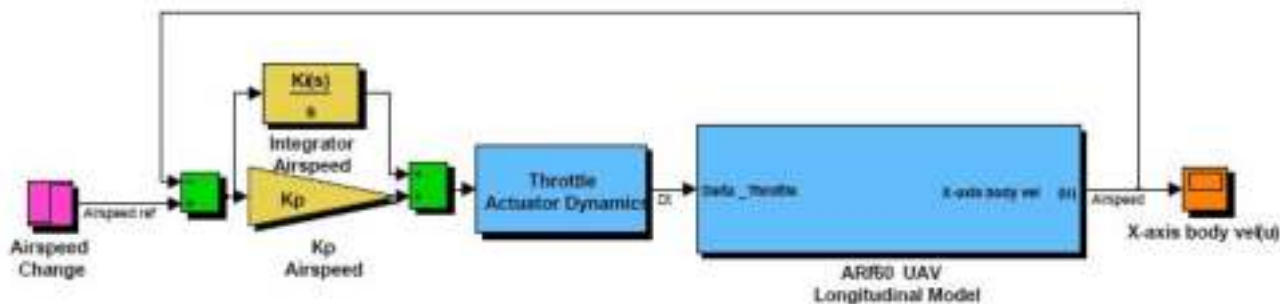


Figure 4.12: Airspeed hold using throttle Block Diagram

Table 4.5: Airspeed hold using throttle loop gains

Tuned Parameter	gain value
Airspeed hold PID loop ( $K_p$ )	0.02487
Airspeed hold PID loop ( $K_i$ )	0.004564

### 4.2.3 Lateral Autopilot

The design and simulation of the aircrafts lateral controllers is considered in this section. Each controller design begins with a discussion of the design approach before the details of the controller are considered and the results verified by linear simulation.

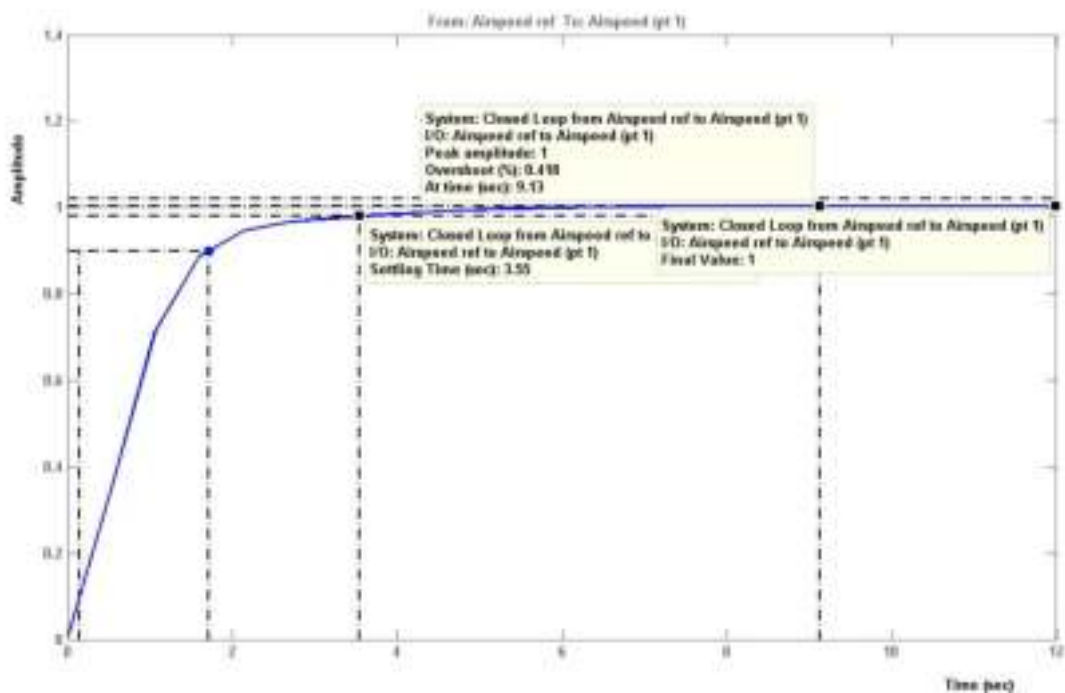


Figure 4.13: Airspeed hold using throttle step response

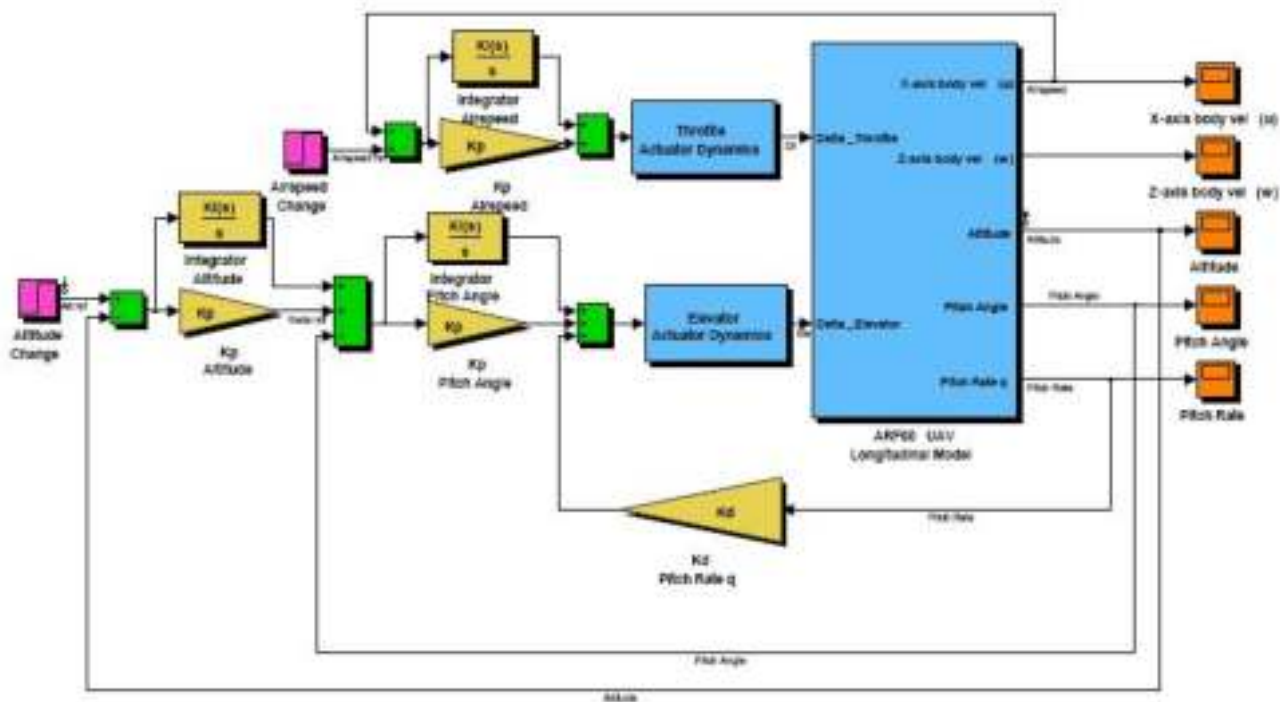


Figure 4.14: ARF60 Longitudinal Autopilot Block Diagram

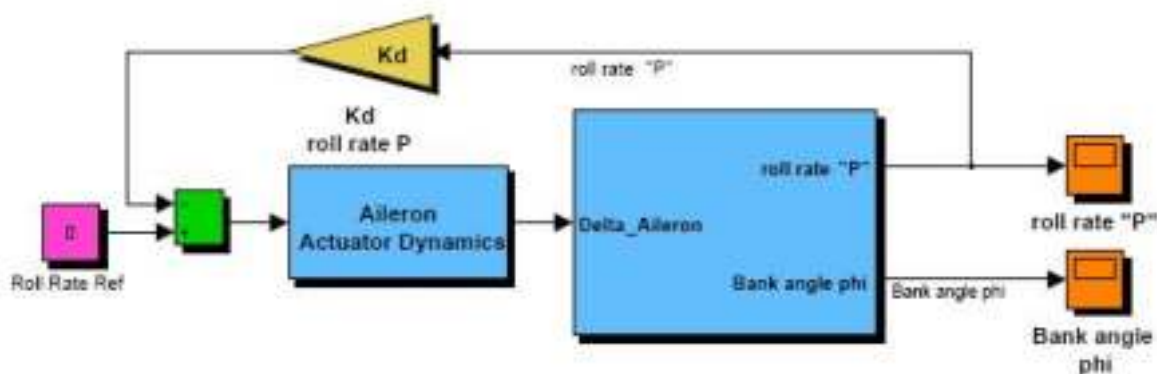


Figure 4.15: Roll Rate Damping Block Diagram

### Roll Rate Damping

Closed loop control of roll rate (Figure 4.15) is used to reduce the variation of roll performance with flight conditions.

### Roll Attitude Hold

Feedback of the deviation of the roll angle to the ailerons (Figure 4.16) is used to control the aircraft's roll angle thus the autopilot will hold the wings level.

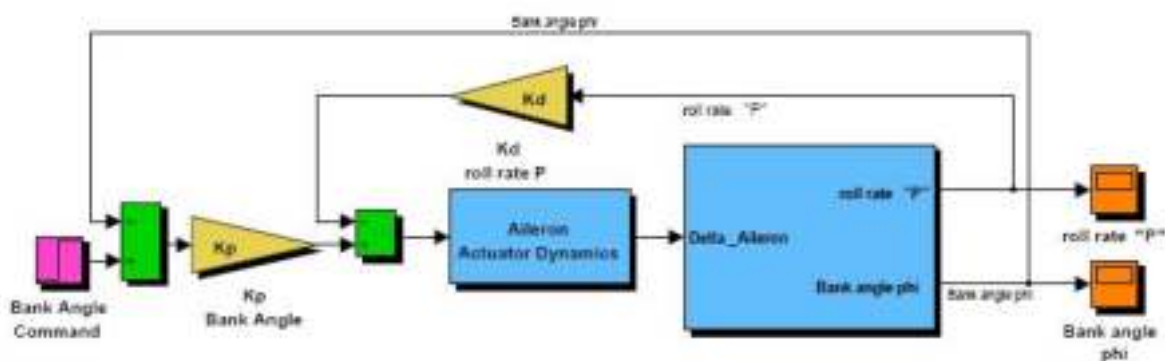


Figure 4.16: Roll Attitude Hold Block Diagram

### Dutch Roll Damper

Modal analysis showed that the natural damping of the dutch roll mode is low. Thus a dutch roll damper is implemented in order to suppress the natural dynamics of the dutch roll mode, desensitize the overall yaw damping to variation in flight parameters and provide damping with respect to inertial space for wind gust disturbance. Continuing along the same lines as the design of the pitch rate damper, the dutch roll damper is implemented by feeding a yaw rate signal back to the rudder. The rudder is used to provide the damping because it was shown by modal analysis to be 4 times more effective at controlling the dutch roll mode than the ailerons are. The yaw rate signal must however, be high pass filtered before it is fed to the rudder so that the damper does not counter constant turn rate motions. A secondary advantage of the high pass filter is that it negates the bias effects of low cost rate gyroscopes.

The control system is summarized in the block diagram of Figure 4.17 where the plant dynamics are taken from Equation 4.4 and shown in transfer function form in Equation 4.16. The output matrix ( $C$ ) is set to extract the yaw rate state in degrees per second ( $\text{deg/s}$ ). Note that the yaw rate signal moves through a washout filter before being fed back to the rudder in a proportional fashion. Choosing the washout filter cutoff frequency is an iterative process. However, it must be chosen low enough to ensure the frequency of the dutch roll mode lies within its passband (without too much phase error), but high enough so as not to interfere with constant turn rate motions. With the natural frequency of the dutch roll mode at  $18\text{rad/s}$ , a washout filter cutoff frequency of  $10\text{rad/s}$  is found to work well.



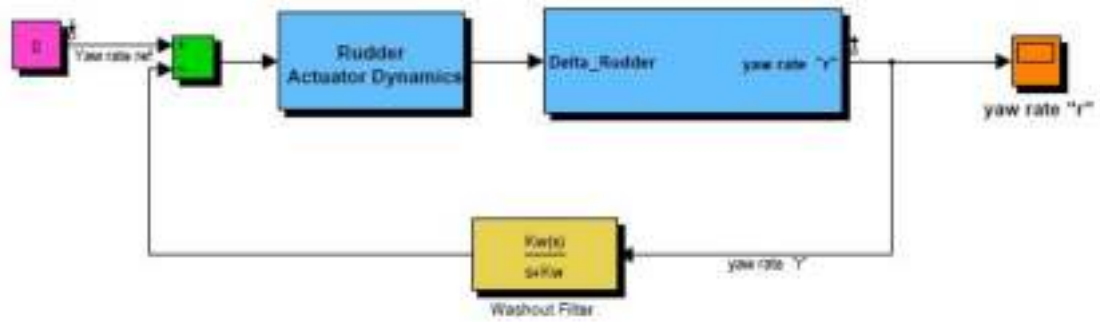


Figure 4.17: Dutch Roll Damper Block Diagram

Table 4.6: Dutch Roll Damper loop gains

Tuned Parameter	gain value
Dutch Roll Damper PID loop ( $K_{dr}$ )	0.1
Dutch Roll Damper Washout Filter ( $K_W$ )	0.2
Dutch Roll Damper Washout Filter ( $\omega_W$ )	10

$$\frac{\delta_r}{p} = \frac{5.0475s(s^2 - 0.8548s + 258)}{(s + 47.36)(s - 0.002712)(s^2 + 13.06s + 337.2)} \quad (4.16)$$

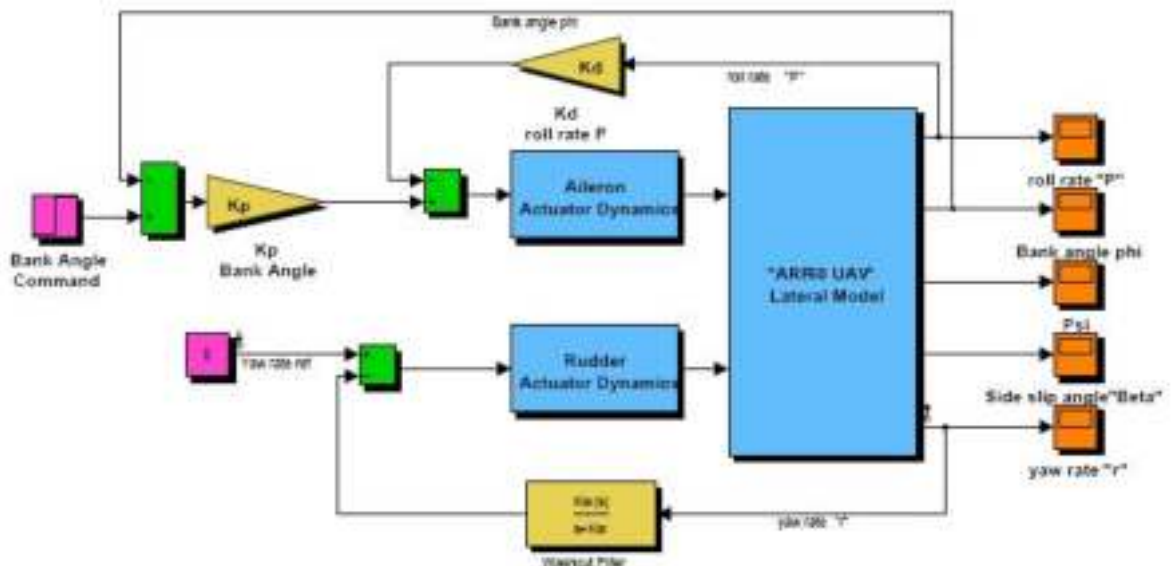


Figure 4.18: ARF60 Lateral Autopilot Block Diagram

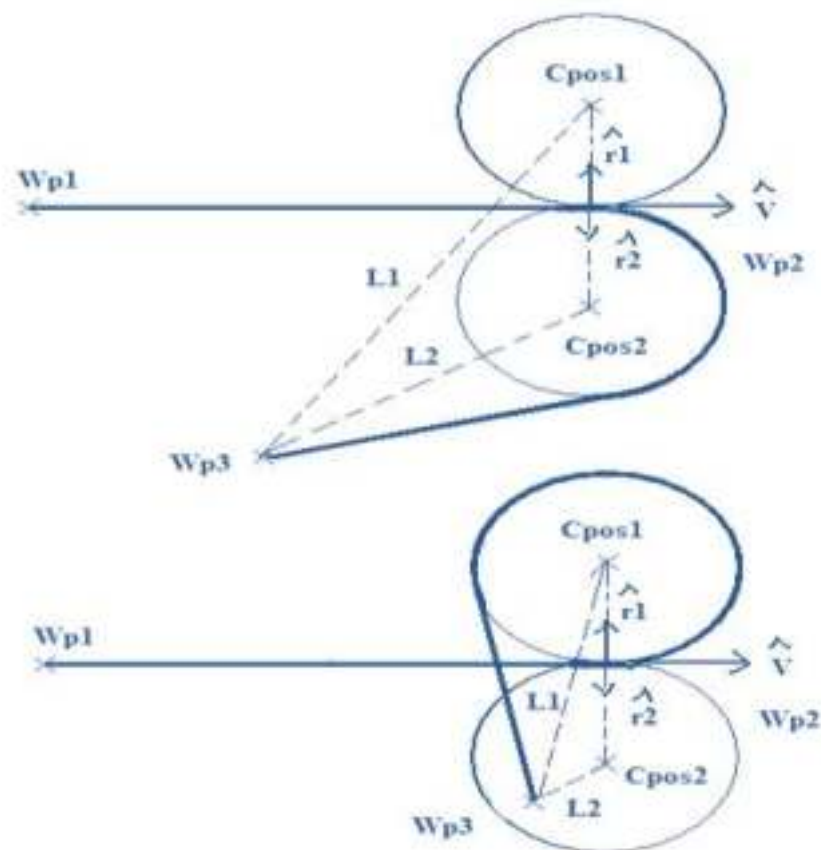


Figure 4.19: Path taken by the UAV When Entering a Curve using Feedback Guidance

#### 4.2.4 Trajectory Tracker(Shortest Flight Algorithm in 3D)

In this thesis, the natural extension of feedback guidance strategy using band-bang control strategy (Bhatt S. P., 2005) was used, simulated and implemented. The algorithm contains straight lines and circular curves in each leg of the UAV mission. Using this strategy, once the aircraft reaches a waypoint, it will start to turn until it reaches the next waypoint and then fly straight to the next waypoint. However, there are two circles where the aircraft can take; one circle is in the clockwise direction while the other one is in the counterclockwise direction. The distance from the center of the circular arc to the next waypoint determines which of the circles the aircraft chooses. If the distance between the center of the circular arc and the next waypoint is smaller than  $R$  (the minimum radius of the circular arc limited by the maximum turning rate of the aircraft), the UAV will choose the circular arc whose center is farther from the waypoint and vice versa. Figure 4.19(Hassan, 2006) represents the two circles that the aircraft can maneuver from one way point to another. The heading of the aircraft from its current position to the next waypoint is iteratively computed using Equation

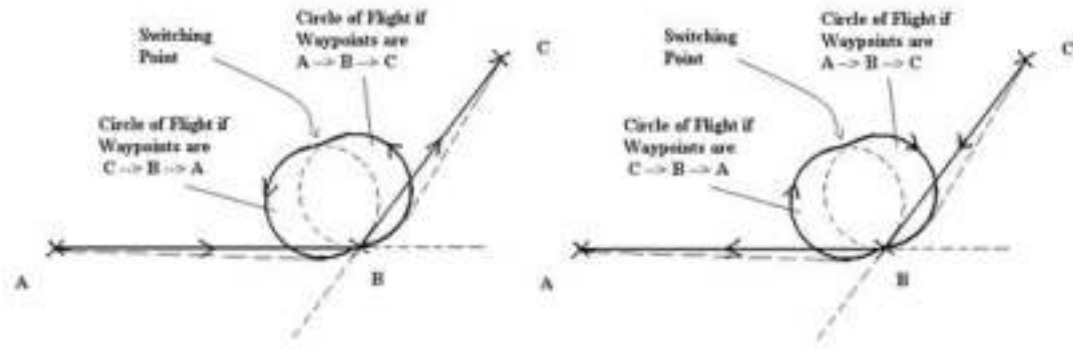


Figure 4.20: Extension of the Feedback Guidance Strategy - Bidirectional

4.17. Then, the calculated heading is compared with the aircraft current heading. If the heading error is within 10 degrees of the UAV current heading, the UAV will bank in such a way that is proportional to the heading error, thus, reducing the error before following a straight line to the next waypoint. Furthermore, the UAV will fly a circular curve until it faces the next waypoint. Then, it will fly straight to the waypoint if the next waypoint is more than 10 degrees of the UAV current heading. Finally, if the heading error remains more than 10 degrees, the UAV will continue in a circular path; otherwise, it will straighten.

$$H_p = \arctan\left(\frac{Y_N - Y_C}{X_N - X_C}\right) \quad (4.17)$$

Where  $X_N, Y_N$  are the coordinates of the next waypoint and  $X_C, Y_C$  are the instantaneous current coordinates. More Details descriptions of the feedback guidance strategy using band-bang control strategy can be found in (Bhatt S. P., 2005).

Although feedback guidance strategy will allow the aircraft to reach its destination, it doesn't control the heading of the aircraft once it reaches its waypoint. Therefore, feedback guidance strategy was extended to bidirectional Feedback Guidance Strategy by (Hassan, 2006). Figure 4.20 shows the bidirectional Feedback Guidance Strategy.

As indicated earlier, feedback Guidance Strategy is used to form a circle in which the aircraft enters when travelling from points A to B to C. However, in bidirectional Feedback Guidance Strategy, two circles are drawn; one is when the aircraft travels from points A to B to C while the other one is when the aircraft travels from points C to B to A. The switching point between the two circles is determined by the point when the current direction of the aircraft is exactly 180 degrees (opposite) from

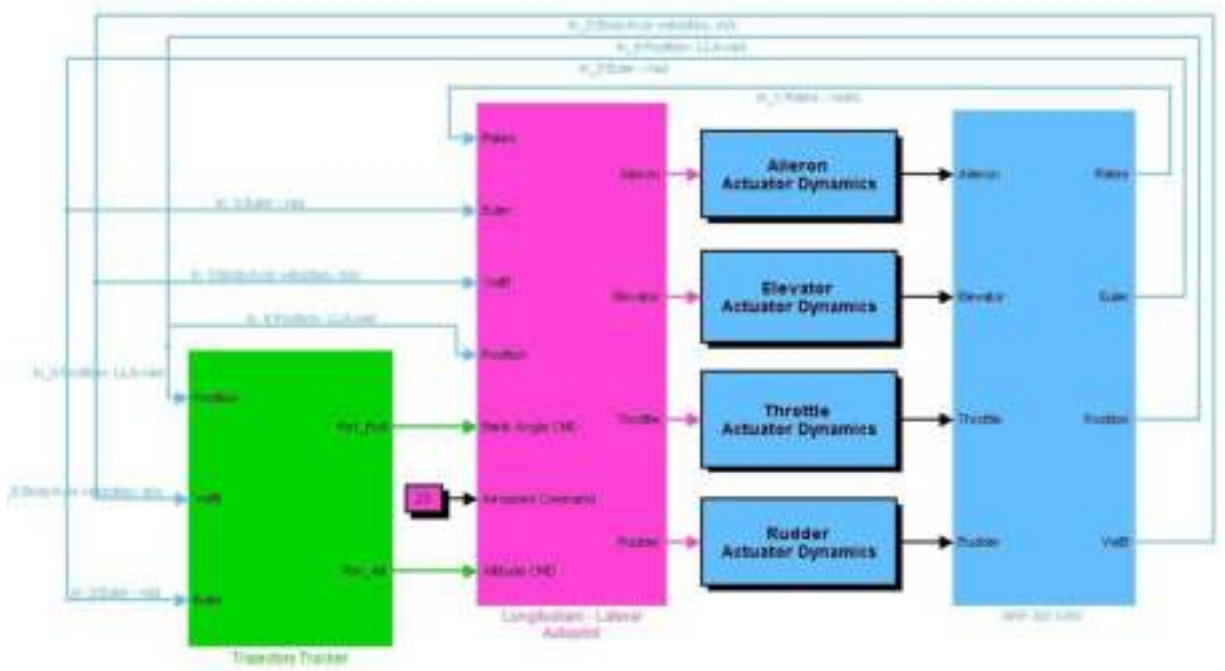


Figure 4.21: ARF60 Autopilot and Trajectory Tracker System Block Diagram

the theoretical current direction of the aircraft. At the switching point, the aircraft will change its maneuvering from following the first circle to straight flight until it intersects the other circle to follow the circular path again. The conditions where the second switch occurs are summarized in Equations 4.18.

$$if 0^\circ \leq \theta_A < 180^\circ \text{ and } \theta_V = \theta_A + 180^\circ \quad (4.18a)$$

$$elseif \theta_A = 180^\circ \text{ and } \theta_V = 0^\circ \quad (4.18b)$$

$$elseif 180^\circ \leq \theta_A < 360^\circ \text{ and } \theta_V = \theta_A - 180^\circ \quad (4.18c)$$

### Trajectory Tracker Results (Simulation)

Figures 4.22-4.24 show the plots of waypoint navigation using the extension of the Feedback Guidance Strategy - Bidirectional "simulation only" methods described earlier. The results show that the aircraft reaches the desired waypoint "dead on target". The reader must be given to understand that this is only a simulation result where continuous updates of all the states necessary were available such as position, heading, altitude, and all the other states necessary for the autopilots. These parameters were available continuously, and were very precise, and they did not suffer

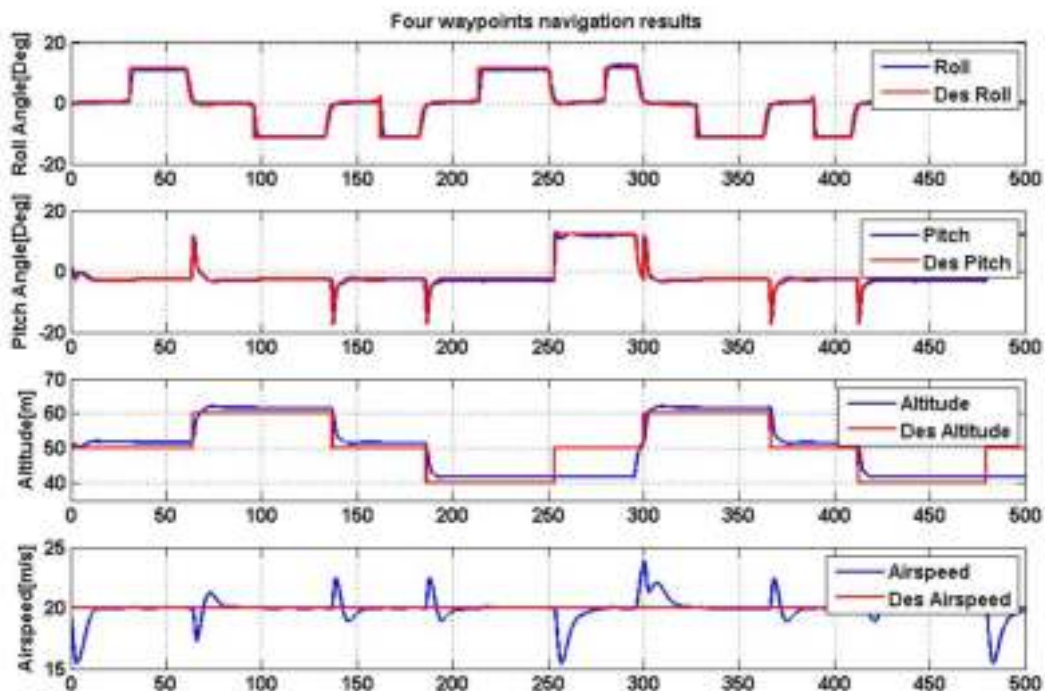


Figure 4.22: Four waypoints navigation results

from noise associated with sensing devices. Thus the results achieved can be described as ideal. The Bang-Bang Trajectory Tracker with the SLC Autopilot completed the mission with less than 500 seconds. Overall the SLC Autopilot performed as expected and allowed the plane to bank more for a given bank reference command, and thus take sharper and shorter turns.



Figure 4.23: Four waypoints navigation Map 2D

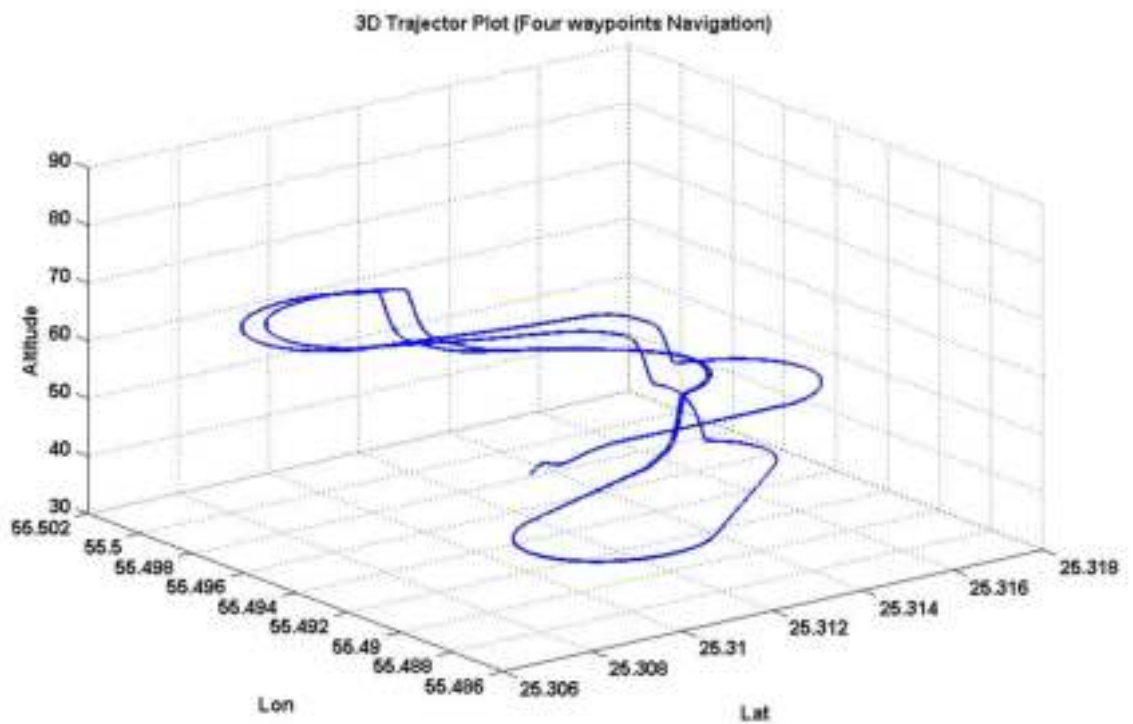


Figure 4.24: Four waypoints navigation plot 3D

## CHAPTER 5

# CONTROL AND HARDWARE IMPLEMENTATION

This chapter discusses the hardware and software involved in the avionics and ground station. A block diagram overview of the system is shown in Figure 5.1.

The block diagram shows that the system is divided into two logical parts: the UAV and the ground station. The UAV consists of a RC (Radio Controlled) receiver, a set of servos and an avionics package developed. The ground station consists of a laptop computer running the ground station software, an RF transceiver module and an RC transmitter. The avionics package and ground station designs are discussed in more detail. A summary of the system including a cost, power consumption and weight analysis is presented in the final section.

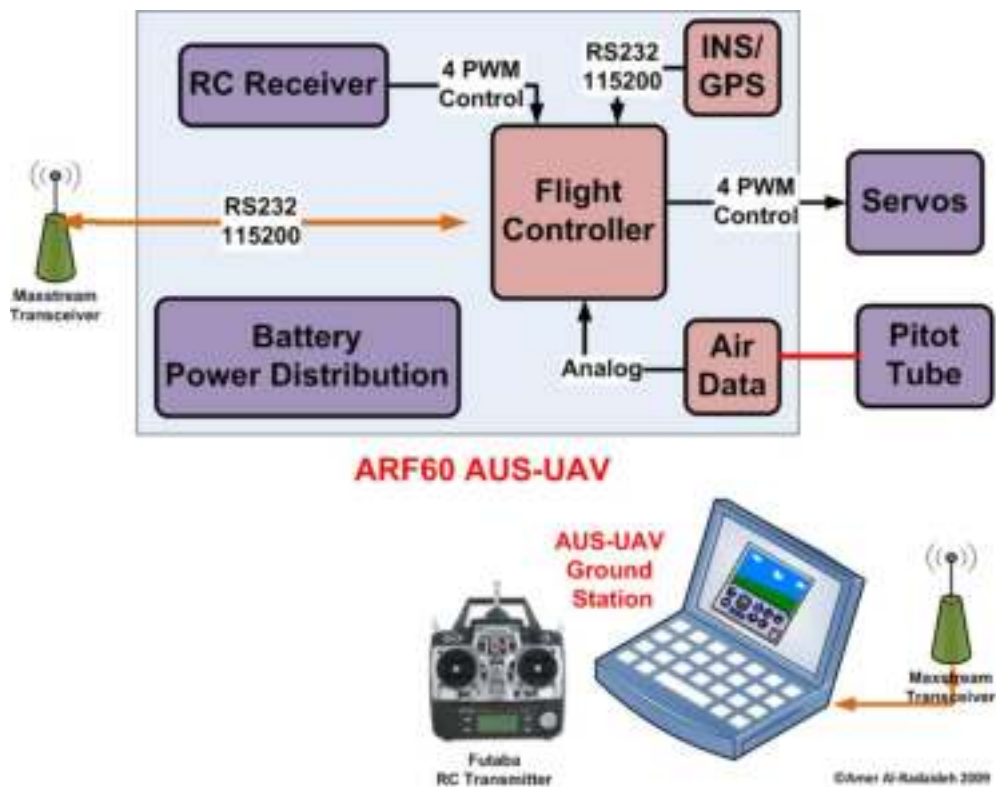


Figure 5.1: AUS Avionics and Ground station Block Diagram

## 5.1 SIGNALS, HARDWARE AND SOFTWARE

In order to provide some insight into the control system integration, the components are briefly discussed.

### 5.1.1 Control Signals

Control signals are the method by which different components exchange information. The two types of control signals used in this project are Remote Control (RC) Pulse Width Modulation (PWM) controller area network (CAN) and serial communications using the RS-232 standard. *RC Pulse Width Modulation* Pulse Width Modulation (PWM) is a technique commonly used to represent an analogue signal using digital circuitry. *Controller Area Network* Controller Area Network (CAN or CAN-bus) is a computer network protocol and bus standard designed to allow microcontrollers and devices to communicate with each other and without a host computer. It was designed specifically for automotive applications but is now also used in other areas. *Serial Communications* Many devices communicate using an asynchronous serial communications port, ones in this project include the IMU.

### 5.1.2 Control Hardware

The control hardware is the hardware used to run the control system or assist in its implementation.

#### dSPACE DS-1103

The dSPACE DS-1104 rapid prototyping platform is a real-time control target that is extensively used in the construction and testing of control systems. The DS-1104 is an expansion card that sits on the host computers PCI bus and contains its own PowerPC CPU and a Texas Instruments (TI) Digital Signal Processor (DSP). Matlab Simulink models are compiled using a cross-C compiler and loaded to the DS-1104 platform. Using the dSPACE software ControlDesk, variables and outputs from the Simulink model are accessible via a Graphical User Interface (GUI). A dSPACE DS-1104 breakout board is shown in Figure The DS-1104 hardware has eight Analogue to Digital (A/D) converters, eight Digital the Analogue (D/A) converters, four PWM



outputs, one asynchronous serial port (either RS-232 or RS-422/485), two encoder readers as well as a host of other inputs and outputs.

#### phyCORE-MPC555 Single Board Computer

A typical embedded system development process requires the evaluation of executable specifications, design implementation by manually writing software, performance tuning by trial and error, and testing using product prototypes. With this traditional approach, errors are often found at or near the end of the development process where they are costly and difficult to fix and can jeopardize the successful completion of the project on time and within the stated budget. These problems become even more critical when the target is a controller with a very intricate architecture such as MPC555. This project demonstrates that the quality of any project depends not merely on the end product, but more on the process involved in developing the product. It reveals the solution to all such process-related problems by means of introducing model-based design. Model-based design clearly defines design specifications, tests systems concepts and automatically develops code for rapid prototyping and software development. The Mathworks provides evolution and adoption of model-based design. Simulink is a software package provided by Mathworks for modeling, simulating, and analyzing dynamic systems. Simulink provides a graphical user interface (GUI) for building models as block diagrams, using drag and drop of blocks from Simulink library. The most attractive feature is Automatic Code Generation of developed model. Along with code reusability, an added advantage that Simulink provides is that the code can be target specific. The advent of processors employing newer technologies and even more complex architectures everyday dictates the need of Target Specific Automatic code Generation. This relieves the design engineers of having the full-fledged knowledge of architecture of target. The best example of a 'next generation' microcontroller is the MPC555, which is exclusively tailored for automotive and industrial applications. MPC555 is a high performance modern automotive microcontroller with a very complex but reliable Power PC architecture. When it comes to developing a system using MPC555, it is a time consuming and tedious job to first study the entire architecture and then write the target specific C/C++ code.

## 5.2 AVIONICS

A picture of the avionics package is shown in Figure 5.2. The unit is mounted on rubber grommets and padded with soft foam inside the aircraft to provide vibration isolation. The avionics comprises the following components on the Printed Circuit



Figure 5.2: AUS Avionics Unit.

Boards (PCB),

- Flight Controller Computer (MPC555 Microcontroller)
- INS/GPS Unit.
- Air Data sensors
- RF Transceiver Module
- Battery and Power Distribution Board

Each of these boards is now discussed in more detail in the following sections.

### 5.2.1 Flight Controller Computer (MPC555 Microcontroller)

Flight Control is responsible for executing all of the control code, interfacing with the high bandwidth sensors such as those on the IMU and Airdata Board and driving the servos. The INS/GPS is interfaced serially, via the RS232 protocol, at 115200 bit per second. The signals from the airdata board are sampled directly by Flight Control using its on-board channels, 10bit Analog to Digital Converter (ADC).



Figure 5.3: MIDG II: Inertial Navigation System (INS) with Global Positioning System (GPS)

To allow Flight Control to switch between safety pilot and autopilot, the servos are driven directly from the Microcontroller. This is done by re-routing the RC receivers PWM signal, containing all of the servos position information. And capture information is using the Time Processor Unit (TPU3). This allows the reading of the input pin and measures an accumulation of time over a specified number of periods. Manually driving the servos allows single control loops to be turned on at a time, while the safety pilot controls the actuators not in use by the autopilot.

### 5.2.2 INS/GPS Unit

The MIDG II is an Inertial Navigation System (INS) with Global Positioning System (GPS) contained in an incredibly small package. This INS GPS package is ideally suited for any unmanned vehicle application that requires an inertial navigation solution. The MIDG II INS/GPS package is specifically designed to be used with the Microbotic Autopilot Platform, but can also be used with other autopilot packages for primary instrumentation.

Message rates are configurable, and individual messages may be polled. All data messages are time stamped with GPS time, and a One Pulse Per Second signal is available for time synchronization in the host computer. Operational mode is selectable, including IMU only operation, vertical gyro simulation with magnetic aiding, and full INS solution. MIDG is intended for use in applications requiring a full state vector, including attitude, position, altitude, velocity, acceleration, and angular rates. All measurements specifications are listed in Table 5.1. MIDG II INS/GPS

## Product Features:

- 3-Axis Rate Gyro
- 3-Axis Accelerometer
- 3-Axis Magnetometer
- Differential Ready GPS; WAAS/EGNOS compliant
- Hardware filters provide vibration immunity
- Advanced filter algorithms for exceptional performance
- Position, Velocity, and Attitude from Kalman Filter at 50Hz

Table 5.1: MIDG II Specifications

Power Requirements	
Input Voltage	10 VDC - 32 VDC
Power	1.2W max (including GPS antenna)
Measurements-Angular rate (all axes)	
Range	$\pm 300^\circ/sec$
Non-Linearity	0.1% of FS
Noise Density	$0.05^\circ/sec/\sqrt{Hz}$
3dB Bandwidth	20 Hz
Measurements-Acceleration (all axes)	
Range	$\pm 6g^3$
Non-Linearity	0.3% of FS
Noise Density	$150\mu g/\sqrt{Hz}$
3dB Bandwidth	20 Hz
Other Measurements	
Attitude Accuracy (pitch and roll)	$0.4^\circ(1\sigma)$
Heading Accuracy	1 – 2°
Position Accuracy	2m CEP, WAAS/EGNOS available
Velocity Accuracy	± 0.2 m/s
Altitude Accuracy	3m WAAS/EGNOS available, 5m otherwise
Data Output Rates	Position , Velocity, attitude, rates, accelerations 50 Hz Raw GPS measurements 5 Hz (WAAS/EGNOS)
Physical	
Size	$1.500W \times .810H \times 1.725D$
Weight	55 grams

### 5.2.3 Battery and Power Distribution Board

The avionics power source is a, 9.6V, 3000mAh NiMH Battery Pack. The battery is connected directly to the Power Distribution Board where it is routed as shown in Figure 5.4. The servos and RC receiver are powered by an unregulated voltage

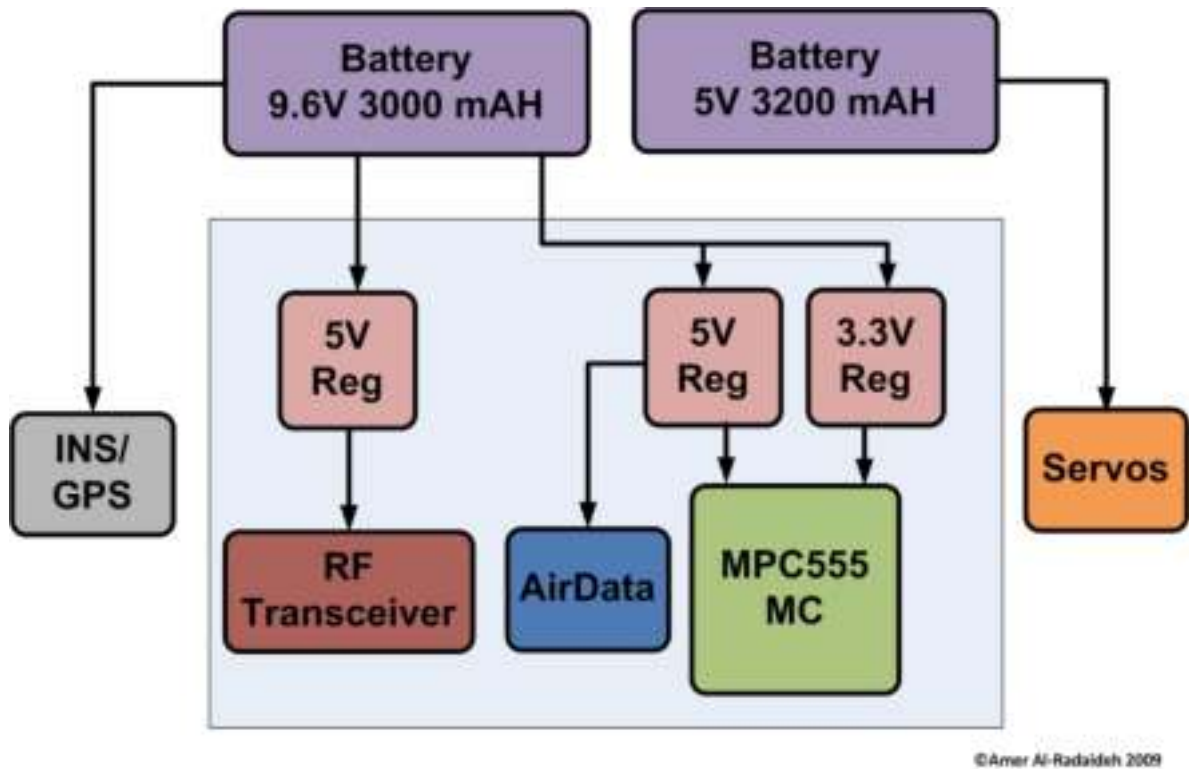


Figure 5.4: Block Diagram of Avionics Power Distribution

supply. This ensures that the servos always have access to a high current source that may be needed in the event of a malfunctioning servo. If a standard regulator were used during this event, it would either shut down or fail, rendering the aircraft uncontrollable which we already faced in our first flight test, see section 7.1.2.

## 5.3 GROUND STATION DESIGN

Figure 5.1 shows that the ground station is made up of a PC running the ground station software, an RF communications module and a RC Transmitter. The RF module provides a wireless link to the aircraft used for telemetry and communications purposes. The ground station PC and the RF module communicate serially, via the RS232 protocol, at 115200 baud. The ground station RF module is set up in exactly the same way as the avionics RF module is. The only modification to the RC

transmitter is that one of its channels is used, in conjunction with a switch in the ground station software, to turn the autopilot on and off. This allows the safety pilot to regain full control over the aircraft at any time.

The rest of this section is devoted to describing the ground station software.

### 5.3.1 Ground Station GUI

The ground station software is a Graphical User Interface (GUI) to the aircrafts on-board avionics package, that allows the autopilot variables to be updated without the need to reprogram the microprocessors. The ground station software is best explained by graphically presenting all of the interface pages and briefly describing the functions that the various group boxes, buttons and text boxes perform.

#### Autopilot Panel

The ARF60 AUS-Autopilot uses a feedback controllers for the elevator, aileron, throttle, and rudder control (see Section 4.2). The Autopilot Panel (Figure 5.5) gives the user the ability to select the control loops available on the autopilot. This panel is used in tuning the PID loops phase.



Figure 5.5: Autopilot Panel-Ground Station

#### Desired Commands Panel

The desired/actual table (Figure 5.6) lists the desired and actual roll, pitch, heading, airspeed, altitude, and turn rate of the UAV. This panel can assist in PID loops tuning as the user need to command the UAV for some set-points to observe the response.

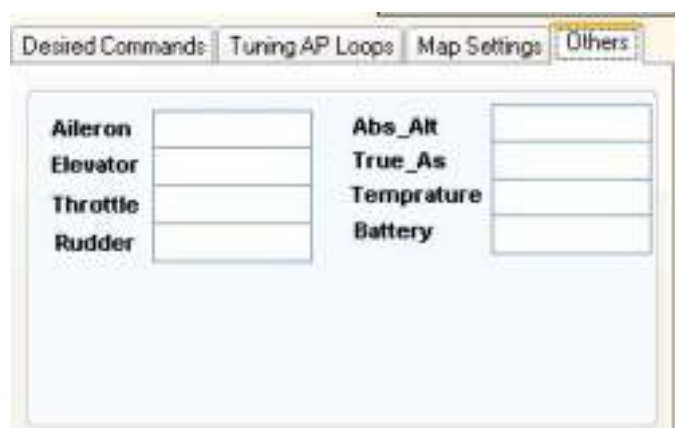


	Desire	Actual	Error
Roll	0		
Pitch	0		
Heading	0		
Airspee	20		
Altitude	50		
Turn	0		
Climb	0		

Figure 5.6: Desired Commands Panel-Ground Station

#### Actuators Monitoring Panel - For Sys ID

The Actuators Monitoring Panel (Figure 5.7) displays the actual position of the UAV actuators as it is read from the servos potentiometer. This panel can be used to get the user input commands for system identification purposes.



<b>Aileron</b>		<b>Abs_Alt</b>	
<b>Elevator</b>		<b>True_As</b>	
<b>Throttle</b>		<b>Temperature</b>	
<b>Rudder</b>		<b>Battery</b>	

Figure 5.7: Actuators Monitoring Panel-Ground Station

#### States Monitoring Panel

The States Monitoring Panel is designed to give a visual reading of the orientation and status of the UAV and other avionics sensor data. There are two different views available, the gauges are used to show the most important states to be monitored visually, while the less important ones are shown numerically. The gauges that were used are the ActiveX Aircraft Instrumentation Library from GMS (<http://www.globalmajic.com/>).

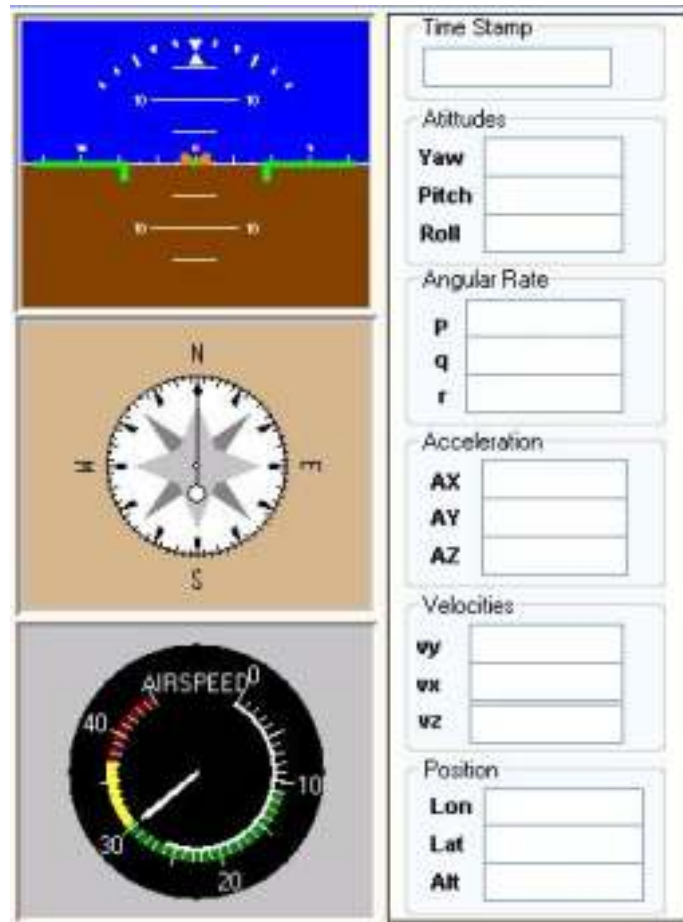


Figure 5.8: States Monitoring Panel-Ground Station

### Ground Station Map

The Map window is used to monitor the position and navigational status of the UAV and to manage the flight plan. The Map displays the position of the UAV and its waypoints. Figure 5.9 shows the map portion of the main Ground Station window. Among other things, it shows a list of the current navigation waypoints as well as indicating the waypoint that the aircraft is flying towards and the path of the aircraft. It also allows waypoints to be added, edited and removed. The map can be customized and configured using the Map Settings window (see Figure 5.10).

### PID Loops Parameters Panel

The PID Parameters area is a table of the PID gains and limits used for control loops tuning.





Figure 5.9: Ground Station Map



Figure 5.10: Ground Station Map Settings

### Data Log Panel

The data log window contains the controls for the telemetry logger. The telemetry logger simply records the pre-defined telemetry from the aircraft to a location on the PC specified by the user. See Figure 5.12.

### Communication Settings Panel

The Communication Settings window is used to select the communications port and list the various baud rates (see Figure 5.13). The communication port will need to be selected the first time the Ground Station is used or any time a different port is

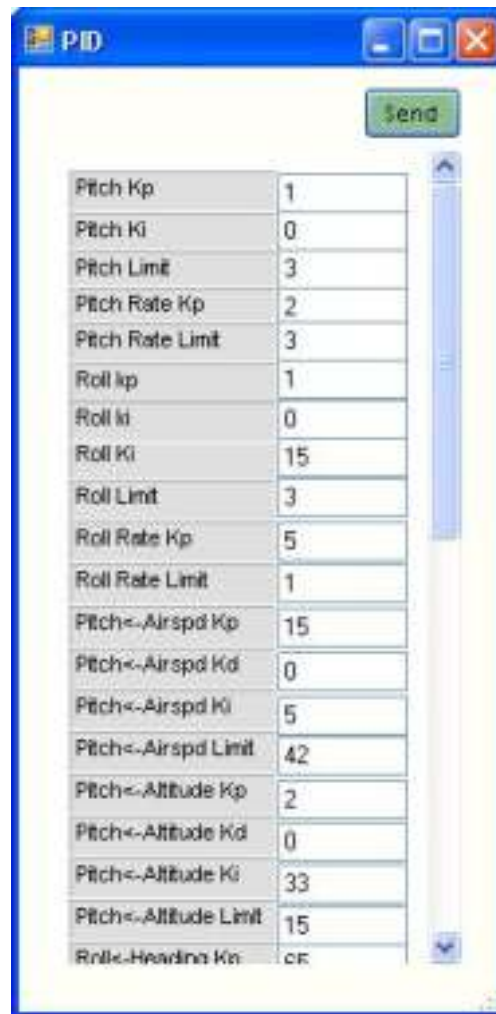


Figure 5.11: PID Loops Parameters-Ground Station



Figure 5.12: Data Log Panel-Ground Station

used. The baud rate was set at 115200.

## 5.4 SUMMARY

This chapter presented an overview of the avionics and ground station developed for the practical implementation of the controller and navigation algorithms of Chapter



Figure 5.13: Communication Settings Panel-Ground Station

4.

The cost, mass and power consumption summary of the avionics package is presented in Table 5.2.

With the controller and navigation algorithms fully designed and the avionics and ground station hardware and software ready, the autopilot is complete and ready for flight tests.

Table 5.2: Cost, Mass and Power Consumption

Item	Cost (\$)	Weight (Kg)	Power (W)
MIDG INS/GPS	7750\$	0.051	1.2 Max
AirData Board	50\$	0.070	
MPC555 Board	519\$	0.1975	
Battery 9.6 V	59\$	0.432	-
Battery 5 V	39\$	0.236	-
Transceiver	149\$	0.0665	1 Max

## CHAPTER 6

# HARDWARE IN THE LOOP SIMULATION (HILS)

Simulation is an important phase that must be completed prior to any real world practical testing. Unlike previously when mathematical models did not exist, excess money was needed to test actual prototypes of real systems. A classic example is the auto industry. In fact, there was no way of knowing before making the prototype or the real system if it would work as specified. If system were high powered machinery that performed dangerous operation, failure of the equipment would often be catastrophic and lead to losses in life. Currently modern systems are always by default simulated in software before the actual prototype is tested. With the accumulation of knowledge, it is possible to acquire accurate mathematical models of complete systems, and test them quickly due to advances in computing power. Thus simulations reduce costs, and increases efficiency. Pure simulation is often used to understand the behavior of a system, or to predict an outcome under different internal and external influences. Unfortunately although a pure simulation alone is not enough to predict all possible outcomes due to the fact that not all practical considerations may be taken into account. For most real systems, there are characteristics that are unknown or too complex to model by pure simulation. That is why nowadays Hardware in the Loop Simulation (HILS) testing is done. HILS is basically a specific form of simulation, where a part of the mathematical model is replaced by the actual hardware. Good system engineering practice would begin with a pure simulation and as components become better defined with the aid of simulation, they can be fabricated and replaced in the control loop. Once physical components are added to the loop, un-modeled characteristics can be investigated, and controls can be further refined. The use of HILS eliminates expensive and lengthy iterations in machining and fabrication of parts, and speeds development towards a more efficient design (Hadi, 2005).

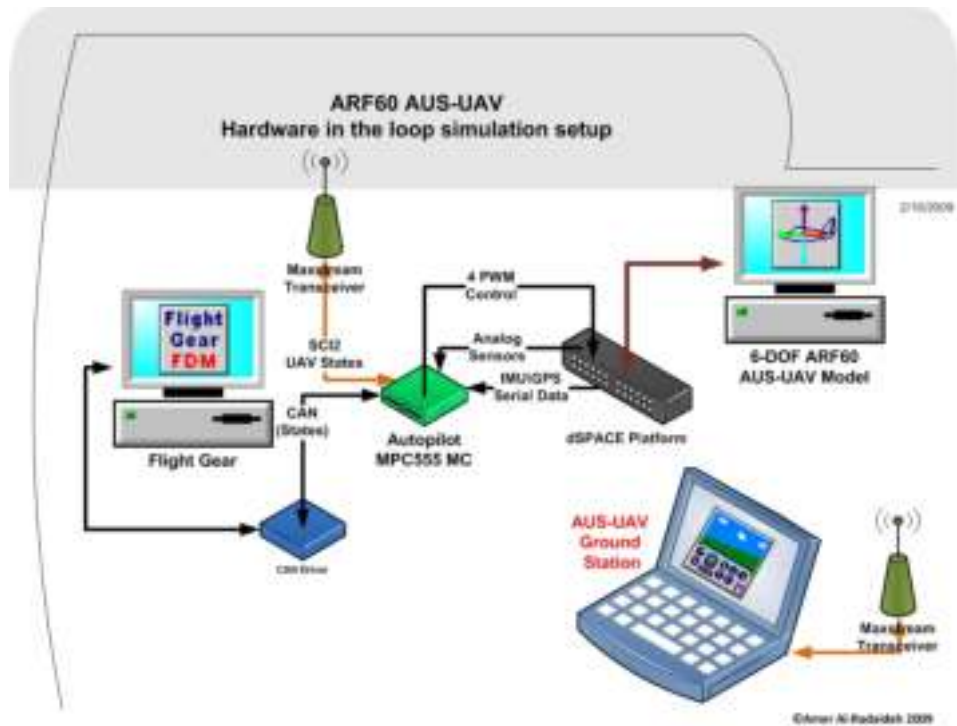


Figure 6.1: Hardware-in-the-loop (HIL) simulation Setup

## 6.1 HARDWARE IN THE LOOP SIMULATION DEVELOPMENT

This section describes the details of developing a realistic simulation environment based on Matlab/Simulink. A complete 6-DOF nonlinear aircraft model with a linear approximation of the aerodynamic forces and moments is used to simulate realistic dynamic behavior of the aircraft. The nonlinear aircraft model also involves the detail modeling of subsystems such as sensors and actuators using experimental data. In addition, the external pilot command input and the flight visualization enable the simulation to be used as a virtual flight test. The actual autopilot hardware is placed inside the simulation loop in order to test and validate both the hardware and the on-board software. Four independent computer systems were used in the hardware-in-the-loop (HIL) simulation as illustrated in Fig 6.1: the 6-DOF simulator, the flight visualization computer, the autopilot micro-controller, and the ground station computer console.

### 6.1.1 ARF60 UAV 6-DOF model simulator

A full 6-DOF nonlinear model for the ARF60 AUS-UAV was built in Matlab/Simulink environment. The 12 states differential equations of motion in Eqs.2.4 - 2.8 are utilized

in conjunction with an approximation of the aerodynamic forces and moments via component buildup. The stability and control derivatives are either obtained in the manner as discussed in Section 3.4.1 or 3.4.2. The stability and control derivatives from the geometry of the aircraft was chosen during the early phase of development, however, once these derivatives have been identified experimentally, the identified values are used for realistic simulation results. The output states from the simulator are processed to emulate real sensors accounting for sensor latency, random walk bias, and measurement noise. After digitized according to the word size of the microcontroller (10 bit, 1024 steps), the sensor values are transmitted to the autopilot via a serial communication. In a similar manner, the navigation states are processed for data latency and measurement noise and encapsulated in a binary GPS packet identical to the actual GPS sensor output. This packet is also transmitted to the autopilot at an update rate of (50 Hz) via the serial communication baud rate of (115200 bits per second). In the HILS environment, the autopilot functions identically as in a real flight test, while computing control commands to each control actuator. These commands are sent back to the 6-DOF simulator in order to drive the actuator model of the control surface. Each control surface was modeled as a first order system with saturation limit, whose parameters were identified experimentally. Consequently, a simulation loop is formed between the 6-DOF simulator (software) and the autopilot (hardware) exchanging the simulated data back and forth.

### 6.1.2 R/C transmitter

An R/C transmitter is connected to the 6-DOF simulator for recording remote pilot stick commands: Four channels for control surface commands ( $\delta_a$ ,  $\delta_e$ ,  $\delta_r$  and  $\delta_t$ ) and auxiliary commands for toggling between autonomous control mode and remote pilot mode. The remote pilot stick commands can override the autopilot control command at any time by switching the commands to the actuator models at users choice. In this case, a simulation for an open loop maneuver can be conducted along the remote pilot input to validate the dynamic characteristic of the aircraft model. In order to visualize the simulation, we adopted the use of FlightGear (v1.9.1, 2009), an open source flight simulator for a visualization tool. The FlightGear is a flight simulator framework, which has been widely used in various research environment. Although it provides a total simulation environment in conjunction with the internal flight



Figure 6.2: Hardware-in-the-loop (HIL) simulation environment

dynamics models, we used the FlightGear as a visualization tool combining with the 6-DOF simulator already developed. By doing this, the FlightGear receives the simulated states from the simulator at a fixed update rate to constantly refresh the virtual scenes that have been generated along the users convenient view angles. The ability to record the pilot stick command with visualizing via the FlightGear allows the simulation environment to replace a real experiment to save time and effort. An open loop behavior of the UAV can be tested and validated by a remote pilot via the user friendly input device, and the closed loop control performance can be verified and demonstrated by conducting virtual experiments in advance to the real flight test. Figure 6.2 shows a computer screen shot taken during the HILS simulation visualizing the dynamic behavior of the UAV, while displaying the corresponding state variables in the scopes.

### 6.1.3 Data communication and synchronization

The 6-DOF simulator exchanges the sensor and control command signals with the autopilot via a serial communication between the two. The sensor output data include 16 different sensor outputs from rate gyros, accelerometers, magnetometers, and etc., and are packed into a custom-designed binary packet. The binary packet begins with a designated header to distinguish between different packets and ends by a trailer for data consistency check. The serial communication is configured for a baud rate 115200 bps, which allows communicating by transmitting the sensor packet of 45

bytes at 50 Hz as well as the GPS navigation solution packet of 35 bytes at 50 Hz update rate. The control command data from the autopilot are composed of four PWM commands for each actuator, resulting in a binary packet of 36 bytes in length associated with header and trailer to be transmitted at 50 Hz update rate. The HILS bridge shown in Figure 6.1 was then incorporated into the 6-DOF Simulink model to handle the bidirectional communication with a help of the serial communication block toolbox (Leonardo, ). In addition, a dedicated S-function block is utilized to send simulated output to the FlightGear (v1.9.1, 2009). Because the multiple systems are involved in the HILS simulation, it is all important to keep the execution timing among these systems properly synchronized during the entire simulation period for data compatibility among them. Besides, a real-time execution is necessary for the simulation to be in accord with the pilot input and the visualization at correct time step. Although the 6-DOF simulator was written in a Simulink model running at non real-time, a real time execution was accomplished by utilizing the Realtime block toolbox and dSPACE environment (dSPACE, ). This toolbox (dSPACE) makes control engineers lives easier with real-time tools for rapid control prototyping, production code generation, and hardware-in-the-loop simulation. For a real time simulation, the basic simulation time step of the 6-DOF simulator is carefully chosen at 100 [Hz] taking into consideration both the computational overhead and the faithful simulation results for accurate dynamic characteristics of the UAV. A different sampling rate at 50 [Hz] was utilized for the serial communication block and the FlightGear S-function block. The synchronization of the data was implicitly dealt with in a manner that the main simulation loop of the 6-DOF simulator polls each communication block at a fixed interval during the simulation, whereas the autopilot and the FlightGear receive the packets passively.

#### 6.1.4 HILS Summary

A hardware-in-the-loop simulation environment has been built to validate hardware and software development of the autopilot for a small UAV. A full 6-DOF nonlinear dynamic model has been used in conjunction with the linear approximation of the aerodynamic forces and moments. A batch parameter identification method has been used to determine the stability and control derivatives of the UAV using flight test data. Detailed models for the sensors and actuators were incorporated in the



simulation along with the capability of real-time 3-D visualization and external pilot interface. The hardware-in-the-loop simulation is an indispensable tool for performing simulated flight tests in support of avionics development and validation of control laws for small UAVs with minimal cost and effort.

## 6.2 HARDWARE IN THE LOOP SIMULATION RESULTS

### 6.2.1 HILS Autopilot Results

In this section two tests were conducted to check the autopilot behavior. In those tests the wind disturbances were included; [ $W_x = 5, W_y = -3, W_z = 0$ ]. The first test included; holding a fixed airspeed, fixed altitude and a bank angle commanded to a square wave with a specific amplitude and frequency. While, the second test included; holding fixed Airspeed, fixed bank angle and the altitude commanded to a sine wave with a specific amplitude and frequency.

#### HILS Autopilot Test 1

The first test hold the Airspeed to  $20m/s$ , the altitude to  $50m$ . The bank angle command is a square wave with an amplitude of  $30^\circ$ . The Bank angle was following the commanded one as Figure 6.3 shows the attitude results.

#### HILS Autopilot Test 2

The second test hold the airspeed to  $20m/s$ ,  $0^\circ$  bank angle and the altitude commanded to a sine wave with  $8m$  amplitude as a variation from the trimmed altitude ( $50m$ ). Figure 6.4 shows that the altitude following the sine command also the pitch angle and was varying accordingly. The airspeed was following the command as well.

### 6.2.2 HILS Trajectory Tracking Results

In this section the Bidirectional Feedback Guidance Strategy Trajectory Tracker (see section 4.2.4) was tested using the HILS. two navigation tests were conducted. The results for two waypoints navigation listed in section 6.2.2 while the hourglass shape (4 waypoints navigation) results listed in section 6.2.2.

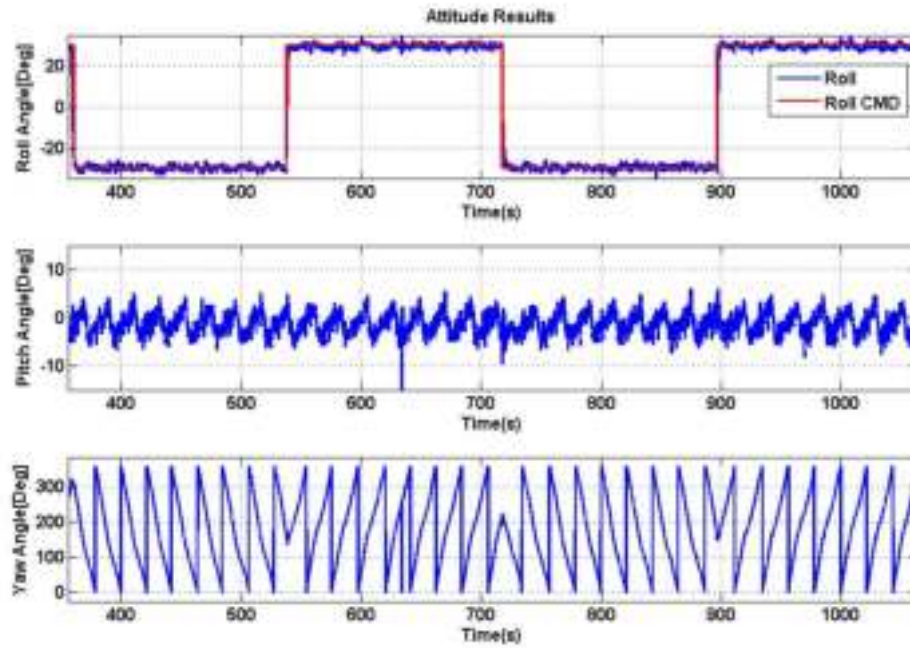


Figure 6.3: HILS Autopilot Test 1 -Attitudes

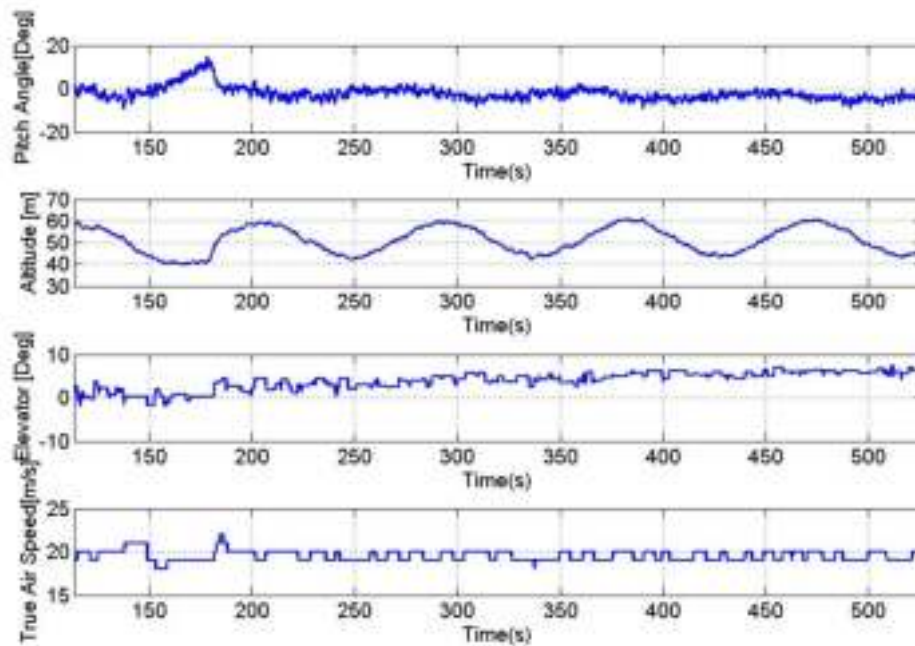


Figure 6.4: HILS Autopilot Test 2 - States Results

### HILS Trajectory Tracking Results-2WP Navigation

Two waypoints were feeded to the trajectory tracker to follow. Figure 6.5 show the 2D plot for the navigation between 2 waypoints with a distance of 500m in between. The 3D plot and the map for the trajectory are shown in Figures ?? and 6.7. Figure

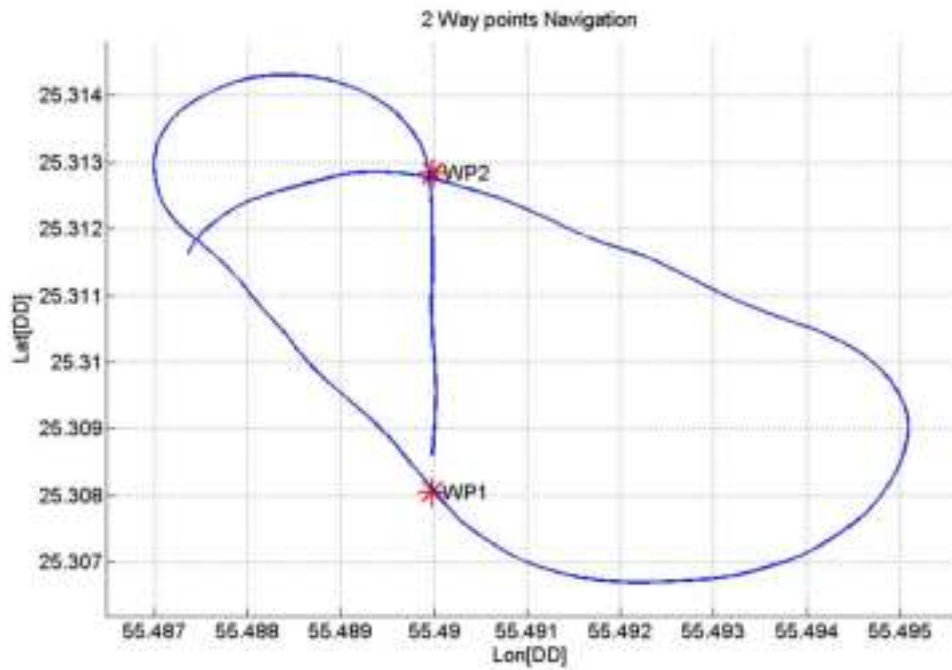


Figure 6.5: 2WP Navigation-2D

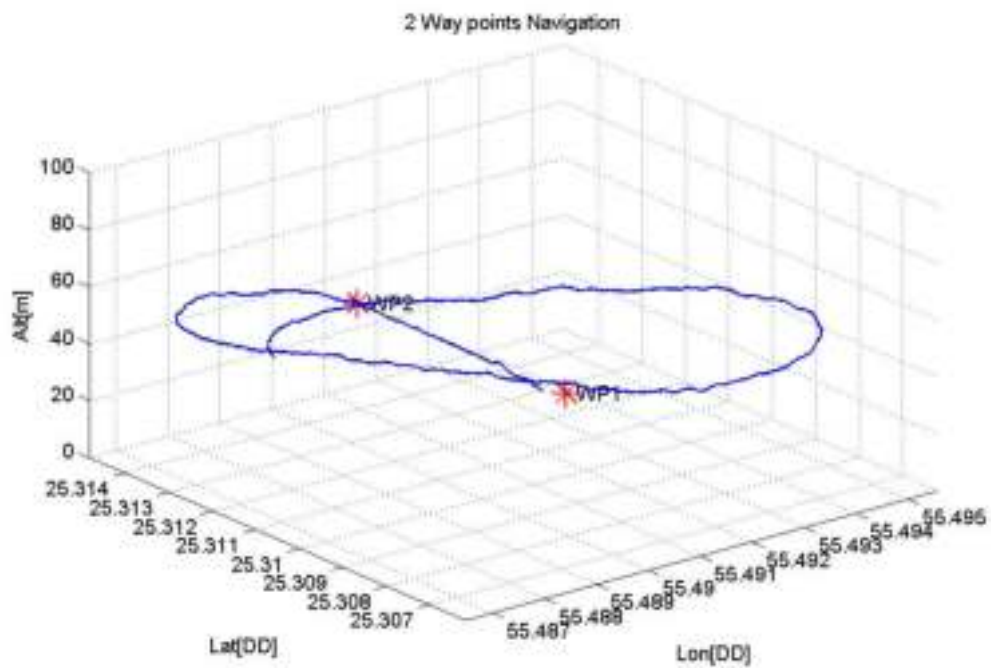


Figure 6.6: 2WP Navigation-3D

6.8 shows the attitudes of the aircraft for this trajectory. The reader can see the how the aircraft was switching to the  $\pm 10^\circ$  to perform the navigation according to the Bidirectional Guidance Strategy.



Figure 6.7: 2WP Navigation-Map

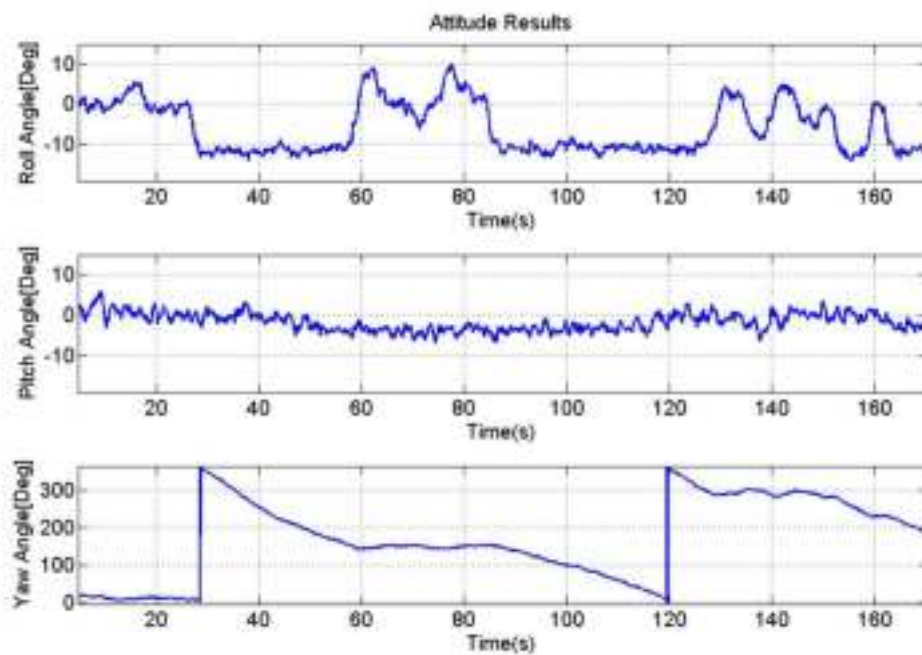


Figure 6.8: 2WP Navigation-Attitudes

### HILS Trajectory Tracking Results-4WP Navigation Hourglass Shape

Four waypoints (hourglass shape) were fed to the trajectory tracker to follow. Figure 6.9 shows the 2D plot for the navigation between the four waypoints. The 3D plot and the map for the trajectory are shown in Figures 6.10 and 6.11. Figure 6.12 shows

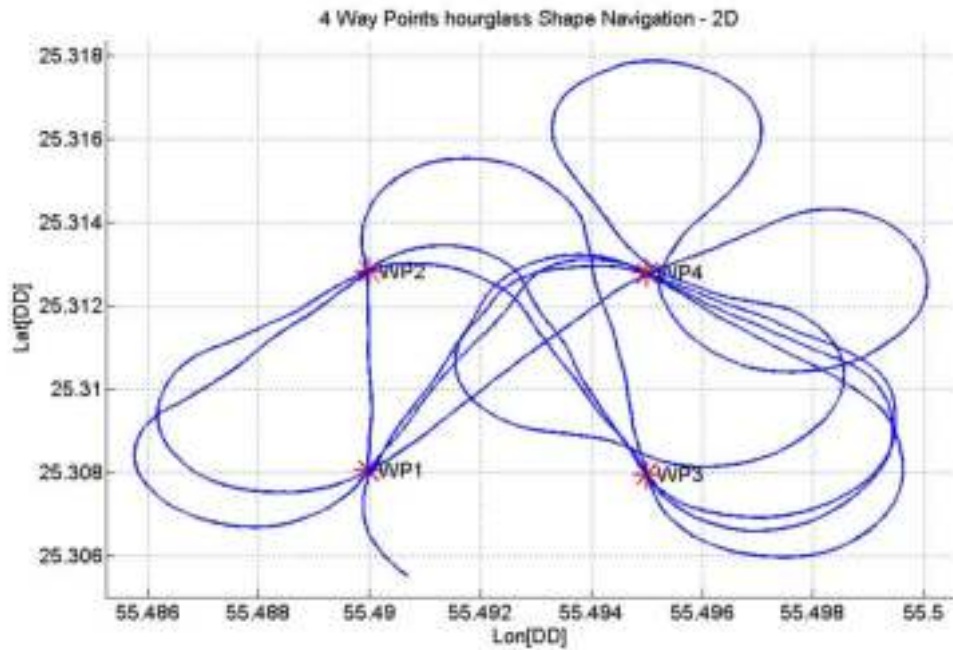


Figure 6.9: 4WP Navigation (Hourglass Shape)-2D

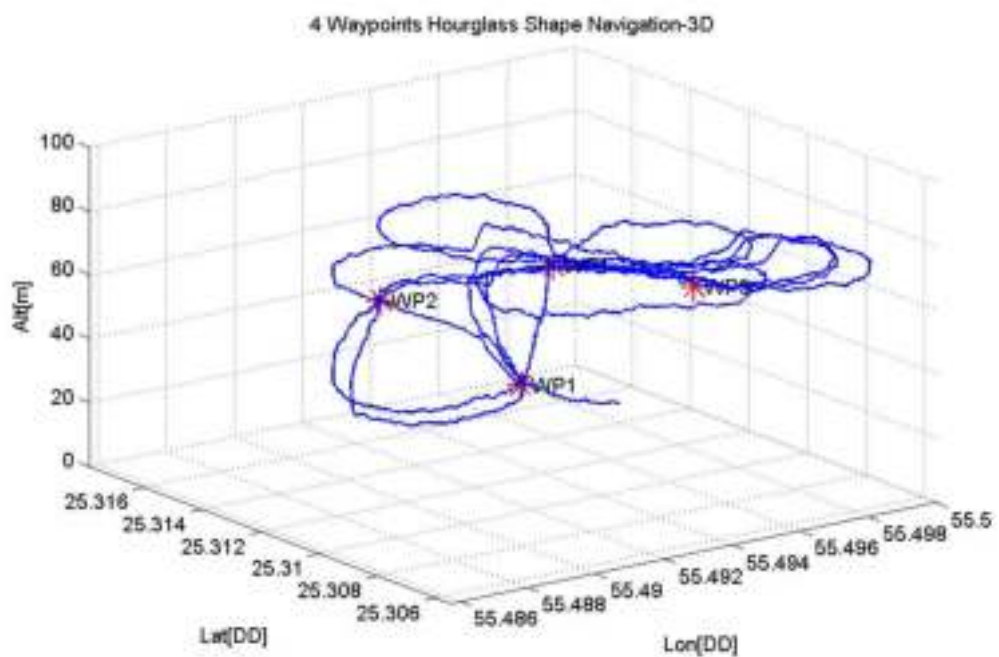


Figure 6.10: 4WP Navigation (Hourglass Shape)-3D

the attitudes of the aircraft for this trajectory. Figure 6.14 shows how the aircraft was switching to the  $10^\circ$  to perform the navigation according to the Bidirectional Guidance Strategy.



Figure 6.11: 4WP Navigation (Hourglass Shape)-Map

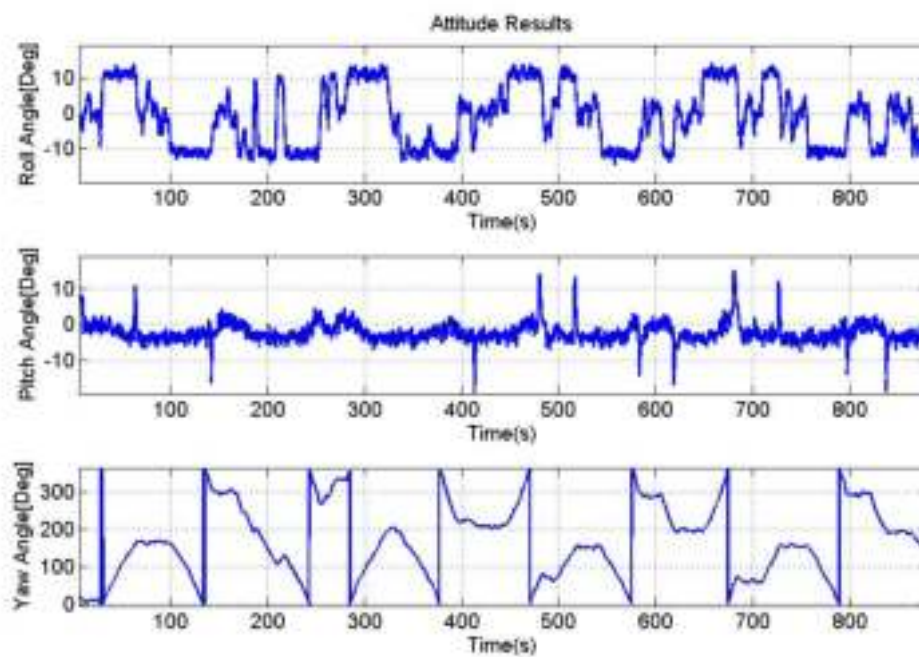


Figure 6.12: 4WP Navigation (Hourglass Shape)-Attitudes

## CHAPTER 7

# FLIGHT TESTS RESULTS AND AUTOPILOT TUNING

This chapter outlines a 3rd party autopilot mounting and tuning. It begins by introducing the kestrel autopilot, a commercial off the shelf autopilot. Then, it proceeds to the discussion of the flight testing results in terms of loops tuning and trajectory tracking. Furthermore, the designed autopilot for the ARF60 AUS-UAV is discussed in terms of the utilized hardware, tuning steps and trajectory tracking results. Finally, we concluded by benchmarking the ARF60 AUS-UAV autopilot with the kestrel autopilot in terms of accuracy.

### 7.1 KESTREL AUTOPILOT OVERVIEW

Kestrel autopilot, shown in Figure 7.1, was integrated in the ARF60 aircraft. This autopilot is used to bench mark the designed autopilot at AUS and compare their capabilities. A variety of sensors were used to provide the necessary data for autonomous control of the UAV. These sensors include three magnetometers, three rate gyros, three accelerometers, a differential and absolute pressure sensors, a GPS sensor, and three temperature sensors. The Kestrel uses an onboard 8-bit 29MHz processor to handle all the sensor data and run the necessary code for controlling the aircraft via four servo ports on the actual Kestrel unit and eight additional servo ports on a servo expansion board. The Kestrel uses a Maxstream 9XTend 900MHz 1000 mW wireless modem to communicate with the ground station; this connects to the bottom face of the autopilots PCB board through the modem header. The two components were then secured together with heat shrink tubing to prevent any separation during normal operation. Furthermore, the Kestrel autopilot can perform GPS navigation using waypoints uploaded to the autopilot from the ground station. Figures 7.2 and 7.3 show the block diagram of the Kestrel autopilot and its main components respectively.



Figure 7.1: Kestrel Autopilot

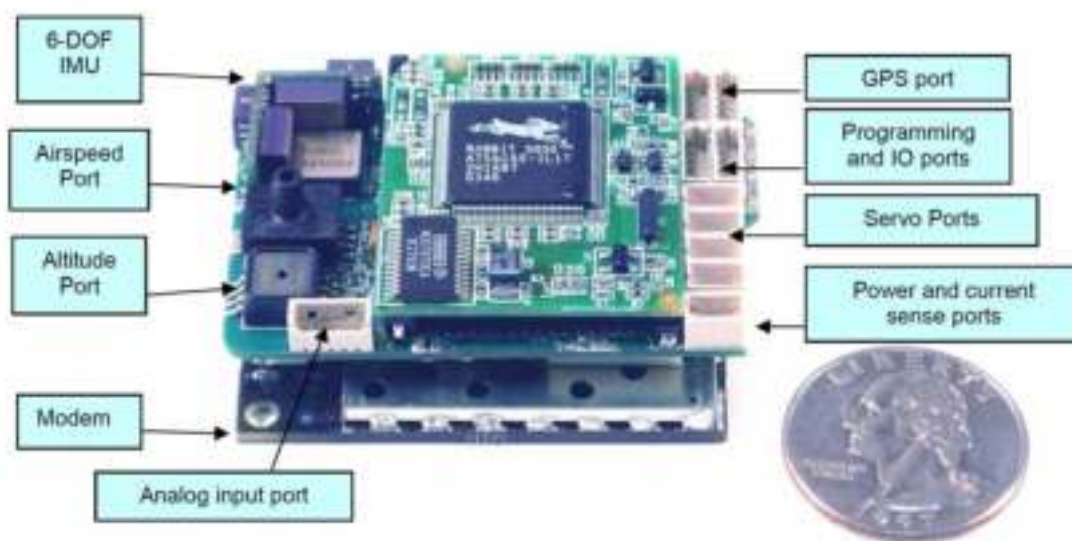


Figure 7.2: Kestrel Autopilot Diagram

### 7.1.1 Mounting Kestrel Autopilot on the ARF60 UAV

The autopilot, pitot static tube, GPS, and radio modem antenna were installed correctly in the ARF60 aircraft.

The autopilot was installed flat with spacers of 15 mm long from the aircraft fuselage bottom (see Figure 7.4). Then, set of rubbers were used to decrease the effect of the engine vibration, Figures 7.5 and 7.6 shows the how the rubbers were mounted. An aluminum box was designed to house the autopilot in order to protect



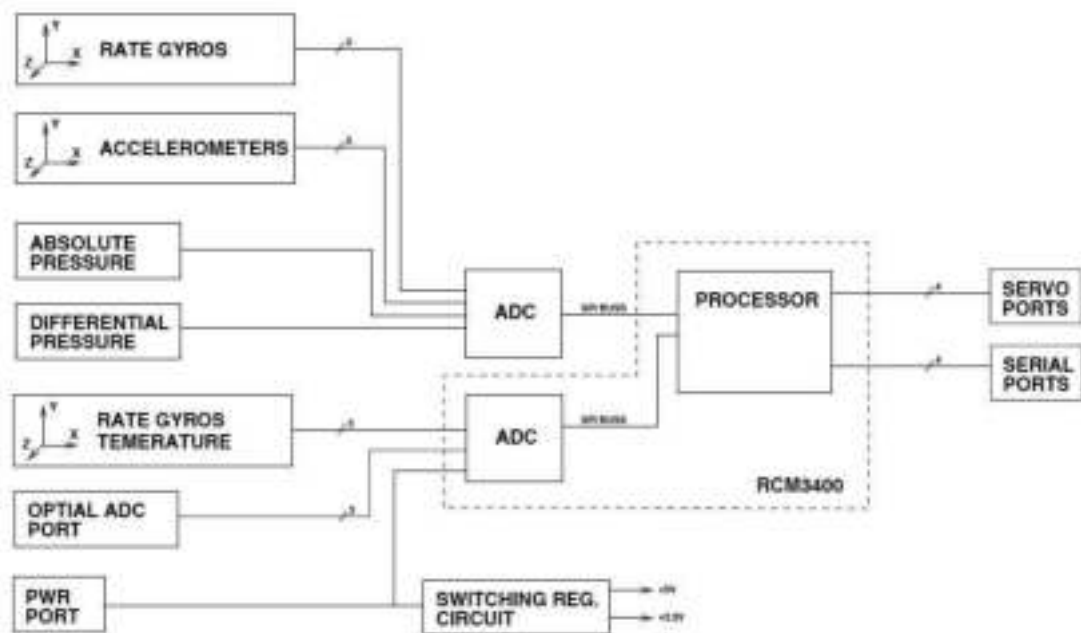


Figure 7.3: Kestrel Autopilot Block Diagram

it in the event of a crash or hard landing. Figure 7.7 shows the autopilot installed in the airframe inside the aluminum box.



Figure 7.4: Kestrel Autopilot with spacers

The GPS receiver is one of the most important autopilot sensors. Without GPS reception, the aircraft cannot estimate its position, ground speed, or ground track. Loss of GPS reception during flight can result in the loss of the aircraft, as the autopilot cannot navigate. The GPS unit was mounted in such a way that the antenna



Figure 7.5: Kestrel Autopilot isolation from inside



Figure 7.6: Kestrel Autopilot isolation from outside

has a clear view of the sky. To significantly improve the GPS receiver performance a ground plane  $2 \times 2$  inches was added under the antenna. Figure 7.8 shows the GPS location on the aircraft.

The digital radio modem is a key element of the autopilot system. Without the digital modem, there is no way to communicate with the aircraft during flight. Maxstream 9XTend 900MHz with 115k baud rate TTL level digital modem was used with the autopilot. This modem is lightweight and, with a decent antenna, can



Figure 7.7: Kestrel Autopilot inside the Aluminum box



Figure 7.8: GPS Location on the aircraft

achieve ranges greater than 10 kilometers. A simple lightweight antenna was mounted vertically on the ARF60 aircraft fuselage. The antenna location is shown in Figure 7.9.

The pitot system is critical for correct airspeed and altitude readings. The airspeed measurement is derived from a differential pressure sensor that measures the difference between static pressure and the pressure from the forward airspeed. The pressure port on the differential pressure sensor was connected using silicon fuel tubing



Figure 7.9: RF Antenna Location on the Aircraft

to the pitot static tube. On the other hand, the altitude measurement is derived from an absolute pressure sensor that measures the static pressure. The pressure port on the absolute pressure sensor was connected using silicon fuel tubing to the static tube of the pitot system. The pitot static tube was mounted such that the open end is in the path of the forward air stream in the direction of flight. The pitot static tube location was picked in an area that will not be exposed to the propeller wash or significant turbulence. Figures 7.10 and 7.11 show the pitot tube installation.



Figure 7.10: Pitot Static Tube Location on the Aircraft



Figure 7.11: Pitot Static Tube Location on the Aircraft

### 7.1.2 Flight Testing Using Kestrel Autopilot

Before attempting autonomous flight for the first time, the autopilot was correctly configured. Configuring the autopilot includes configuring servos correctly, setting airframe dependent feed forward control parameters, configuring navigation parameters, setting user commanded limits and configuring joystick were the first steps to go through on the ground.

Then, the autopilot is tuned using the following procedure:

**First Flight Test** The first flight was conducted to verify the operation of the autopilot, sensors outputs, pilot-in-the-loop (Manual control) and the digital communication range. This test was repeated twice since one aircraft is crashed during the first test. The crashing of the aircraft was due to mechanical connection failure of the aileron servos. To continue the flight test, another identical aircraft was prepared with the same autopilot and sensors installations. The repeated test was successful and the expected outcomes were fulfilled. Table 7.1 lists the data calibration. Figures 7.12 and 7.13 show the crashed test, note the securing design protected the autopilot.

**Second Flight Test** The objective of this test was to tune the Stability Augmentation System (SAS). The rate damping PID loops damp the aircraft rotation around the pitch, roll, and yaw axis. These three damping loops were tuned

Table 7.1: Calibration data

Trim Airspeed	14 m/s
Trim throttle	50 percent
Trim Angle of Attack (AOA)	2 deg



Figure 7.12: Crashed test (1)



Figure 7.13: Crashed test (2)

Table 7.2: Stability Augmentation System (SAS) gains

Tuned Parameter	gain value
Yaw Rate PID loop (Kp)	
Roll Rate PID loop (Kp)	
Pitch Rate PID loop (Kp)	

based on the PID tuning methods. A starting point is found by enabling those loops while on the ground. Then moving the aircraft in the pitch, roll, and yaw axis, and observing the aircrafts response. During flight, the proportional gain (Kp) of each damping loop was increased slowly. As Kp increases, the aircraft damps more around the corresponding axis. The pilot feedback was used to verify that the aircraft is becoming more damped around the correspond axis. We continued increasing the value of damping Rate Kp of each loop until small instabilities are noted in the corresponding axis and then we lowered the value by 25 percent or more until the instabilities disappears. Table 7.2 lists the values of the gains after on-flight tuning for the SAS.

**Third Flight Test** The purpose of the third flight test was to tune the inner attitude hold loops and the outer airspeed and altitude hold PID loops. Since tuning these loops is very demanding, several flight tests were conducted to accomplish a proper tuning of these gains. Tuning these gains are done using the same procedure described in the second flight test.

As can be seen from Figure 7.14 the roll attitude hold was performing nicely when the autopilot was engaged. A mean of  $-0.7405$  and a median of 0 shown in Figure 7.15 for the error analysis. The map in Figure 7.16 shows the circles achieved by the aircraft. It is obvious there was drifting because of the wind. Figures 7.17-7.19 shows better results after minor tuning.

Tables 7.3, 7.4 and 7.5 list the values of the gains after on-flight tuning.

**Fourth Flight Test** The purpose of the fourth flight test was to verify waypoint navigation and loiter work correctly. Different tests were conducted. The first test was the loiter pattern (see Figure ??) with radius of  $150m$ . The results for this navigation test are shown in Figures ??-7.26. The results give a good

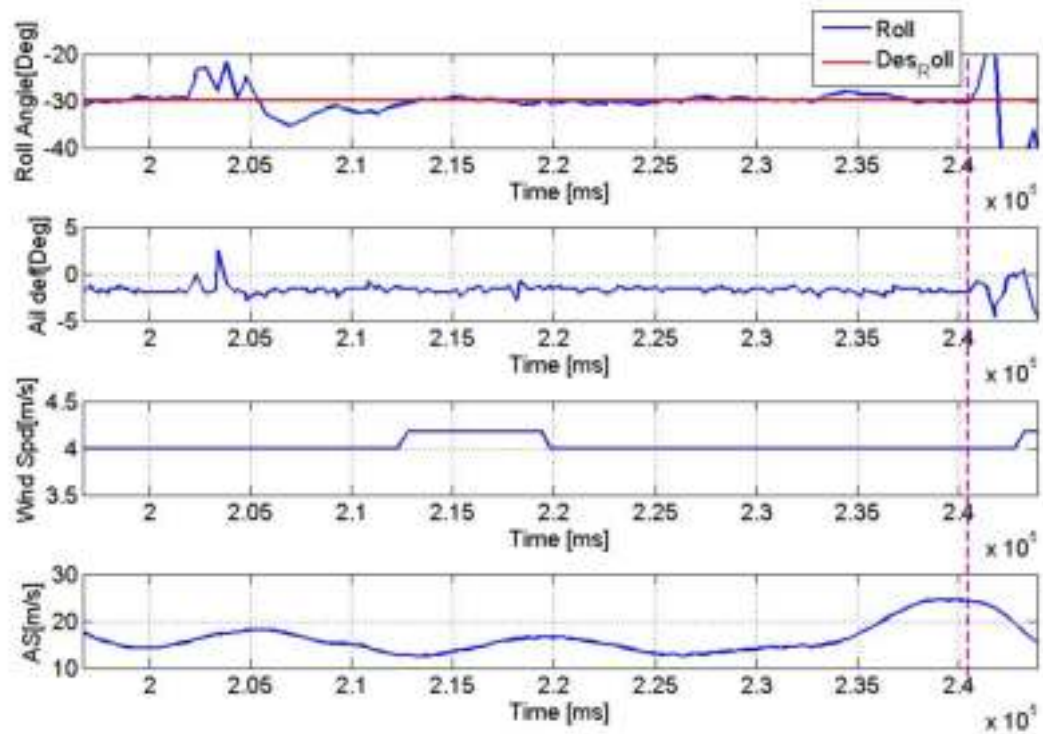


Figure 7.14: Roll Hold Test1

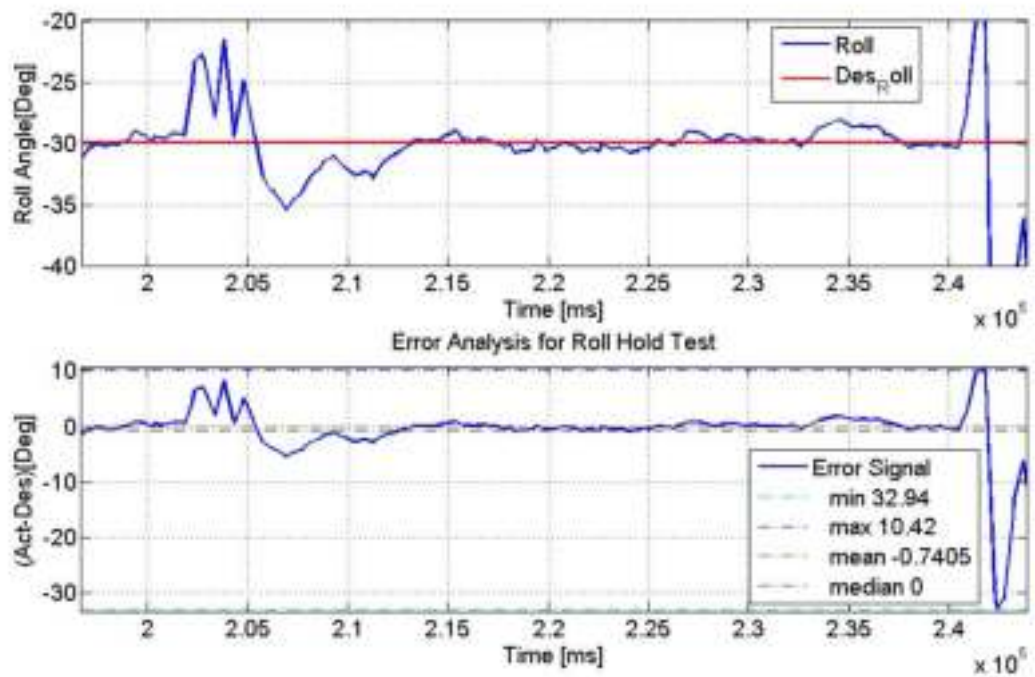


Figure 7.15: Roll Hold Test1 Error Analysis

impression about the tuning that has been done as the commanded signals were followed nicely.





Figure 7.16: Roll Hold Test1 Map

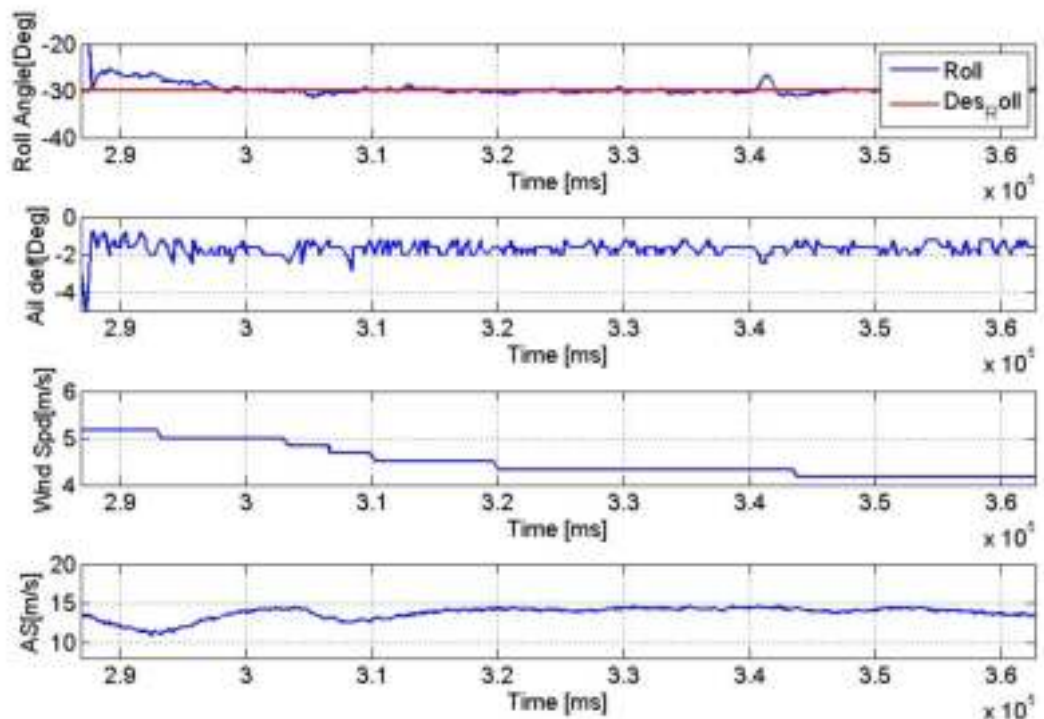


Figure 7.17: Roll Hold Test2

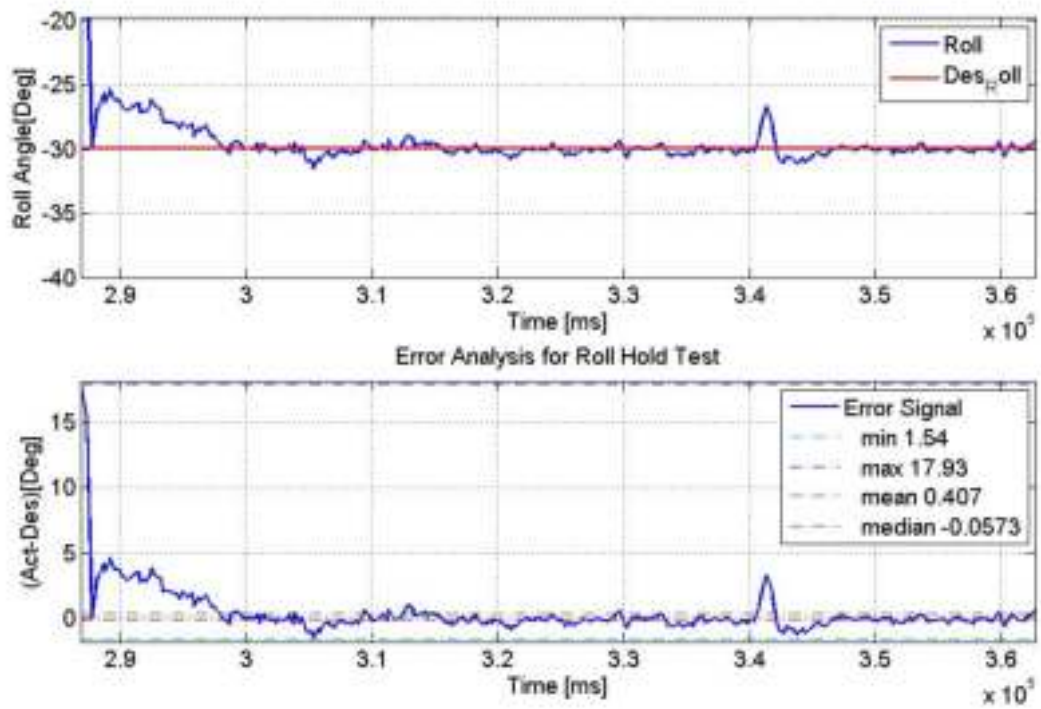


Figure 7.18: Roll Hold Test2 Error Analysis



Figure 7.19: Roll Hold Test2 Map

Another loiter test with radius of  $100m$  is conducted with the results shown in

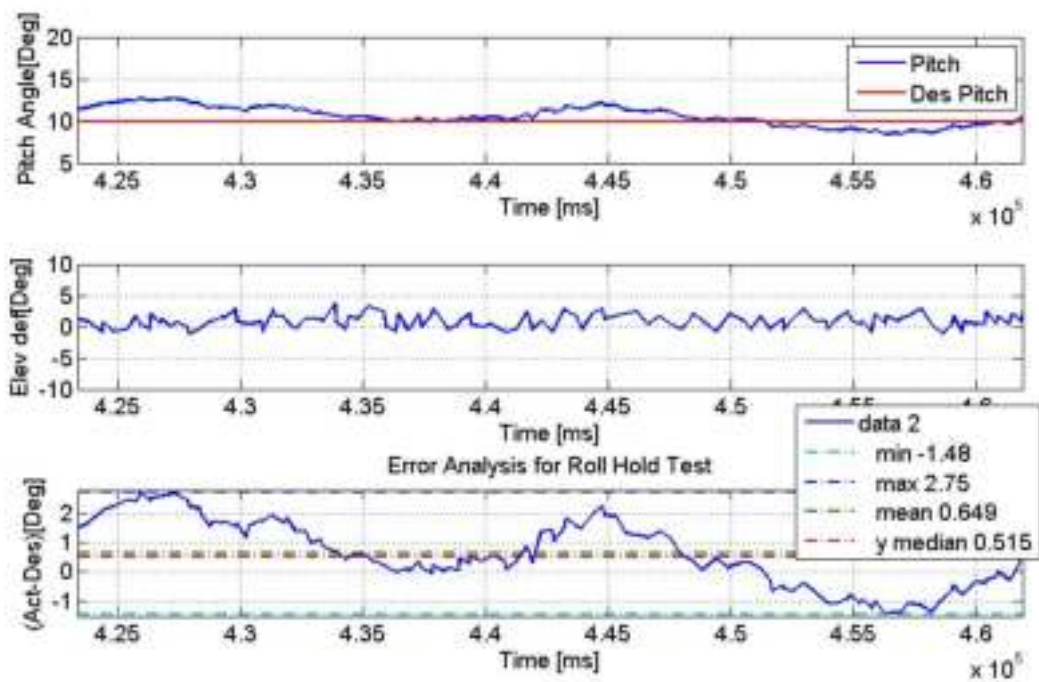


Figure 7.20: Pitch Hold Test

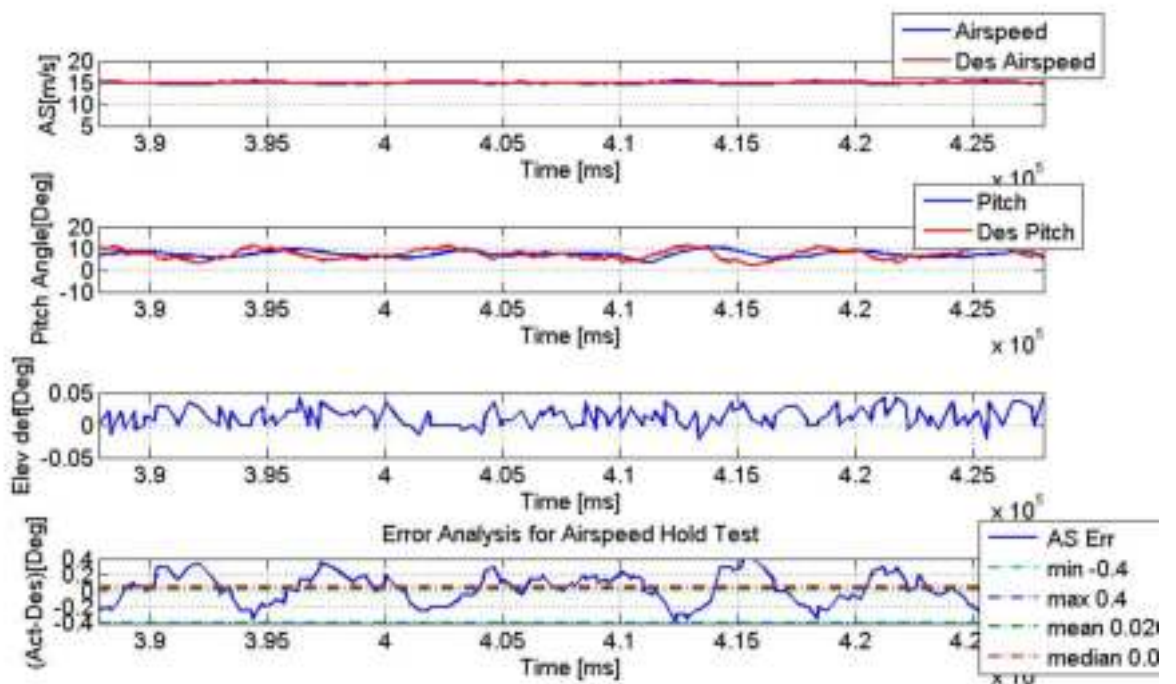


Figure 7.21: Airspeed Hold Test

Figures ??-??.

Four waypoints trajectory, shaped a square pattern (see Figure 7.27), was the

Table 7.3: Inner Attitude Hold Loops gains

Tuned Parameter	gain value
Roll PID loop	
Kp	
Ki	
Kd	
Pitch PID loop	
Kp	
Ki	
Kd	

Table 7.4: Outer Airspeed Hold PID Loops Gains

Tuned Parameter	gain value
Pitch from Airspeed PID loop	
Kp	
Ki	
Kd	
Throttle from Airspeed PID loop	
Kp	
Ki	
Kd	

second test for the navigation. The square has  $872m$  and  $852m$  two legs length. Figure 7.28 shows the path followed. The aircraft visited the four waypoints. The analysis for the attitudes, altitude and the airspeed are shown in Figure 7.29. The 3D trajectory shows how the aircraft was losing altitude when it was switching between the waypoints as this needs more banking. This aircraft was commanded to do the trajectory four times. Figures 7.31-7.33 shows some consistency between the four laps behavior.

Table 7.5: Outer Altitude Hold PID Loops Gains

Tuned Parameter	gain value
Throttle from Altitude PID loop	
Kp	
Ki	
Kd	
Pitch from Altitude PID loop	
Kp	
Ki	
Kd	

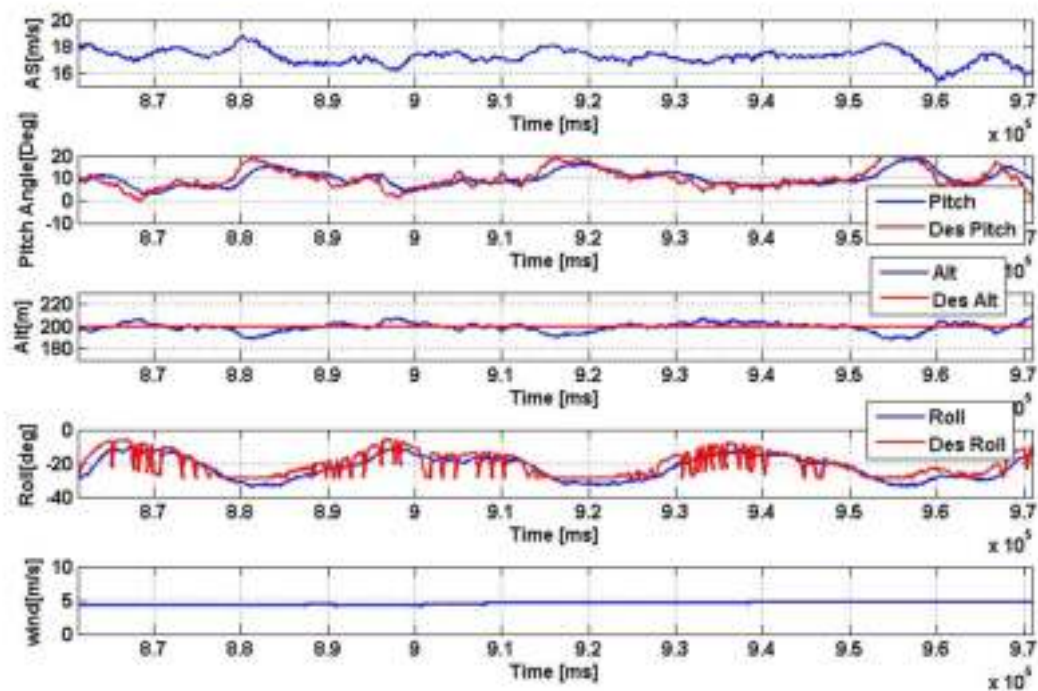


Figure 7.22: 150m Loiter Test

The third trajectory was the sandglass (hourglass) pattern with  $872m$  edges and  $1207m$  diagonals (see Figure 7.34). In contrast to the square pattern, the hourglass pattern allow to test that right and left turns as they have equal representation. The four waypoints have the same altitude of  $150m$  and different airspeeds of  $14m/s$  and  $18m/s$ .

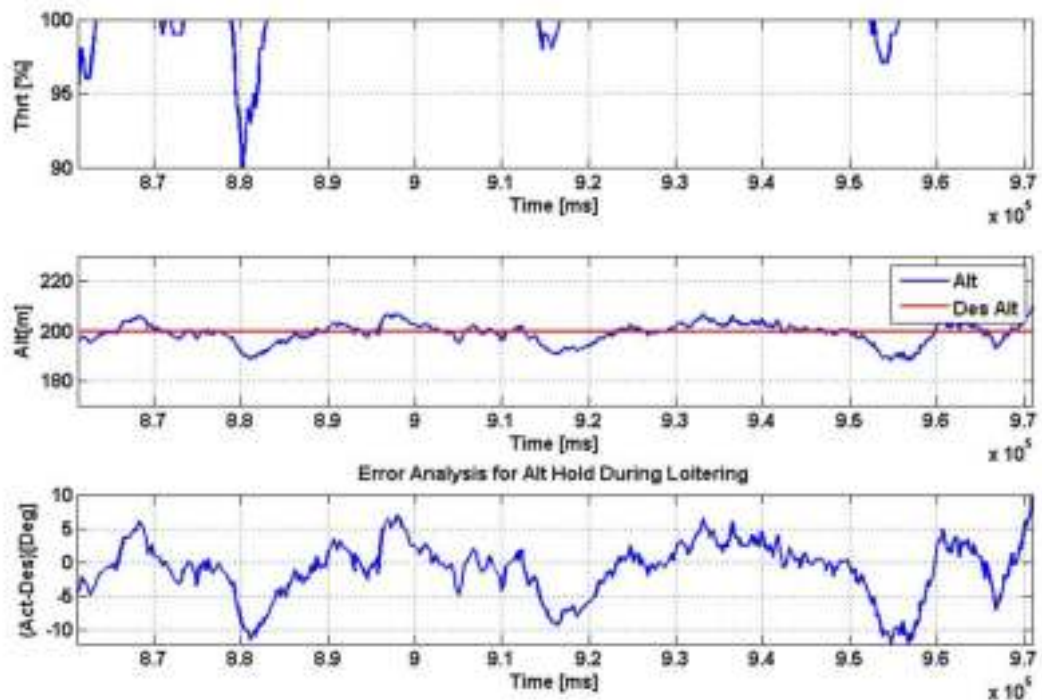


Figure 7.23: Error Analysis for the Altitude from the 150m Loiter Test

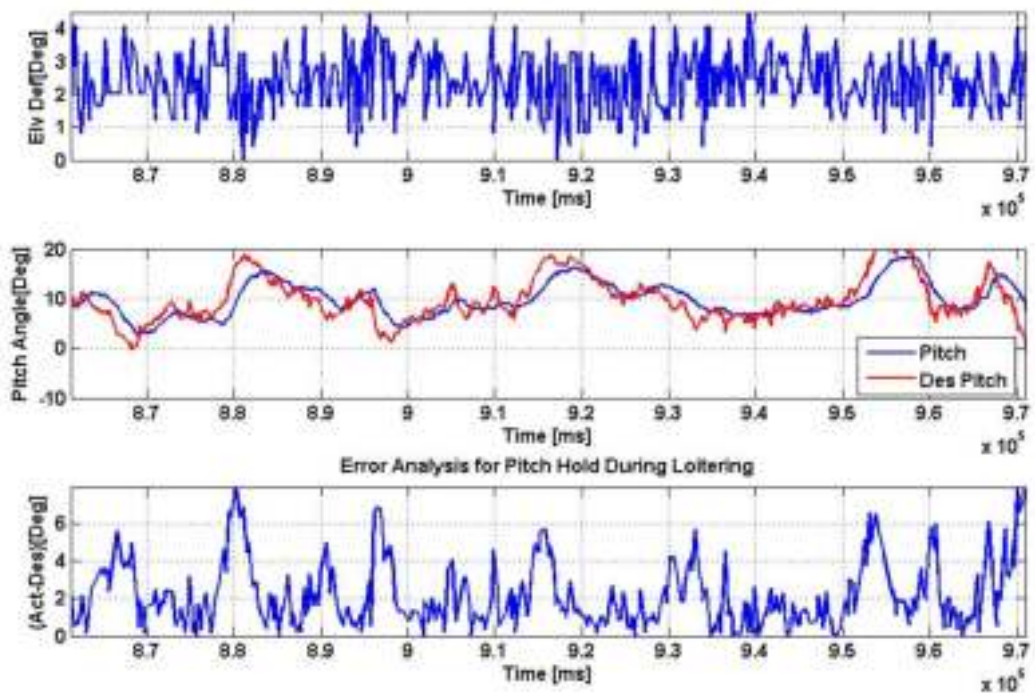


Figure 7.24: Error Analysis for the Pitch from the 150m Loiter Test

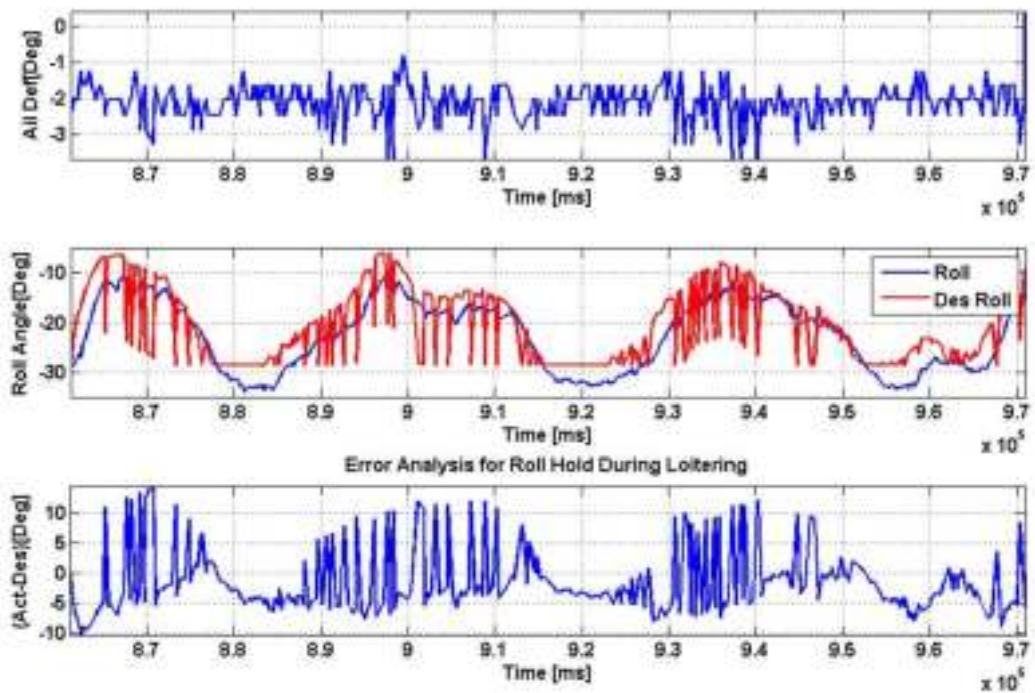


Figure 7.25: Error Analysis for the Roll from the 150m Loiter Test



Figure 7.26: 150m Loiter Test Map



Figure 7.27: Square Pattern

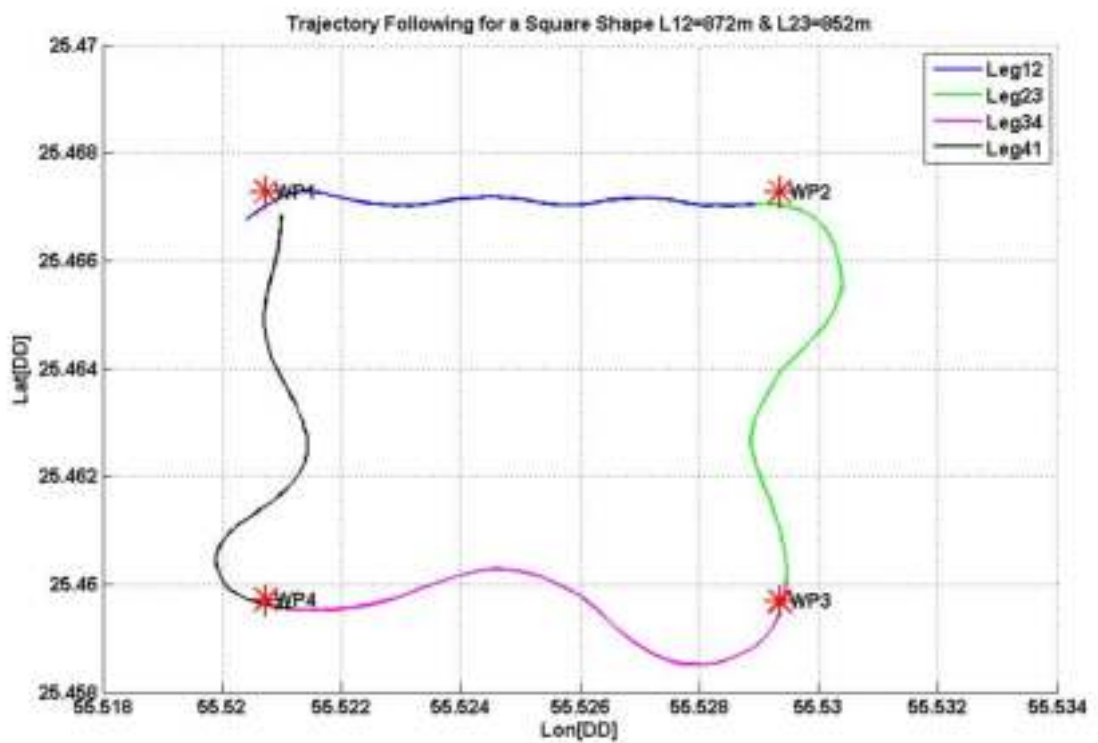


Figure 7.28: Four Waypoints Square Trajectory Test



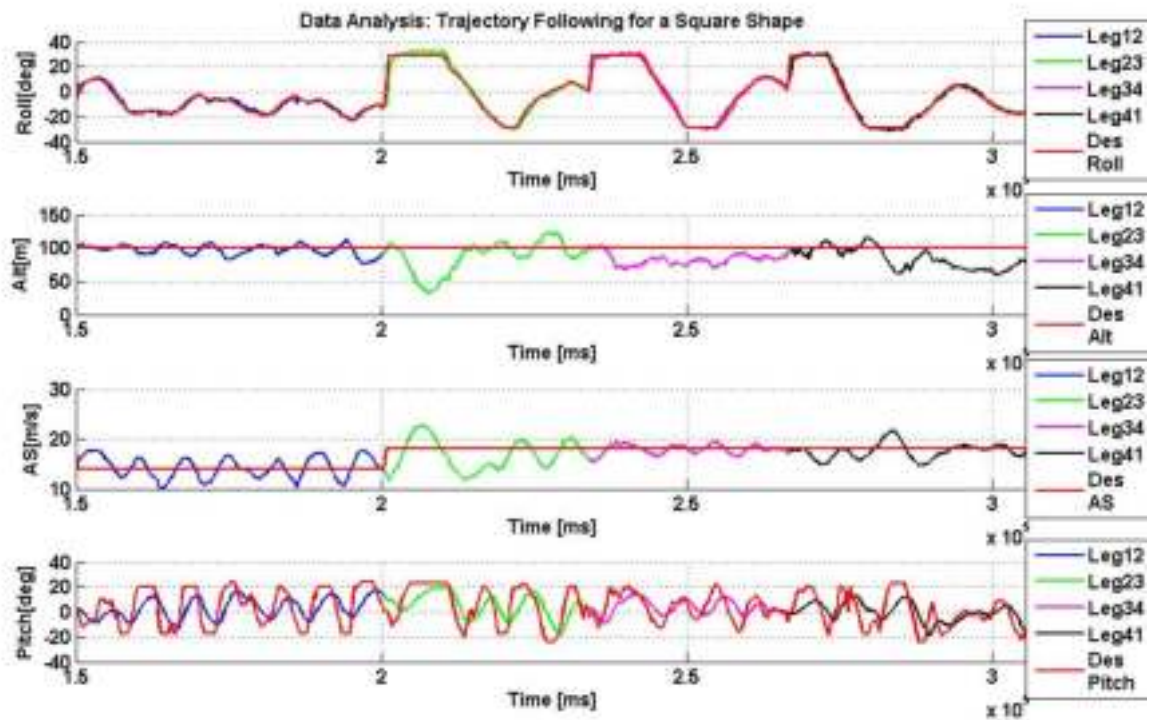


Figure 7.29: Four Waypoints Square Trajectory Test Analysis

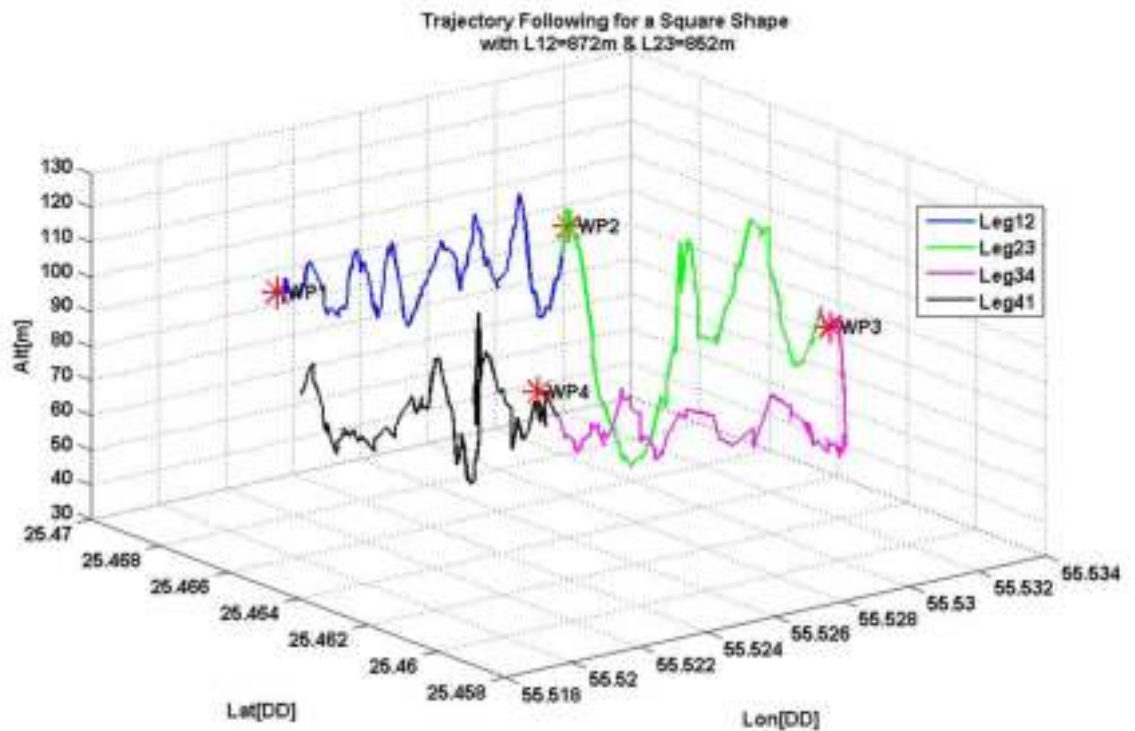


Figure 7.30: Four Waypoints Square 3D Trajectory

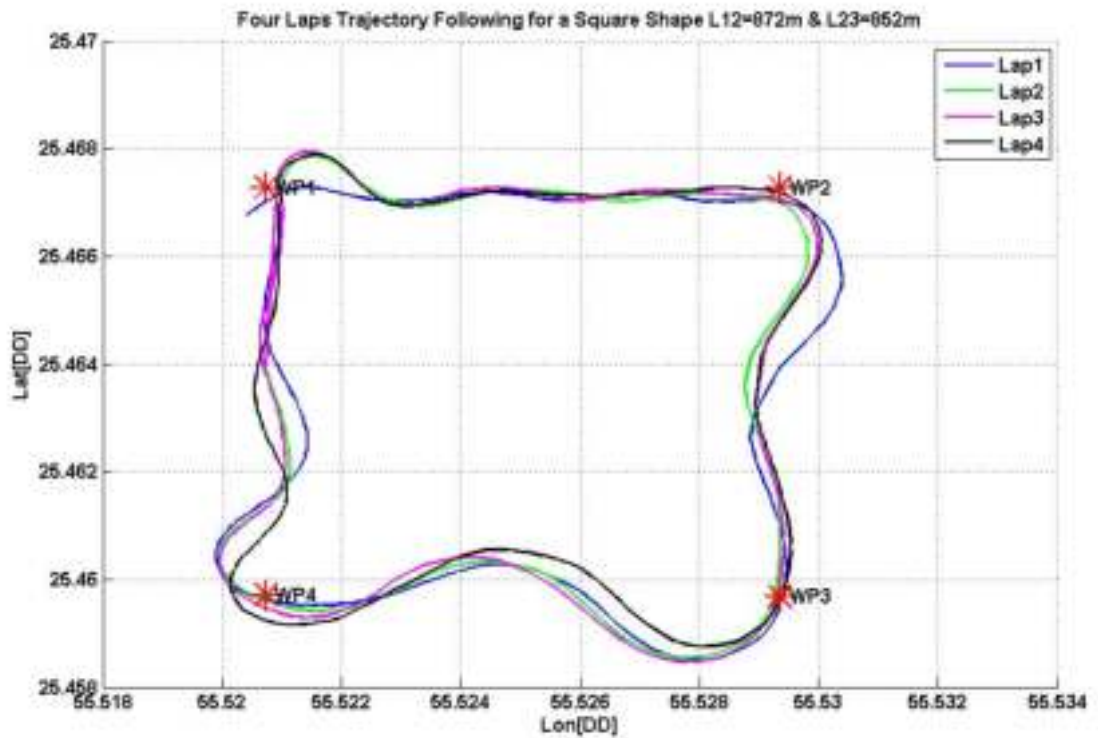


Figure 7.31: Four Laps:Four Waypoints Square 2D Trajectory

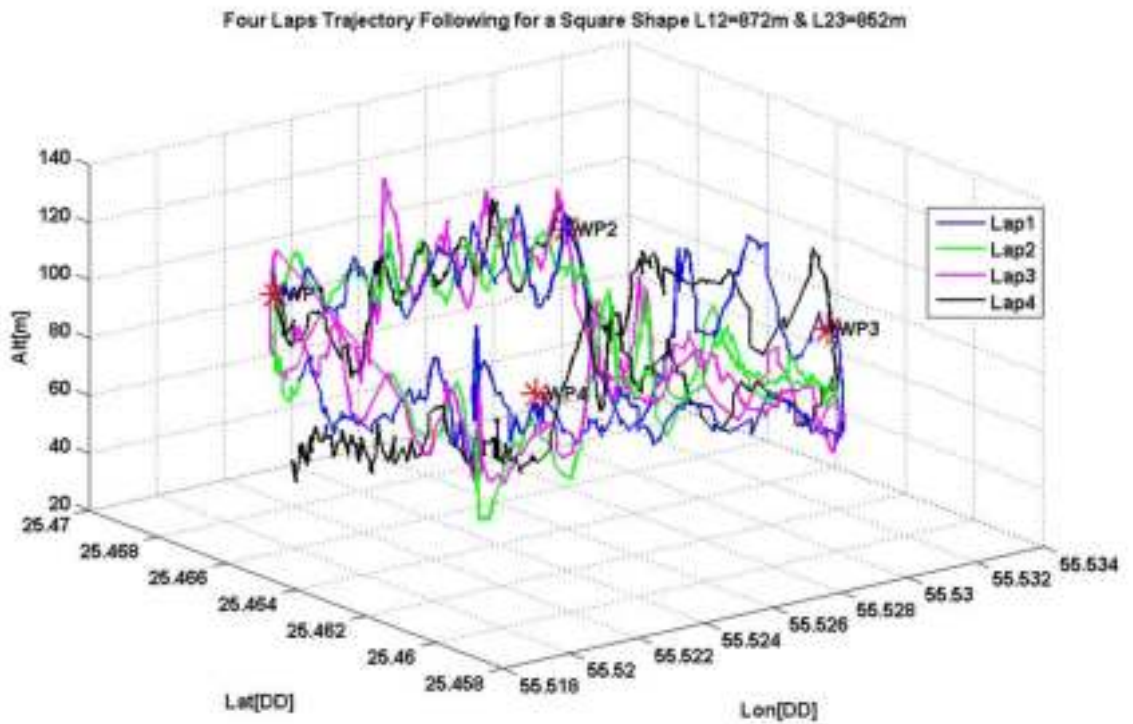


Figure 7.32: Four Laps:Four Waypoints Square 3D Trajectory



Figure 7.33: Four Laps:Four Waypoints Square 3D Trajectory Map



Figure 7.34: Hourglass Pattern

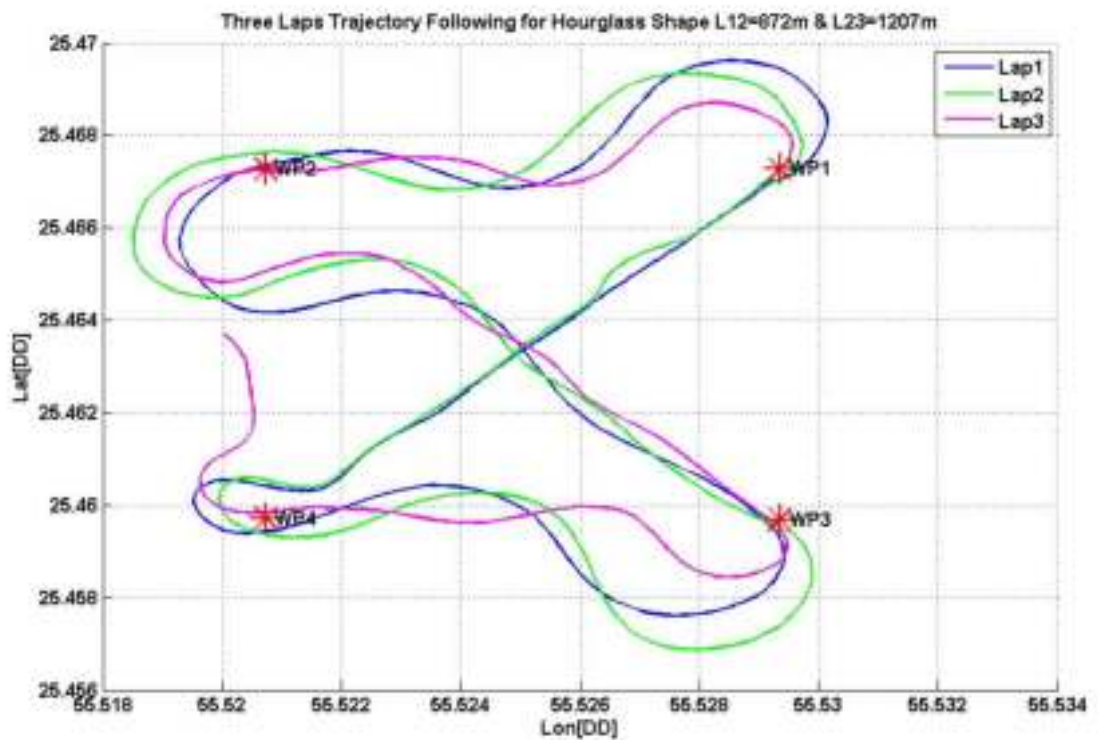


Figure 7.35: Four Waypoints Hourglass Trajectory Test

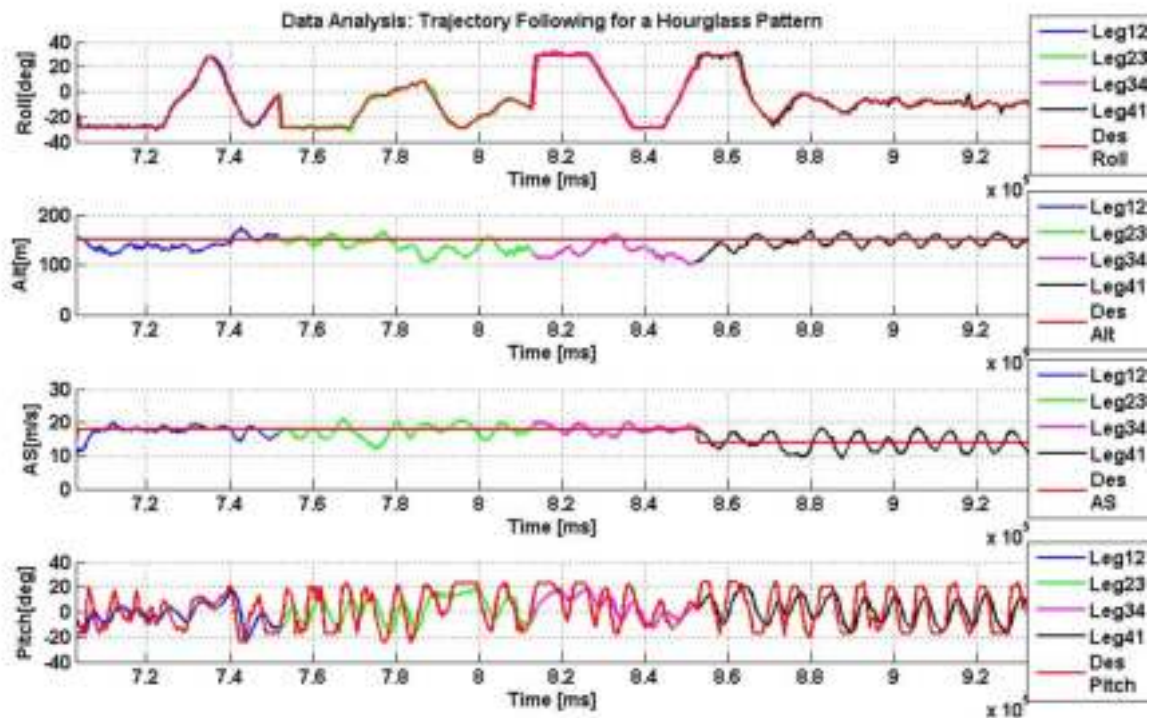


Figure 7.36: Four Waypoints Hourglass Trajectory Test Analysis

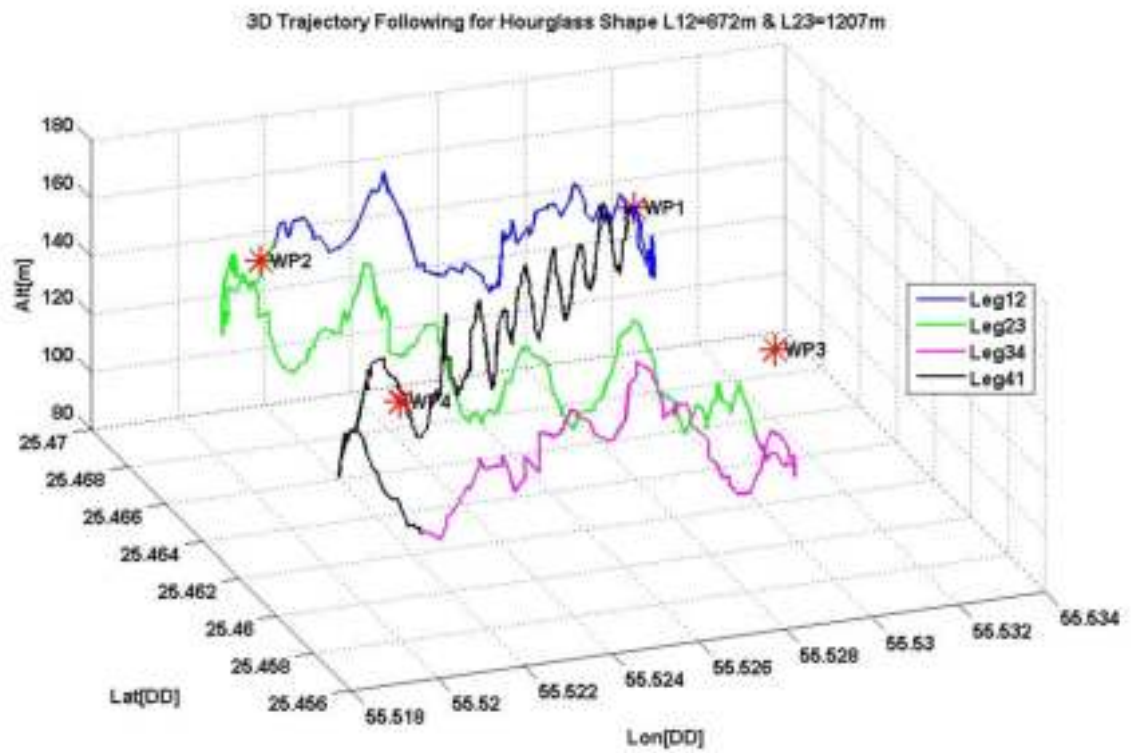


Figure 7.37: Four Waypoints Hourglass 3D Trajectory

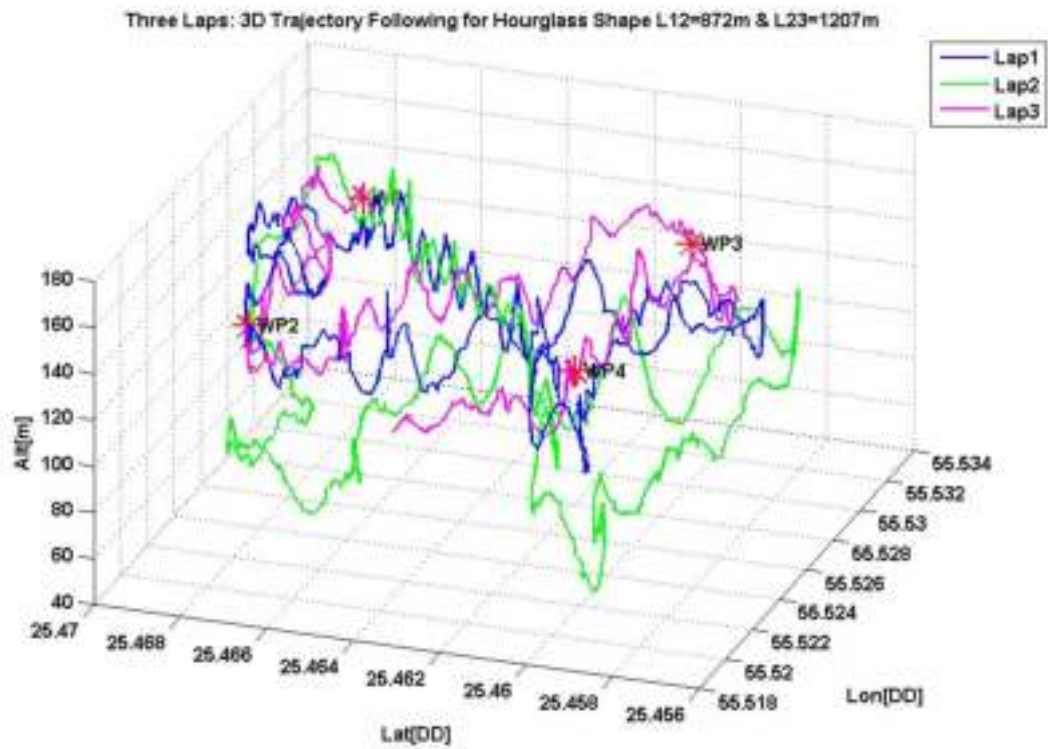


Figure 7.38: Three Laps:Four Waypoints Hourglass 3D Trajectory



Figure 7.39: Three Laps:Three Waypoints Hourglass 3D Trajectory Map

## CHAPTER 8

# THESIS SUMMARY AND FUTURE WORK

In this chapter, the accomplished contributions in this thesis are summarized. Then, recommendations for future research and development as follow-on to the work reported in this thesis are provided

### 8.1 SUMMARY AND CONTRIBUTIONS

#### 8.1.1 Avionics Unit Development

A low cost avionics unit using commercial off the shelf components was designed, built and tested. The designed avionics unit consists of a variety of sensors that consists of basic electronics components. The total cost of the developed unit was around 9,000 US\$.

#### 8.1.2 System Identification and Aircraft Nonlinear Modelling

To be able to control the aircraft, a non-linear model is built. The aircraft stability coefficients were estimated based on the aircraft geometry. To feed the controller with the right aircraft states, both the engine and servo motors subsystems are identified based on system identification techniques. Then, avionics unit sensors are modelled.

#### 8.1.3 Developing Hardware in The Loop Simulation

To test the developed avionics unit performance, a Hardware In the Loop Simulation was designed and tested on the aircraft non-linear model.

#### 8.1.4 Implementing SLC Based Autopilot and Trajectory Tracking Using Simulink Embedded Model-based Design

Improvements from previous versions of our work in AUS is the extensive use of the interactive design using MATLAB/SIMULINK environment. Simulink Response

Optimization, Control System Toolbox and Simulink Control Design are the major tools used for the autopilot design to interact with Simulink. And the Target for Freescale MPC5xx was used for the embedded system evaluation, implementation and code generation of the design in real-time.

#### 8.1.5 Developing Common Ground Station for UxV's in AUS

A common and new ground station design was built and developed. The ground station is developed using Visual Basic 2008 based software. The designed interface consists of gauges to monitor speed, altitude, and aircraft attitudes. It also includes a map that shows the position of the aircraft in the nearby area. Finally the GUI is also used to upload commands directly to the aircraft.

#### 8.1.6 Flight Testing

In this thesis, flight tests were conducted using Krestal autopilot to experiment with flight testing and compare the performance with our avionics unit HILS results.

## 8.2 FUTURE WORK

### 8.2.1 Ground Station Enhancement

Ground station still can be enhanced as the project is improving and seeking for more functions to be added to facilitate the user needs.

### 8.2.2 Nonlinear Autopilot and Trajectory Tracking Enhancement

In this thesis, a classical autopilot was designed for one trim condition. Future work can put more in this area by going through the gain scheduling for different trim conditions as well as designing a nonlinear autopilots. Moreover, with this designed test bed, the research in the area of guidance and trajectory tracking can be given a boost for algorithms validation.

### 8.2.3 Nonlinear System Identification

To get a better aircraft model, a nonlinear identification algorithms can be used and developed.



# APPENDIX A

## GEOMETRY, AERODYNAMIC, AND OTHER AIRCRAFT DESIGN INFORMATION

### A.1 AIRCRAFT GEOMETRY DEFINITIONS

#### A.1.1 Wingspan

Wingspan of aircraft The wingspan of an aircraft is always measured in a straight line, from wingtip to wingtip, independently of wing shape or sweep.

- Implications for aircraft design

Planes with a longer wingspan are generally more efficient because they suffer less induced drag and their wingtip vortices do not affect the wing as much. However, the long wings mean that the plane has a greater moment of inertia about its longitudinal axis and therefore cannot roll as quickly and is less maneuverable. Thus, combat aircraft and aerobatic planes usually opt for shorter wingspans to increase maneuverability.

Since the amount of lift that a wing generates is proportional to the area of the wing, planes with short wings must correspondingly have a longer chord. An aircraft's ratio of its wingspan to chord is therefore very important in determining its characteristics, and aerospace engineers call this value the aspect ratio of a wing. (Wikipedia the free encyclopedia, )

#### A.1.2 Mean Aerodynamic Chord (MAC)

Finding the Mean Aerodynamic Chord (MAC) Many plans indicate that the Center of Gravity (CG) should be located at a certain point of the Mean Aerodynamic Chord. The CG can be measured from any point along the span from the leading edge of the wing if the wing is a constant chord planform.

If the wing is tapered then you must locate the MAC before you can locate the CG.

### A.1.3 Aspect ratio (AR)

In aerodynamics, the aspect ratio is defined as span squared divided by wing area:

$$AR = \frac{b^2}{S}$$

Informally, a high aspect ratio indicates long, narrow wings, whereas a low aspect ratio indicates short, stubby wings.

## APPENDIX B

### HARDWARE AND SOFTWARES USED IN THIS THESIS

#### B.1 HARDWARE

##### B.1.1 OS FS120 Engine

The aircraft thrust force comes from a 16 x 24 propeller mounted on a gasoline engine. The engine shown in the Figure B.1 is a 1.200 cubic inches with a maximum power of 2.5 horsepower. The OS FS120 is a four stroke engine from O.S., which starts by hand cranking. It is designed for sport, but engineered for excellence. Its RPM ranges from 2000-11000. Table B.1 lists the engine specs.



Figure B.1: OS FS120 Engine

##### B.1.2 MIDG II INS/GPS

The MIDG II is an Inertial Navigation System (INS) with Global Positioning System (GPS) contained in an incredibly small package. This INS GPS package is ideally suited for any unmanned vehicle application that requires an inertial navigation solution. The MIDG II INS/GPS package is specifically designed to be used with the

Table B.1: S FS120 Engine Specifications

Engine Type	4-Stroke
Displacement	1.200 cu. in.
Cylinders	1
Displacement	1.200 cubic inches
Bore	1.197 (in.)
Stroke In	1.083 (in.)
Shaft	5/16 x 24 Thread
Low RPM	2000
High RPM	11000
Horse Power	2.500 bhp @ 10000 RPM
Weight (no muffler)	36.30 oz.



Figure B.2: MIDG II:Inertial Navigation System (INS) with Global Positioning System (GPS)

Microbot Autopilot Platform, but can also be used with other autopilot packages for primary instrumentation.

Message rates are configurable, and individual messages may be polled. All data messages are time stamped with GPS time, and a One Pulse Per Second signal is available for time synchronization in the host computer. Operational mode is selectable, including IMU only operation, vertical gyro simulation with magnetic aiding, and full INS solution. MIDG is intended for use in applications requiring a full state vector, including attitude, position, altitude, velocity, acceleration, and angular rates.

MIDG II INS/GPS Product Features:

- Size : 1.50 x 1.58 x 0.88
- Weight : Under 55 grams (1.9 oz.)
- 3-Axis Rate Gyro



Figure B.3: MMPX4115A Absolute Pressure Sensor

- 3-Axis Accelerometer
- 3-Axis Magnetometer
- Differential Ready GPS; WAAS/EGNOS compliant
- Power In: 10 to 32 VDC, 1.2W maximum
- Hardware filters provide vibration immunity
- Advanced filter algorithms for exceptional performance
- Position, Velocity, and Attitude from Kalman Filter at 50Hz

### B.1.3 MPX4115A Absolute Pressure Sensor

The sensor we used in order to sense the absolute pressure is the Motorola MPX4115 shown in Figure ???. The Manifold Absolute Pressure (MAP) sensor is one of the state of the art from its kinds, it costs around 30\$.

Motorola MPX4115 is a piezoresistive transducer; which integrates on chip bipolar op-amp circuitry and a thin film resistor network to provide a high output signal and temperature compensation.

part comes with six pins of which only three are used. Pins 4, 5 and 6 are no connections. Pin 1 is the output that varies with the air pressure while pins 2 and 3 are the VCC and the ground connections.

The sensor outputs an analog voltage proportional to pressure using a linear equation. The sensor also as we mentioned before has on-chip signal conditioning to produce an output range of 0.2V at (15Kpa) to 4.8V at (115Kpa).

#### B.1.4 1INCHGBASIC Differential Pressure Sensor

The pitot tube is connected to a gauge pressure sensor to get a measurement of the difference between the static and total pressures. We are using the 1INCHGBASIC low pressure differential/gauge sensor fully signal conditioned.

Wind Tunnel experiments are used in meteorology and engineering sciences to investigate flow over and around obstacles, such as mountains, airplane wings, or vehicles, under controlled conditions. This experiment is designed to examine the relationships between wind speed and the pressure it exerts, the effect of high winds on vehicles, and the mechanism by which very high winds can destroy buildings.

In order to calibrate our gauge pressure sensor a wind tunnel test is used to establish the wind-pressure relationships when air flows over a flat surface. The "pitot tube" sensor and a turbine anemometer are used to obtain both pressure and wind speed.

## APPENDIX C

# ENGINE AND ACTUATORS SYSTEM IDENTIFICATION

### C.1 ENGINE SYSTEM ID

To build the aircraft nonlinear model we need to characterize the engine response to throttle command. The engine dynamics is a function of several inputs like fuel inlet, manifold pressure, temperature, and air pressure. For simplicity we assume that the other inputs are constant and we are only changing the throttle command. An experiment has been conducted to get a transfer function that relates the throttle command input to engine RPM and propeller thrust force output. The experiment was applied on two engine-propeller assembly sets.

#### C.1.1 The Engine and its Propeller Modeling

The ARF60 AUS-UAV thrust is provided by *fixed pitch propeller-internal combustion engine assembly*. Since one of the important roles for the propulsion system is to provide enough thrust to balance the UAV drag during flight, a faithful mathematical model for the engine-propeller can be obtained to be used for constructing the nonlinear mathematical model of the UAV.

#### Experimental Design

The data collected from the experimental setup are the engine thrust and the engine RPM. The thrust is measured using load cell while the RPM is measured using IR Reflective object sensor. The input signal is the duty cycle that controls the throttle and is represented by the pseudo random binary sequence to excite all the dynamics in the system. An introduction to the sensors utilized in this experiment, as well as the experiment setup is provided.

**RPM Sensor** A sensor was needed to measure the engine RPM. The reading from WW-01 WheelWatcher low cost incremental encoder system is utilized to measure the RPM. Both standard ChA/ChB raw quadrature outputs, as well as decoded Clock and Direction signals are available. The clock signal produces  $25\mu s$  pulses at each transition of ChA or ChB, providing a 4x increase in resolution - 128 clocks per servo rotation - while the direction signal indicates the decoded direction of rotation. The readings from each channel is recorded and saved.

**Load Cell Sensor** A load cell is used to measure the thrust force that occurs on the aircraft due to the rotation of the propeller. The load cell used is the Entran ELPM series 1250N. The load cell was mounted on a frame that was used for the experiment. Before using the load cell, it needs to be calibrated with a known mass. The voltage output for a given weight is shown in table C.1. Equation C.1 relates the load force to the output voltage according to the linear fitting shown in Figure C.1.

$$Load[N] = 0.52016 \times Voltage - 8.269 \quad (C.1)$$

**Experiment Setup** Using dSPACE, an experiment has been made that takes a throttle command as a pseudo random variable input. Then, the throttle command is fed to the throttle servo motor. The Engine RPM changes due to the change in the fuel combustion rate. The encoder reads this RPM and sends its data to dSPACE. Also due to the rotation of the engine the propeller will apply a thrust force on the aircraft. This force is measured by the load cell and its output is also saved in dSPACE. The experiment setup block diagram is shown in C.2. Simulink-dSpace program used to generate the PRBS signal, RPM measurement and thrust measurement. These results are shown in Figures C.3 , C.4 and C.5 respectively.

## C.2 ACTUATOR SYSTEM ID

The control surfaces of the UAV are actuated by four identical R/C servo motors. Each servo arm is coupled to the corresponding control surface via mechanical links.



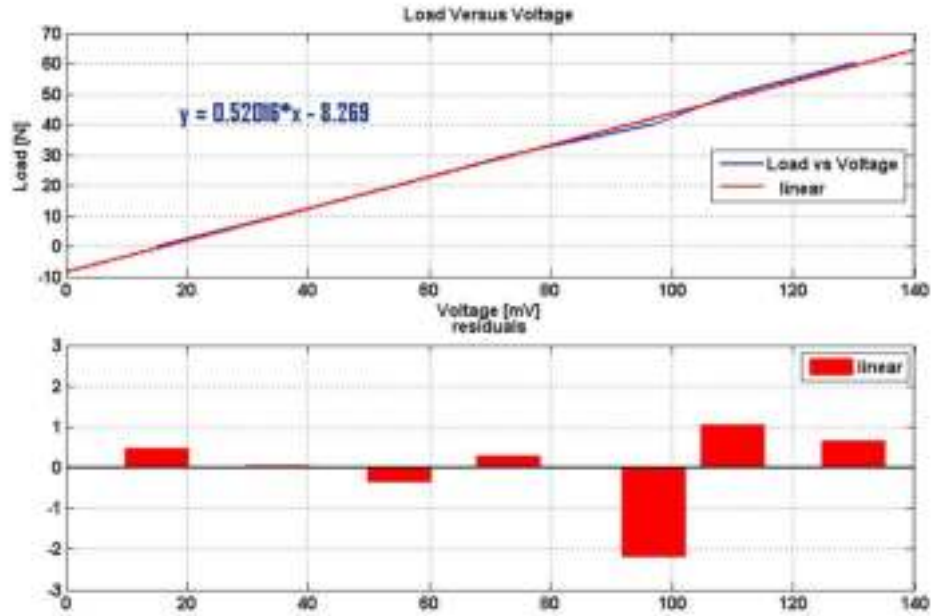


Figure C.1: Load Cell Calibration Plot

Table C.1: Load cell calibration data

Load [N]	Voltage [mV]
0	15
10	35
20	55
30	73
40	97
50	110
0	130

The data collected from the experimental setup (see Figure C.6) are the servo position and the control commands. The deflection angles of the control surfaces are measured by the potentiometers linked to the servo motor, and calibrated using a digital encoder. It appears that an R/C servo motor nearly performs a dead beat control action. Thus, a first-order low pass filter and control saturation results in a good actuator model. Figures summarize the results of dynamic modelling of the control surfaces.

$$G(s) = \frac{K}{1 + ST_{p1}} e^{-sT_d} \quad (C.2)$$

$$G_{\delta a} P1 = \frac{7.373}{s + 9.52} \quad (C.3a)$$

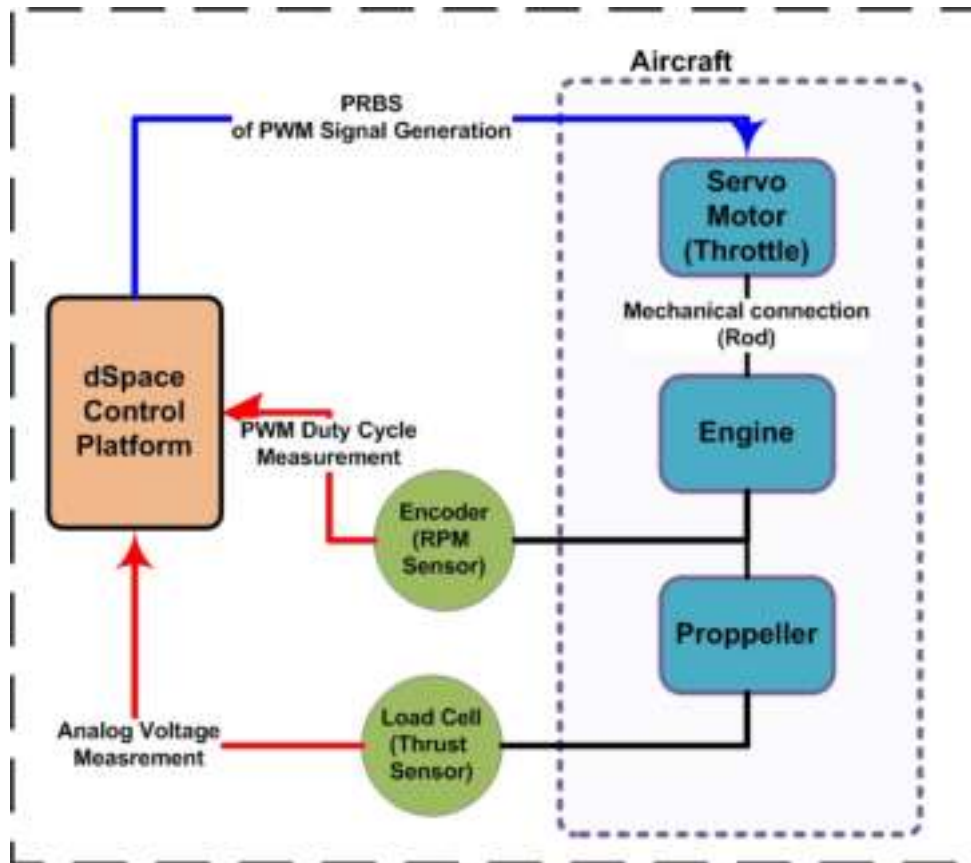


Figure C.2: Engine Identification Setup

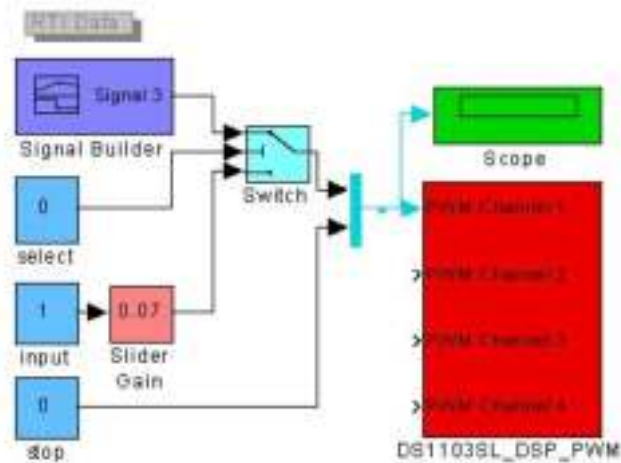


Figure C.3: PRBS PWM Signal Generation using dSpace Toolbox Blocks

$$G_{\delta_a P1D} = \frac{11.02}{s + 14.35} e^{-0.03s} \quad (\text{C.3b})$$

$$G_{\delta_a P1DZ} = \frac{-0.2065s + 11.78}{s + 14.35} e^{-0.03s} \quad (\text{C.3c})$$

$$G_{\delta_a P1} = \frac{4.468}{s + 6.521} \quad (\text{C.4a})$$

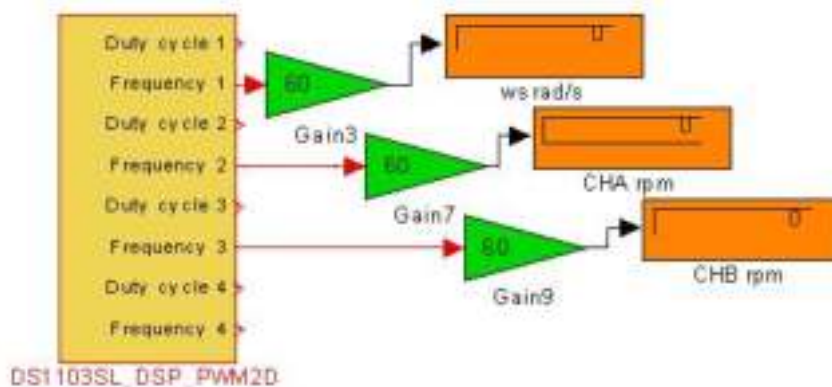


Figure C.4: RPM Measurement using dSpace Toolbox Blocks

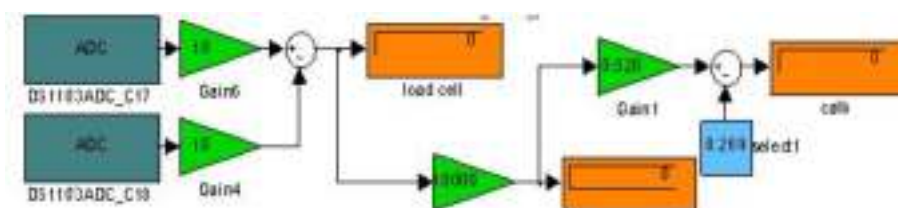


Figure C.5: Thrust Measurement using dSpace Toolbox Blocks

$$G_{\delta a}P1D = \frac{6.143}{s + 9.281} e^{-0.03s} \tag{C.4b}$$

$$G_{\delta a}P1DZ = \frac{-0.1826s + 6.675}{s + 10.18} e^{-0.03s} \tag{C.4c}$$



Figure C.6: Actuator Identification Setup

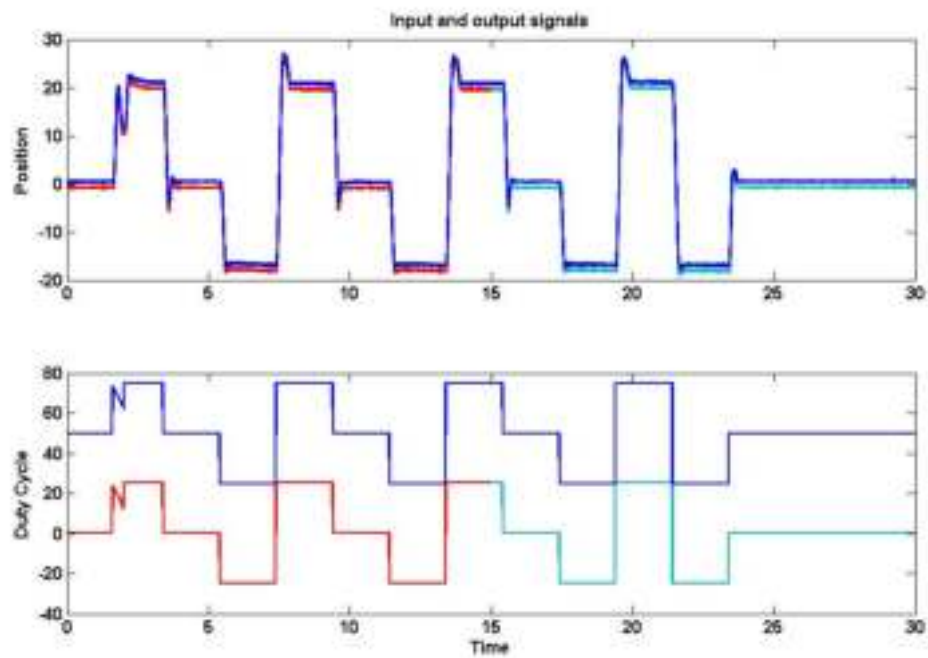


Figure C.7: Aileron actuator response with the doublets input

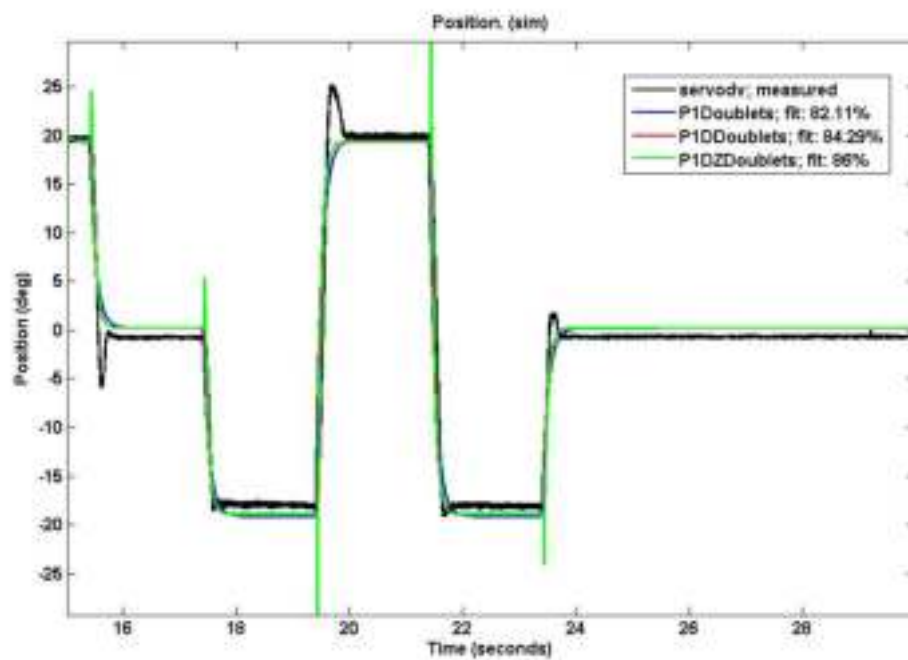


Figure C.8: Aileron Actuator Identification Results for Doublets inputs

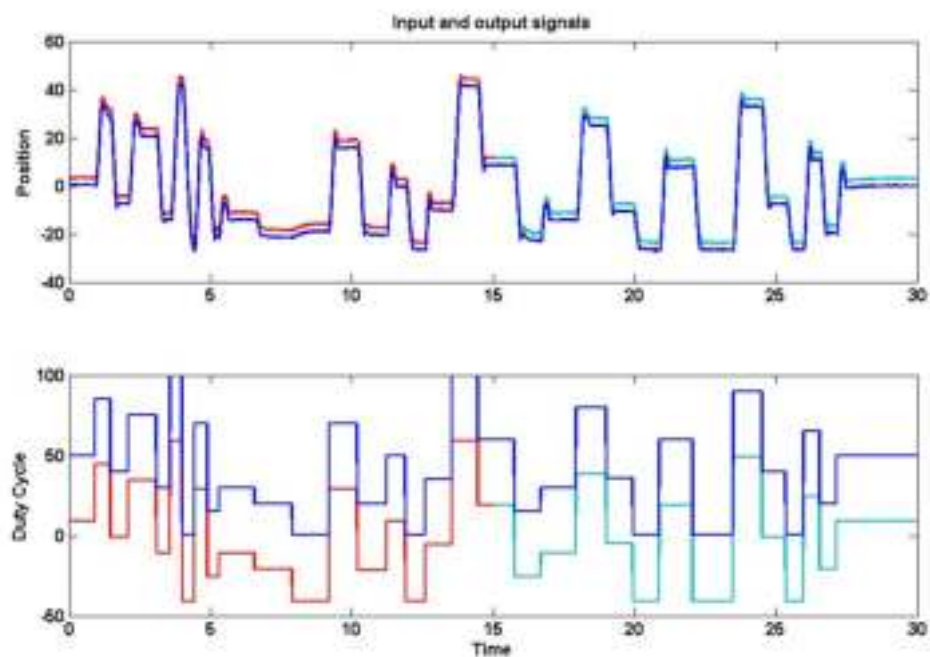


Figure C.9: Aileron actuator response with the PRBS input

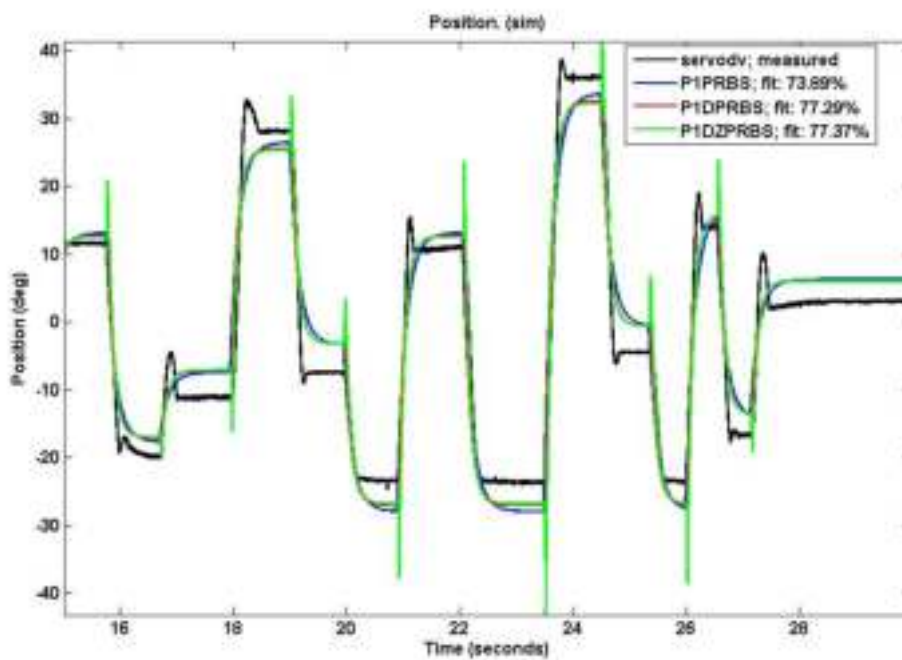


Figure C.10: Aileron Actuator Identification Results for PRBS inputs

## REFERENCES

- Beard, R. (2006). Vector field path following for small unmanned air vehicles. *Proceedings of the 2006 American Control Conference*.
- Bernard Etkin, L. D. R. (1996). *Dynamics of Flight: Stability and Control*. John Wiley & Sons.
- Bhatt S. P., K. P. (2005). A feedback guidance strategy for an autonomous mini-air vehicle. *National Conference on Control and Dynamical Systems*.
- Chunhua Hu, Xingli Huang, J. H. & Zhu, J. (2004). System identification of a small uavs speeding up process before take-off. *The Proceedings of the 5th Asian Control Conference*.
- Dongwon Jung & Panagiotis Tsiotras (2007). Modeling and Hardware-in-the-Loop Simulation for a Small Unmanned Aerial Vehicle. *American Institute of Aeronautics and Astronautics, file = F*.
- dSPACE. *dSPACE - Control Design*.
- Hadi, M. (Spring 2005). Autopilot design based on fuzzy supervisory controller for aus-autonomous vehicle. Master's thesis, American University Sharjah (AUS).
- Hassan, M. (Spring 2006). Aus-uav hils setup of dynamic flight path planning. Master's thesis, American University Sharjah (AUS).
- Holland, G. (1998). <http://www.aerosonde.com/drawarticle/42>.
- Jung, S. (2001). Autopilot design for the stanford dragonfly uav: Validation through hardware-in-the-loop simulation. *AIAA*.
- Kaminer, A. Pascoal, E. H. & Silvestre, C. (1998). Trajectory tracking for autonomous vehicles: An integrated approach to guidance and control. *AIAA Guidance, Control Dynamics*, 21(1), 29–38.
- Leonardo, D. *RS232 Blockset for Simulink*.
- Li-Xin Wang (1995). Design and analysis of fuzzy identifiers of nonlinear dynamic systems. *IEEE transactions on automatic control*.
- Peddle, I. K. (2005). Autonomous flight of a model aircraft. Master's thesis, University of Stellenbosch.
- Pike, J. (2005). <http://www.globalsecurity.org/military/systems/aircraft/x-47.htm>.
- R. Connor, R. E. L. (2001). <http://www.nasm.si.edu/research/aero/aircraft/pioneer.htm>.

- R. Pintelon & J. Schoukens. (2001). *System Identification: A Frequency Domain Approach* (1st ed.). Wiley-IEEE Press.
- Randal W. Beard, T. W. M. (2007). *An Introduction to Autonomous Miniature Air Vehicles*. Brigham Young University.
- Rauw, M. . (1992). *Using SIMULINK for Nonlinear Analysis of Aircraft Control Systems*. PhD thesis, Delft University of Technology (Aerospace Engineering).
- Rolf, R. (September 2003). Uav path following for constant line of sight. *AIAA Unmanned Unlimited Systems, Technologies and Operations Conference, San Diego, CA*.
- S. Park, J. D. & How, J. (Aug. 2004). A new nonlinear guidance logic for trajectory tracking. *AIAA Guidance, Navigation Control Conference*.
- Shaaban, A. (2006). Real-time Validation and Comparison of Fuzzy Identification and State-space Identification for a UAV Platform.
- v1.9.1, F. (2009). *FlightGear Flight Simulator*.
- Vladislav Klein & Eugene A. Morell (2006). *Aircraft System Identification: Theory and Practice* (1st Edition ed.). American Institute of Aeronautics and Astronautics, AIAA.
- Wikipedia the free encyclopedia. [www.wikipedia.org](http://www.wikipedia.org).
- Wise, R. (2006). *UAV Control and Guidance for Autonomous Cooperative Tracking of a Moving Target*. PhD thesis, University of Washington.
- Zadeh, L. (2007). *The Fuzzification of Systems*, volume Volume 216/2007, chapter From Circuit Theory to System Theory, (pp. 165–200). Springer Berlin / Heidelberg.